

UNIVERSITY OF BRISTOL

DOCTORAL THESIS

---

OBSERVING, ANALYSING, MODELLING, AND  
EVEN CHANGING THE BEHAVIOUR OF  
ZEBRAFISH

---

*Author:*  
YUSHI YANG

*Supervisors:*  
DR. THOMAS MACHON  
DR. CRISSY HAMMOND  
DR. C PATRICK ROYALL

*A dissertation submitted to the University of Bristol in accordance with  
the requirements for award of the degree of Doctor of Philosophy in the  
Faculty of Science, H. H. Wills Physics Laboratory.*

March 2022

37257 Words



# Abstract

A group of animals is a typical active matter system, whose behaviour can be understood from the perspective of statistical physics.

Here we studied the behaviour of zebrafish experimentally. We developed a novel algorithm to extract fish locations from 2D images. By incorporating images captured from synchronised cameras, we calculated the 3D locations of individual fish in a group. The data-processing pipeline developed in this work allows the trajectories of the fish being recovered from the coordinates. We then analysed the collective behaviour of the zebrafish by different correlation functions. We find the macroscopic states of the fish can switch between ordered and disordered. The changing states of the fish is dominated by a dynamical length scale as well as a structural length scale. More specifically, the polarisation of fifty zebrafish correlate robustly with a dimensionless number, the ratio between the persistence length and the nearest neighbour distance of individual fish.

To understand the observed zebrafish behaviour, we proposed different models to fit the density distribution of the fish as well as the dynamics of the fish. For the spatial distribution of the fish, our model highlights the fish-environment interaction, that dominates the behaviour of small groups ( $N < 5$ ), and the fish-fish interaction, that dominates the behaviour of large groups ( $N = 50$ ). For the dynamics of the fish, our model revealed the importance of the orientational inertia for the fish individuals, and the alignment interaction between the fish.

Finally, we applied the established methods to biology, and studied the behavioural feature of the *col11a2* mutant zebrafish, whose genetic modification is related to human diseases. The *col11a2* mutant zebrafish individuals exhibited slower re-orientation, corresponding to a higher activity. Consequently, a group of *col11a2* mutant zebrafish exhibited more ordered behaviour, compared to the wildtype zebrafish. The linkage between the individual behaviour and the collective behaviour of the *col11a2* mutant zebrafish can be explained by our proposed active matter model.



天涯海角 觅觅知音



# Acknowledgements

I would like to thank Paddy Royall, Chrissy Hammond, John Russo, and Thomas Machon for helpful guidances on the project. I will not be able to carry out my researches without the financial support from China Scholar Council and university of Bristol.

I could not thank Francesco Turci, Erika Kague, and Abraham Mauleon Amieva enough for their tremendous supports, as my tutors and my friends. Ioatzin Rios de Anda told me I will finish my study, just by *not giving up*. These are the reasons I did not quit my PhD.

Working in G39 is a pleasant experience. I wish Fergus Moore a pleasant experience as a software engineer, and Levke Ortlieb to solve the glass transition problem *again*. I hope Jingwen Li (李静文) to find a good job in academia, and Xiaoyue Wu (武晓岳) to have more fun with coding. I appreciate the nice chats with Jun Dong (董君), Rui Cheng (程睿), and Laurent Vaughan, the free cigarettes from Maximilian Kloucek and Nariaki Sakaï, the crochet techniques from My Nguyen, and the *friendship* offered by Marcos Villeda Hernandez and Teodoro Garcia Milan.

The Bristol Centre for Functional Nanomaterials (BCFN) provided tremendous amount of help for me to study and live in a foreign country. The management team of BCFN as well as the 2017 cohorts are the best. The support from the fish facility in Bristol, as well as the group members in Hammond Lab are extremely helpful. All the talks in Chrissy's group meeting surprised me with the power of biology.

Shamelessly, I copied a lot of code snippets and ideas from the nameless heroes and heroines on the Internet. The charitable contributions from Francesco Turci (@Fturci), Joshua Robinson (@tranqui), Peter Crowther (@marrygoat), Katherine Skipper (@kskips), and Michael P Allen (@Michael-P-Allen) were extremely helpful.

I will not forget the accompany of Min Wang (王敏), and all the sleepless nights we spent together, chatting, worrying, and laughing.



# Author's declaration

I declare that the work in this dissertation was carried out in accordance with the requirements of the University's Regulations and Code of Practice for Research Degree Programmes and that it has not been submitted for any other academic award. Except where indicated by specific reference in the text, the work is the candidate's own work. Work done in collaboration with, or with the assistance of, others, is indicated as such. Any views expressed in the dissertation are those of the author.

SIGNED: .....  DATE: ..... 29/03/22.

## Publications:

1. Y. Yang et al., "Dominating lengthscales of zebrafish collective behaviour", [PLOS Computational Biology 18, 1 \(2022\)](#)

## Other Contributions

1. E. Kague et al., "3D assessment of intervertebral disc degeneration in zebrafish identifies changes in bone density that prime disc disease", [Bone Research, 1 \(2021\)](#)
2. P. López-Cuevas et al., "Transformed notochordal cells trigger chronic wounds in zebrafish, destabilizing the vertebral column and bone homeostasis", [Disease Models & Mechanisms 14, dmm047001 \(2021\)](#)
3. R. Salazar-Silva et al., "NCOA3 identified as a new candidate to explain autosomal dominant progressive hearing loss", [Human Molecular Genetics 29, 3691 \(2021\)](#)



# Contents

<b>Abstract</b>	iii
<b>Acknowledgements</b>	vii
<b>Author's declaration</b>	ix
<b>List of figures</b>	xvi
<b>List of tables</b>	xvii
<b>List of Abbreviations</b>	xix
<b>List of Symbols</b>	xx
<b>1 Introduction</b>	1
1.1 Collective Behaviour . . . . .	1
1.2 Zebrafish . . . . .	1
1.3 Thesis Structure . . . . .	2
<b>2 The Collective Behaviour of Animals as Active Matter</b>	4
2.1 Active Matter . . . . .	4
2.1.1 What is the activity? . . . . .	4
2.1.2 What does active matter do? . . . . .	5
2.1.3 Animals as Active Matter . . . . .	8
2.2 The Observation of Animal Behaviour . . . . .	8
2.2.1 Complex Patterns Seen in Nature . . . . .	8
2.2.2 Observing the Collective Motion in 2D . . . . .	8
2.2.3 Observing the Collective Motion in 3D . . . . .	9
2.3 The Analysis of the Collective Motion . . . . .	10
2.3.1 Identifying Behavioural Patterns with <i>Order Parameters</i> . . . . .	10
2.3.2 Probing the Structure: the Radial Distribution Function . . . . .	11
2.3.3 Probing the Dynamics: the Correlation function of Orientation . . . . .	12
2.3.4 Probing the Dynamics: the Auto-Correlation Function . . . . .	13
2.3.5 Novel Correlation Functions for Animals . . . . .	14
2.4 Understanding the Animal Behaviour . . . . .	15
2.4.1 Microscopic Approach: Agent Based Models . . . . .	15
2.4.2 Hydrodynamic Approach: Continuum Models . . . . .	15
2.4.3 Thermodynamic Approach: Equation of State . . . . .	16

2.5	Is Active Matter an <i>Useful</i> Concept? . . . . .	17
<b>3</b>	<b>Observing Zebrafish in 2D</b>	<b>20</b>
3.1	Introduction . . . . .	20
3.2	Methods . . . . .	21
3.2.1	Fish and Apprautus . . . . .	21
3.2.2	Metric Rectification . . . . .	22
3.2.3	Image Processing . . . . .	23
3.2.4	Extracting Features from the Image . . . . .	24
3.2.5	Finding Templates for the Features . . . . .	26
3.2.6	Convolutional Neural Network . . . . .	28
3.3	Results . . . . .	30
3.3.1	A Single Fish . . . . .	30
3.3.2	Two Fish . . . . .	30
3.3.3	Three Fish . . . . .	31
3.3.4	Many Fish . . . . .	32
<b>4</b>	<b>Observing Zebrafish in 3D</b>	<b>34</b>
4.1	Introduction . . . . .	34
4.2	Methods . . . . .	35
4.2.1	Tank Design and Hardware . . . . .	35
4.2.2	Locating One Fish in 3D . . . . .	37
4.2.3	Locating Many Fish in 3D . . . . .	39
4.2.4	Optimising the Stereo Matching . . . . .	40
4.2.5	Assessing the Algorithm . . . . .	42
4.3	Results . . . . .	43
4.3.1	A Single Fish . . . . .	43
4.3.2	Two Fish . . . . .	45
4.3.3	Three Fish . . . . .	46
4.3.4	Many Fish . . . . .	46
4.3.5	The Holes on the Tank . . . . .	47
<b>5</b>	<b>Analysing Zebrafish Behaviour</b>	<b>50</b>
5.1	Introduction . . . . .	50
5.2	From Locations to Better Locations . . . . .	51
5.2.1	Removing Overlapping and <i>Hard</i> Particles . . . . .	51
5.2.2	Removing Overlapping and <i>Soft</i> Particles . . . . .	54
5.3	From Better Locations to Trajectories . . . . .	55
5.3.1	Equilibrium Linking . . . . .	56
5.3.2	Active Linking . . . . .	57
5.3.3	Extending the Trajectories . . . . .	58
5.4	From Trajectories to Behaviour . . . . .	59
5.4.1	The Structure . . . . .	59
5.4.2	The Dynamics . . . . .	61
5.5	The Behaviour of 50 Zebrafish in 2D . . . . .	63
5.5.1	The Structure . . . . .	63
5.5.2	The Dynamics . . . . .	64
5.5.3	The Changing States . . . . .	66

5.6	The Behaviour of 50 Zebrafish in 3D . . . . .	67
5.6.1	The Structure . . . . .	67
5.6.2	The Dynamics . . . . .	69
5.6.3	The Changing States . . . . .	70
5.7	The Universal Behaviour of Zebrafish . . . . .	71
<b>6</b>	<b>Modelling Zebrafish</b>	<b>73</b>
6.1	Introduction . . . . .	73
6.2	Simulation Methods . . . . .	74
6.2.1	General Idea . . . . .	74
6.2.2	Monte-Carlo Simulation . . . . .	74
6.2.3	Dynamical Simulation . . . . .	75
6.3	The Distribution of the Density . . . . .	75
6.3.1	The Effect of the Tank . . . . .	75
6.3.2	The Effect of the “Gravity” . . . . .	77
6.3.3	The Effect of the Holes . . . . .	78
6.3.4	The Effect of Pairwise Interaction . . . . .	78
6.3.5	Comparison to Experimental Data . . . . .	80
6.3.6	Limitation of the Model . . . . .	81
6.4	The Order of the Dynamic . . . . .	81
6.4.1	The Vicsek Model . . . . .	81
6.4.2	The Effect of Inertia . . . . .	83
6.4.3	Comparing with the Experiment . . . . .	84
6.4.4	Limitations of the Model . . . . .	86
<b>7</b>	<b>Collective Behaviour of Mutant Zebrafish</b>	<b>88</b>
7.1	Introduction . . . . .	88
7.2	Method . . . . .	89
7.2.1	Mutant Fish . . . . .	89
7.2.2	Experiments and Analysis . . . . .	89
7.3	The Behaviour of A Single Mutant Fish . . . . .	90
7.4	The Behaviour of Many Mutant Fish . . . . .	91
7.4.1	The Behavioural Features of <i>col11a2</i> mutant zebrafish . . . . .	92
7.4.2	The Changing States of <i>col11a2</i> mutant zebrafish . . . . .	93
7.4.3	Modelling the dynamics of <i>col11a2</i> mutant zebrafish . . . . .	94
<b>8</b>	<b>Conclusions</b>	<b>97</b>
<b>A</b>	<b>Appendices</b>	<b>99</b>
<b>A</b>	<b>Alternative 2D Image Analysis Methods</b>	<b>100</b>
A.1	Introduction . . . . .	100
A.2	Estimating Density Heterogeneity . . . . .	100
A.3	Estimating the Mobility . . . . .	101
A.4	Changing States of the Fish Group . . . . .	102
A.5	MIPS as a Possible Explanation . . . . .	102



# List of Figures

1.1 Randomly packed plastic balls . . . . .	1
1.2 The photo of a zebrafish . . . . .	2
2.1 The trajectory of a single active particle . . . . .	4
2.2 Trajectories of Active Particles . . . . .	5
2.3 Common phase diagrams of active matter . . . . .	6
2.4 Complex patterns formed by animals . . . . .	9
2.5 Locating a zebrafish in 3D . . . . .	9
2.6 Different phases revealed by two order parameters. . . . .	10
2.7 Examples of common correlation functions . . . . .	12
2.8 Examples of special correlation functions to characterise animals . . . . .	14
3.1 The morphological detail of a fish . . . . .	21
3.2 Two dimensional fish tracking appraatus . . . . .	21
3.3 Metrical rectification of an image. . . . .	23
3.4 Two dimensional image processing. . . . .	24
3.5 The correct label of overlapping fish. . . . .	25
3.6 Examples of segmented individual fish . . . . .	27
3.7 PCA analysis of the fish shape . . . . .	28
3.8 The feature tensor calculated with convolutional neural network . . . . .	29
3.9 The 2D spatial distribution of 1 adult zebrafish . . . . .	30
3.10 The 2D spatial distribution of two fish . . . . .	30
3.11 The 2D spatial distribution of three fish . . . . .	31
3.12 The 2D spatial distribution of 50 fish . . . . .	32
4.1 Three dimensional fish tracking system . . . . .	35
4.2 The concept of tracking one fish in 3D . . . . .	36
4.3 The concept of tracking many fish in 3D . . . . .	39
4.5 Three dimensional tracking result of simulated data . . . . .	41
4.6 Performance of the 3D locating method . . . . .	43
4.7 The 3D spatial distribution of one fish . . . . .	44
4.8 The 3D spatial distribution of two fish . . . . .	45
4.9 The 3D spatial distribution of three fish . . . . .	46
4.10 The 3D spatial distribution of 50 zebrafish . . . . .	47
4.11 The effect of drilled holes on the tank on the spatial distribution of the fish. . . . .	48
5.1 Removing the overlap particles with different algorithms . . . . .	53
5.2 Removing the overlap particles with soft constraint . . . . .	55
5.3 Linking locations into trajectories: concept illustration . . . . .	56

5.4	Comparing two linking algorithms . . . . .	57
5.5	The effect of relinking . . . . .	58
5.6	The joint probability density function ( $f_{XY}$ ) of $l_{nn}$ and $l_{ch}$ . The results were obtained from 3D experimental data of 50 adult zebrafish. . . . .	60
5.7	The structure of 50 zebrafish in 2D . . . . .	64
5.8	The dynamics of 50 fish in 2D . . . . .	65
5.9	The changing states of 50 zebrafish in a 2D experiment . . . . .	66
5.10	The structure of 50 fish in 3D . . . . .	68
5.11	The dynamics of 50 fish in 3D . . . . .	69
5.12	The changing states of 50 zebrafish in a 3D experiment . . . . .	70
5.13	The behaviour of 50 zebrafish described by reduced persistence length . . . . .	71
6.1	The 3D geometry of the experimental fish tank . . . . .	76
6.2	The distribution of ideal gas in the tank subjected to gravity . . . . .	77
6.3	The effect of the holes on the density distribution . . . . .	78
6.4	Fitting the $u(r)$ of fish with Eq. 6.6. . . . .	78
6.5	The effect of the pairwise interaction on the density distribution . . . . .	79
6.6	The parameter $p$ controls the size of the group. . . . .	79
6.7	Comparing the density distribution of the fish and the model . . . . .	80
6.8	The phase behaviour of the Vicsek model . . . . .	82
6.9	The scalar noise in the Vicsek model. . . . .	82
6.10	The effect of inertia in the Vicsek model . . . . .	83
6.11	The phase behaviour of the Vicsek model with inertia . . . . .	84
6.12	Comparing the dynamics of the zebrafish with the Vicsek model simulation . . . . .	85
7.1	Typical trajectories of the <i>col11a2</i> mutant zebrafish and the wildtype zebrafish . . . . .	89
7.2	The behaviour of one mutant fish and one wildtype fish . . . . .	90
7.3	The trajectories of 25 wildtype zebrafish and <i>col11a2</i> mutant zebrafish . . . . .	91
7.4	The Collective Behaviour of 25 wt fish and <i>col11a2</i> mutant zebrafish. . . . .	92
7.5	The changing states of 25 wt zebrafish . . . . .	93
7.6	The changing states of 25 <i>col11a2</i> zebrafish . . . . .	94
7.7	The behaviour of 25 zebrafish described by $l_{nn}$ and $l_p$ . . . . .	95
A.1	Dense regions in a group of fish . . . . .	100
A.2	Density Heterogeneity analysis of 100 zebrafish . . . . .	101
A.3	The mobility analysis of 100 zebrafish . . . . .	101
A.4	The changing macroscopic states of zebrafish . . . . .	102
A.5	MIPS like phase behaviour of zebrafish . . . . .	103

# List of Tables

5.1 Different Length Scales and Time Scales for 50 Zebrafish. . . . .	61
---	----

# List of Algorithms

1	Brute force algorithm for locate many fish in 3D . . . . .	39
2	Validate a 3D location with retraced error. . . . .	39
3	Validate 3D location with reprojection error. . . . .	40
4	Remove overlapping locations. . . . .	52
5	Greedy algorithm to remove overlapping locations. . . . .	53
6	The Simulation Procedure . . . . .	74

# List of Abbreviations

**TRS** time reversal symmetry 4

**Pe** Péclet number 5

**ABP** active Brownian particles 5

**MIPS** mobility induced phase separation 6, 100

**RDF** radial distribution function 11, 31

**ACF** auto-correlation function 13

**GUI** graphical user interface 20

**API** application programming interface 20

**PCA** principle component analysis 26

**SVD** singular value decomposition 27

**CNN** convolutional neural network 28

**PDF** probability density function 30, 43

**FPGA** field-programmable gate array 34

**MC** Monte-Carlo 73

**wt** wildtype 88

**dpf** days post fertilisation 89

# List of Symbols

<b>Notation</b>	<b>Description</b>	<b>Page List</b>
$\eta$	the noise term in the Vicsek Model	6, 82, 95
$N$	the number of particles/agents	10, 74, 103
$\Phi$	polarisation order parameter	10, 62, 93
$\mathbf{P}$	polarisation order parameter vector	10
$\mathbf{c}$	location of the centre	11, 37
$M$	milling order parameter	11
$\mathbf{M}$	milling order parameter vector	11
$g(r)$	radial distribution function	11, 31, 60
$\xi_\rho$	correlation length of the density	11, 60
$C(r)$	spatial correlation function	12
$\mathbf{o}$	orientation	12
$r$	distance between two particles	12
$C_{\mathbf{o}}(r)$	spatial correlation function of the orientation	12, 63
$\xi_{\mathbf{o}}$	correlation length of the orientation	12
$\chi$	susceptibility	13
$d$	dimension	13
$E$	energy	13
$J_{ij}$	coupling constant between two spins	13
$h$	external field	13
$C_{\mathcal{A}}(t)$	temporal correlation function of quantity $\mathcal{A}$	13, 62
$t$	time	13, 24, 50
$\tau_{\mathcal{A}}$	relaxation time of quantity $\mathcal{A}$	13, 62
$\mathbf{v}$	velocity	13
$C_{\mathbf{o}}(t)$	temporal correlation function of the orientation	14, 62, 90
$\gamma$	anisotropy factor	14
$n$	neighbour rank	14
$C_\gamma(n)$	correlation function of anisotropy factor	14
$C_{ij}(t)$	orientational cross-correlation function	14
$P$	pressure	16
$V$	volume	16, 76

<b>Notation</b>	<b>Description</b>	<b>Page List</b>
$T$	temperature	16
$S$	entropy	16
$\mu$	chemical potential	16, 54
$k_B$	Boltzmann constant	16
$\mathcal{W}$	internal pressure	16
$\mathbf{H}$	homography	23
$B_{ij}(t)$	the background video	24
$I_{ij}(t)$	the video from the camera	24
$F_{ij}(t)$	the foreground video	24, 100
$\sigma_{\text{blur}}$	standard deviation of the Gaussian kernel for blurring	24
$l_{\text{local}}$	length scale for the local threshold	24
$l_{\text{open}}$	length scale of the binary open operation	24
$T_{ij}$	fish shape template	25
$C_{ijo}$	Feature tensor including the locations and orientations of the fish	25
$C_{ijos}$	Feature tensor including the locations, orientations, and shapes of the fish	25
$C_{ij}$	Feature tensor including the locations the fish	29
$\mathbf{f}_i$	3D location of the 2D feature on the $i$ th camera	37
$\mathbf{x}_i$	3D location of the $i$ th fish	37
$\mathbf{P}_{3 \times 4}$	Projection matrix	37
$\mathbf{x}$	the 3D location of a fish	37
$\mathbf{a}_i$	the point where the retraced ray from the $i$ th camera and the water-air interface meets	37
$\mathbf{v}_i$	the retraced ray from the $i$ th camera after the refraction	37
$\mathbf{c}_i$	the centre of the $i$ th camera	38
$d_i$	the retraced error for the $i$ th camera	38
$\epsilon$	the reprojection error	40
$\{\mathbf{x}_{ijk}\}$	a collection of valid 3D locations from three view reconstruction	40
$\{\mathbf{x}_{ijk}\}_{\text{opt}}$	an optimised collection of valid 3D locations from three view reconstruction	40
$f_{XY}$	the joint probability density function of X and Y coordinates	43
$f_R(r)$	the probability density function of radius	43, 78
$f_Z(z)$	the probability density function of z coordinates	44, 78
$f_Z^{\text{ex}}(z)$	the excess probability density function of z coordinates	44
$\xi_g$	the effective gravitational length	44
$\hat{C}(k, t)$	spatial-temporal correlation function	50
$\xi$	the correlation length	50

<b>Notation</b>	<b>Description</b>	<b>Page List</b>
$\{\mathbf{x}\}_{\text{opt}}$	a collection of optimised 3D coordinates	51
$\{\mathbf{x}\}$	a collection of 3D coordinates	51
$K$	the number of non-overlapping particles	51
$\sigma$	the diameter of particles	52
$x_i$	an element in a boolean array for removing overlap particles	52
$\beta$	inverse temperature	54, 74, 77
$\Delta$	total squared movement of trajectories	56
$l_{\text{nn}}$	nearest neighbour distance	59, 73, 93
$d_{ij}$	distance between particle $i$ and $j$	59
$l_{\text{ch}}$	effective convex hull diameter	59
$f_d(r)$	the probability density function of pairwise distances	60
$\epsilon$	the effective attraction	61, 93
$v$	average speed	61, 93
$l_p$	persistence length	63, 73, 94
$C_v(r)$	spatial correlation function of the speed	63
$\kappa$	reduced persistence length, the ratio between the persistence length and the nearest neighbour distance	71, 73, 95
$\rho$	number density	74
$A(\zeta \rightarrow \nu)$	acceptance ratio from state $\zeta$ to state $\nu$	74
$Z$	partition function	77
$q$	the strength of the agent-hole interaction	78
$u(r)$	effective pairwise potential energy	78
$p$	the strength of the agent-agent interaction	79
$\mathbf{v}_i^t$	velocity of the $i$ th particle at time $t$	82
$S_i$	the set containing the neighbours of agent $i$	82
$\Theta$	operator to normalise a vector	82
$\mathcal{R}_\eta$	operator to rotate a vector randomly with noise level $\eta$	82
$\mathcal{V}$	velocity updating rule of the Vicsek model	82
$\rho_c$	density of the Vicsek model at the order-disorder transition	83
$\eta_c$	noise of the Vicsek model at the order-disorder transition	83
$\alpha$	inertial in the modivied Vicsek model	83, 95
$\mathcal{D}$	density heterogeneity of a group of fish	100
$\mathcal{M}$	total mobility for a group of fish	101

# Chapter 1

## Introduction

This thesis will discuss the *collective behaviour* of *zebrafish*. And we will start the thesis by describing the individual terms of our topic.

### 1.1 Collective Behaviour

When objects were densely-packed together, interesting phenomena appear. And we could call these phenomena as the *collective behaviour* of these things. The collective behaviour is interesting because “more is different” [5]. In other words, the behaviour of a large group can not be predicted, even if we know precisely the fundamental laws for the individuals.

An example to illustrate the complexity of collective behaviour, is a collection of randomly packed balls. When we randomly pack a lot of plastic balls together, they packed together like those in Fig. 1.1. These plastic balls, often modelled as *hard spheres*, have a simple property that two spheres can not be too close so that they overlap. Surprisingly, the accurate prediction of the density (expressed for example as the volume fraction) of the randomly packed hard spheres is still unachieved<sup>1</sup> [6, 10]. In addition, the well packed hard spheres form a collection of clusters with different geometrical features. In Fig. 1.1 two different clusters were highlighted. The prediction of the geometrical features is still a challenging problem [11, 12].

The collective behaviour of objects with varying length-scales were studied, from atoms, to colloids, animals, as well as human beings [13–17]. The interesting feature of their collective behaviour is the transformation from one phase to another under different conditions [18]. For instance, the water could change between the fluid phase and crystal phase under different temperatures. These behaviours are often noted as *phase behaviour*, and summarised by *phase diagrams*. The phase diagrams of systems in equilibrium have been systematically studied. However, the equivalent in non-equilibrium systems were less studied, and they will be introduced in chapter 2.

### 1.2 Zebrafish

Zebrafish (*Danio rerio*) is a small fish living mainly in India and Bangladesh, as well as in areas of Pakistan, Nepal, and Myanmar [19]. These fish are social animals that form small groups in the size of tens in still water [20]. In

<sup>1</sup> The latest progress about this problem was made by Zaccone [6]. But the proposed solution received many criticisms [7–9].



Figure 1.1: A photo of randomly packed plastic balls. The photo was taken by the author.

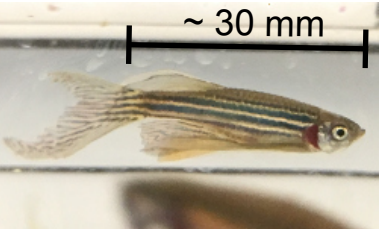


Figure 1.2: The photo of an adult zebrafish. The photo was taken by the author.

rivers with faster flow, the group size could be thousands [21]. The photo of a typical adult zebrafish is shown in Fig. 1.2, with the characteristic stripes of this species. Placing a group of these fish together, they will interact with each other, and often form a coherent group. These behaviours are what we will be studying through out this thesis.

Zebrafish receive attention from the scientific community, because they present a good animal model for different human diseases. Being a vertebrate, the genome of zebrafish is similar to that of human beings [22]. In addition, the embryo of zebrafish, as well as the zebrafish larva are transparent [23], making microscopic observation of cellular behaviour very easy. With the help of zebrafish, we could study common diseases such as the osteoarthritis [2, 24], autism [25], and cancer [3]. The appeal of zebrafish as an animal model makes them being widely used in different institutions[26]. Practically, the zebrafish in the laboratory were kept in a standard condition for many generations [27]. These fish are less likely to suffer from common diseases and parasites, comparing with wild captivated fish [26]. These fish are good for behavioural experiment as their living condition are controlled, which makes repeating experiments easy. In this thesis, all the zebrafish were bred at the fish facility of the University of Bristol.

There are multiple reasons to study the collective behaviour of the zebrafish. The first reason is technical. The fish naturally swim in the river, where they can change their depth every now and then. Observing the fish swimming in a three dimensional (3D) space requires advanced tracking system. The design and construction of such 3D underwater tracking system is a technical challenge. And it is meaningful to solve this challenge. In addition, understanding the behaviour of zebrafish could help us differentiate the states of the fish. And we will have predictive power about the fish behaviour, if we could construct a phase diagram of the fish. Finally, we may study the behavioural difference of the mutant zebrafish, to understand the consequences of genetic modifications.

### 1.3 Thesis Structure

In the next chapter the ideas of active matter and the collective behaviour of animals will be discussed. We will draw the similarity between a group of animal and a group of synthetic particles under constant energy input. Typically, we will stress the complex patterns formed by the animals. The statistical analysis of these patterns will be discussed, as well as some mathematical models that explained the behaviour.

The following two chapters, chapter 3 and 4, will address the technical challenges for the construction of a 3D fish tracking system. Firstly, the method to record the 2D movements of the zebrafish will be discussed in chapter 3. The important element in chapter 3 is the image processing methods, which enables us to extract features from the images. The density distribution of the fish in a quasi-2D environment will also be discussed in chapter 3. Then we will move to chapter 4, which discussed the construction of a 3D tracking system. This chapter will mainly feature different algorithms to calculate the 3D locations of the fish, following the ideas of multiple view geometry. The experimental results of 3D tracking will also

be discussed in chapter 4.

The tracking system will first produce the coordinates of the fish, which provides the information about the structure of the fish group. To study the dynamics of the fish, the coordinates needs to be linked into trajectories. The linking method will be introduced in chapter 5. From the trajectories, we can study the structure and the dynamics of the fish with analytical methods developed in the active-matter community. The analysis includes the calculation of different quantities that capture the essence of the fish behaviour, as well as the calculation of the *correlations* of different quantities. These analytical methods will be introduced, and applied to the experimental data. As a result, an important behavioural feature of the fish will be revealed in the end of chapter 5.

To further understand the fish behaviour, typically the analytical results, we will try to construct models that reproduced the behaviour. We will model the fish as identical agents following certain rules. We will make the model behave like the real fish, by adjusting the model parameters to match the analytical results. The fitted model will then serve as explanations for the observed results. Specifically, we will try to understand the density distribution of the fish, as well as the dynamics of the fish with different models.

Afterwards, we will move to a more biological topic and discuss the behaviour of zebrafish after genetic modification. In chapter 7, the collective behaviour of the mutant fish will be reported and compared against the normal, wildtype zebrafish. The mutant fish have a longer orientational relaxation time compared with the wildtype fish. The change in the single-fish property will affect the collective behaviour of the fish, making a group of mutant fish exhibiting more ordered movement, which can be explained by an active matter model from chapter 6.

Finally, we close the thesis with a conclusion that summarised all experimental observations, analytical results, as well as the models, and discussed possible future tasks to further improve our understand of the zebrafish behaviour.

## Chapter 2

# The Collective Behaviour of Animals as Active Matter

We declare that the splendour of the world has been enriched by a new beauty: the beauty of speed.

---

F. T. Marinetti  
*Manifesto of Futurism*

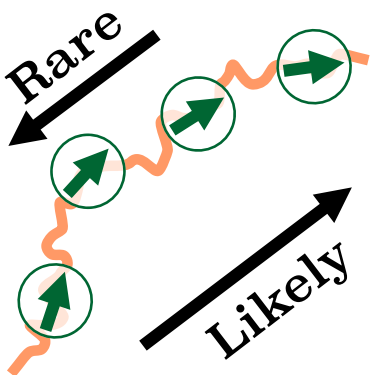


Figure 2.1: The trajectory of a single active particle, which breaks the time-reversal symmetry. The arrow in the circle represents the orientation of the particle, the direction of the self-propelling force.

### 2.1 Active Matter

This chapter would discuss the collective behaviour of *active matter*, focusing on the behaviour of *animals*. The term *active matter* refers to a class of non-equilibrium systems, whose constituting individuals constantly consume energy to generate systematic motion [28]. These individuals are called *active particles*, and they often propel themselves along the direction of their *orientations* [29].

#### 2.1.1 What is the activity?

Active particles are different from their passive counterpart in equilibrium systems, because of their “activity”. The activity could be defined, roughly as the ratio between the deterministic, self-propelling movement, and the stochastic movement from thermal fluctuation. The self-propelling movement breaks the time-reversal symmetry (**TRS**), making the movement of active particles special [30]. One example of how one active particle breaks the TRS is shown in Fig. 2.1. The self-propelling particle, represented by the circles in Fig. 2.1 would have an orientation vector, illustrated by the arrow Fig. 2.1. This orientational vector is an internal degree of freedom of the particle, like a spin carried by the particle. The particles would generate motion in the direction of their orientation vector, being self-propelling. An active particle is more likely to form a trajectory, where the particle is always moving along its orientation, rather than moving against its orientation. For instance, the orange line in Fig. 2.1 is more likely to be the trajectory of an active particle that is moving upwards, because the orien-

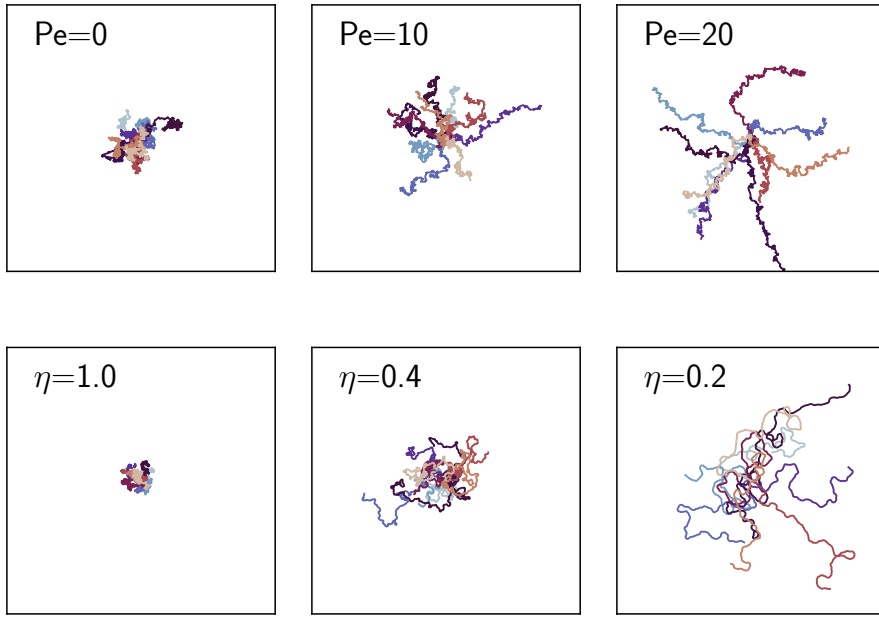


**Figure 2.2:** Trajectories of Active Particles. Top: the trajectories of active Brownian particles (ABP) with different Péclet numbers ( $\text{Pe}$ ). Bottom: the trajectories of Vicsek agents with different noise ( $\eta$ ) values. Each subplot presents the simulated trajectories of 10 particles.

tations of the particle are pointing at similar directions. It is very unlikely to observe a particle to form such trajectory by traveling from upper right to lower left, if the particle is active<sup>2</sup>. In the absence of activity, where the particle is in equilibrium, the two different options in Fig. 2.1 would have the same probability.

The Péclet number ( $\text{Pe}$ ) is often used to quantify the activity of the particles [31]. It is defined as the ratio between the driven, deterministic motion, and the random, diffusive motion. It is easy to grasp the effect of activity visually, by inspecting the movement of particles with different  $\text{Pe}$  values. The trajectories of these particles were plotted in Fig. 2.2. When  $\text{Pe} = 0$ , the particles perform Brownian motion [32], and they explore a smaller area in the space, having very zigzag and twisted trajectories. As the value of  $\text{Pe}$  increased, the trajectories appear more straight, and the particles explore more spaces.

An alternative way to keep track of the activity, is to specify the randomness directly. For instance, we could rotate the moving direction of the active particles randomly, to interrupt their otherwise ballistic self-propelling movement. A system with large noise value therefore would have a low  $\text{Pe}$  number, hence low activity. The effect of the noise is shown in Fig. 2.2. When  $\eta = 1$ , the rotation is totally random, corresponding to the situation when  $\text{Pe} = 0$ . By reducing the noise, the particles explore more spaces, being more active.<sup>3</sup>

### 2.1.2 What does active matter do?

The reason we focus on the two aspects of the activity, is related to the two famous models for the active matter. One of the model is the active Brownian particles (ABP), where the active particles interact with each other via a short-ranged repulsive interaction. The activity of the active Brownian particles is often represented by the Péclet number [29, 33, 34].

<sup>2</sup> It is still possible for the rare situation to happen, but the motion had to be driven by randomness. For instance, an active colloids might move against its propelling force, because of the random kicks from solvent molecules.

<sup>3</sup> It is important to emphasise that the noise term  $\eta$  is exclusively used for the Vicsek model, without being referred to as the activity.

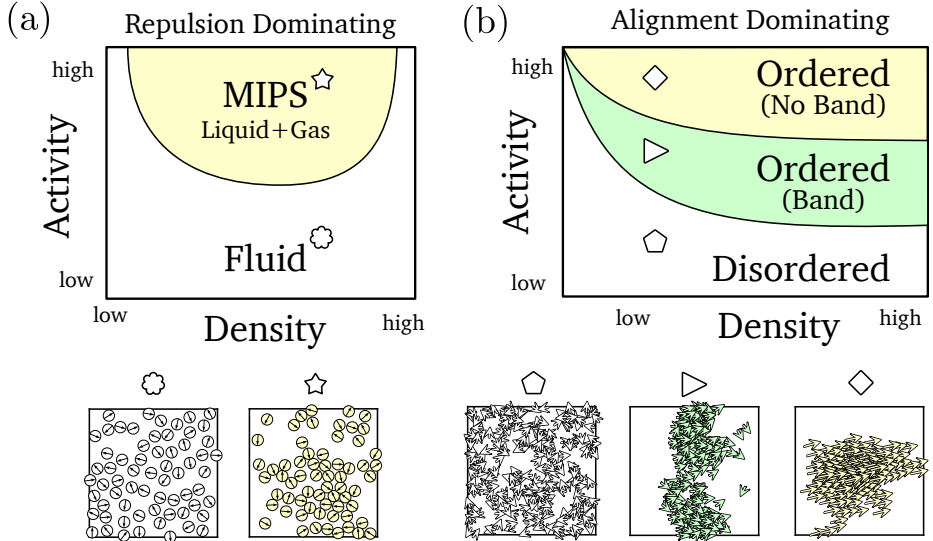


**Figure 2.3:** Two types of common phase diagrams of active matter. (a) The phase diagram of active matter systems where the short-range repulsive interaction is dominating. These systems exhibit liquid-gas separation at high level of activity. (b) The phase diagram of active matter systems where the velocity-alignment interaction is dominating. These systems exhibit a flocking transition at high activity levels and large density values.

<sup>4</sup> We committed to follow Toner et al., calling the *non-equilibrium steady state* with an underlying symmetry a “phase”. In the active matter community, this usage of the term “phase” is widely accepted.

Another widely used model for active matter is the Vicsek model, where the active particles align their orientations with nearby neighbours. The activity of particles in the Vicsek model is often controlled by the noise term  $\eta$  [35–37].

These two models revealed two important phase<sup>4</sup> behaviours of active matter, which are summarised in Fig. 2.3. It is important to stress that the two phase diagrams are sketched in a qualitative way, and some details are ignored. Nevertheless, the phase diagrams are consistent with simulations results, for both 2D and 3D systems [34, 35, 39–41].

For the active matter system whose interaction is dominated by short-range repulsion, its behaviour can be summarised in Fig. 2.3 (a). While the activity is low, the system forms a fluid with a uniform density distribution, like the behaviour of hard disks (in 2D) [39, 42, 43] or hard spheres (in 3D) [12, 34, 39]. With high activity values, the active particles begin to phase separate into high density “liquid” and low density “gas”, a phenomena known as the *mobility induced phase separation* (MIPS) [34, 44–46]. MIPS is reminiscent of the liquid-gas coexistence in equilibrium systems with attractive interactions [47–49]. This similarity is indeed surprising: the activity seems to cause an effective attraction between particles [34]. The apparent attractive interaction could be explained by a feedback loop, where the active particles slows down when they accumulate, and the slowing down also induces accumulation of more particles [45].

On the other hand, for active particles that align their orientation with nearby neighbours, instead of repel each other, their phase behaviour could be summarised in Fig. 2.3 (b). In the low activity and low density region, the particles perform disordered movements like the ideal gas. However, with increasing activity and density, the system would undergo an order-disorder transition<sup>5</sup>, where all the particles would share the same moving direction, with slight perturbations from the rotational noise [35, 40]. The ordered phase in Fig. 2.3 (b) could further be divided into two distinct kinds. When the activity is moderate, the active particles “travel in bands” [54], featuring dense stripes separated by dilute regions, as shown in Fig. 2.3 ( $\triangleright$ ). With high activity, the particles do not travel in bands, but rather

<sup>5</sup> The transition is also called the *flocking transition* in some literatures [50, 51]. The phenomena where particles perform ordered movement is sometimes called flocking [52, 53].

form a coherent cluster, shown in Fig. 2.3 ( $\diamond$ ). The banding phase is an important structural feature of active matter with alignment interactions, which is observed in colloidal experiments [33, 55, 56].

There are more types of interactions beyond repulsion and alignment. Active matter with more complex interactions exhibits rich behaviours. For instance, the incorporation of pairwise alignment, short-ranged repulsion, and long-ranged attraction leads to a complex phase behaviour including the fluid, the moving crystal, as well as the polar bands [33]. The combination of short-ranged repulsion, and dipole-dipole interaction coupled with an alternating current electric field leads to the formation of labyrinth-like patterns [57]. In addition, the vision-based acceleration could lead to the formation of a cohesive cluster [58], as a new mechanism beyond of pairwise attraction and MIPS.

It is important to point out that there are topics of active matter that are not covered in this section. For instance, we did not discuss the apolar active matter with nematic alignment interaction [41, 59, 60]. In addition, the effect of activity on the crystallisation [43, 61, 62] and glass transition [63, 64] is not discussed. We also downplayed the importance of dimensionality, which changed the phase diagram of significantly [62, 65].

Finally, we want to specify the meaning following terms, because they were originally developed in equilibrium statistical mechanics. And applying these terms for active matter could cause confusion.

### Phase

The non-equilibrium steady state with an underlying symmetry, for systems in the thermodynamic limit where the number of particles  $\rightarrow \infty$ .

### Microscopic State

Here we refer to the locations, velocities, and orientations of all the active particles.

### Macroscopic State

Here we refer to a few global variables, like the density and activity, for an active matter system.

### Collective

We use the term to specify the property exhibited by a group of animals, in contrast to the property exhibited by individuals.

### Collective Behaviour

The macroscopic states exhibited by an active matter system.

### Collective Motion

The microscopic states of an active matter system.<sup>6</sup>

It is notable that the meaning of these terms is different in different fields. But they will be consistent in this thesis.

<sup>6</sup> For a group of fish, we can directly observe their collective motion, and study their collective behaviour by further analysis.

### 2.1.3 Animals as Active Matter

A group of animals is a typical active matter system, as each individual spends their energy to perform movement [28]. Consequentially, the two typical phase behaviour of active matter, presented in Fig. 2.3, has been observed in animal groups. For instance, the MIPS-like behaviour, where a dilute region and a dense region coexist, was observed in a group of beetles [66]. In addition, European Starlings exhibit ordered movement [67], while the midges exhibits the disordered movement [68]. From a group of zebrafish, we also observed the order-disorder transition [1], which will be discussed in chapter 5.

There is an implicit paradigm to study the active matter system in the scientific community [69], which includes three steps. Firstly we observe the behaviour of real animals and calculate their behavioural features. Then we simplify the animals with a mathematical model that captured all the essential features [70]. Finally we study the model either numerically or analytically, to have a comprehensive understanding. An example of this approach, was recently demonstrated by Bull and Prakash with a trilogy<sup>7</sup> on the movement of cilia [71, 73, 74]. It is important to stress that the research on active matter does not always follow the order of “observation, model, and theory”, even though we will review the literature in such order.

<sup>7</sup> The authors explained their work in a series of helpful tweets [72]. A tweet is a text snippet people posted on a website named “Twitter”.

## 2.2 The Observation of Animal Behaviour

Observing the collective motion of animals is a visually pleasing task, since a group of animals could form striking patterns in nature [75]. It is expected that animals could do more interesting things, compared with the behaviour of simple active matter systems introduced in section 2.1.2. This is because the interaction between the animal individuals is based on vision [76], sound [77], and smell [78]. All of these biological sensors makes the interaction of animals being more complex than a combination of repulsion and the velocity alignment.

### 2.2.1 Complex Patterns Seen in Nature

Even the visual footages of the animal behaviour, like the photos and the videos, are useful information. For instance, the early active matter models were aiming at simulating the movement of animals with visual similarity, rather than quantitative agreement [35, 79, 80]. Two typical complex patterns commonly seen in the nature were presented in Fig. 2.4. The first kind is flocking birds, which form a coherent cluster with a smooth but irregular shape (Fig. 2.4, left subfigure). Another kind of pattern were formed by a school of fish, where the fish rotates around a common axis collectively (Fig. 2.4, right subfigure), exhibiting a “milling” behaviour.

### 2.2.2 Observing the Collective Motion in 2D

To understand the animal behaviour in more detail, it is important to go beyond the visual inspection, and perform quantitative measurement. One popular option to study animal behaviour is to analyse videos, recorded

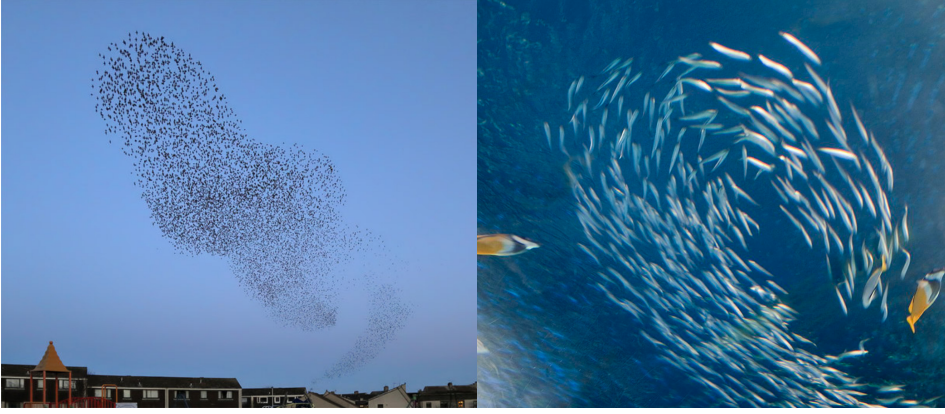


**Figure 2.4:** Photos of complex patterns formed by animals. Both photos were distributed under the Creative Commons Licence. Left: the murmuration of flocking European starlings. Each dark dot represents a bird. The photo was taken by [Walter Baxter](#) in Eye-mouth, Scotland. Right: a school of prey fish forming a circle, as a defensive move against two nearby butterfly fish. The photo was taken by an Internet user named “[life-fish](#)”, a semi-pro photographer.

with conventional cameras, which capture the movement of animals in 2D. Both the flocking behaviour and the milling behaviour, shown in Fig. 2.4, were observed from these 2D videos. For examples, there are analyses on the behaviour of locusts [81, 82], fish [15, 83–85], penguins [86, 87], and many other animal species [88–91].

As a well developed experimental technique, the 2D tracking of animals is an easy task. There are multiple free and user-friendly softwares available online, enabling researchers to carry out 2D tracking tasks [92–95]. The performances of various tracking softwares were quantified in a recent comprehensive review [96]. In addition to cameras, there are alternative technologies for the study of animal behaviour. For instance, Makris et al. used a waveguide remote-sensing technology to record the density distribution of fish shoals at the scale of kilometers [97, 98]. The GPS is also another option to tag individual animals, and obtain trajectories [99].

### 2.2.3 Observing the Collective Motion in 3D

The idea of tracking the movement of animals in 3D, with the help of cameras, was proposed early in the 1960s [100, 101]. The fundamental principles to carry 3D tracking were covered by the multiple view geometry in the computer vision community [102]. Very briefly, the picture in one 2D image offered two constraints on the 3D coordinates of an object. Therefore, 3D coordinates can be determined with images from two or more cameras [103]. Figure 2.5 sketched an example for this idea.

Even though the idea is simple, setting up a 3D tracking experiment and obtaining long trajectories of multiple animals are still challenging [104]. Multiple new algorithms have been proposed to tackle the various issues during the tracking process. These issues includes the calibration of camera during field study [103, 105], the visual occlusions where two animals overlap in the image [106], the ambiguity for the stereo matching of trajectories in multiple views [107], and the recovery of identity information given the coordinates in different time points [108, 109].

Despite the technical challenges, the 3D tracking of birds [103, 110–112], insects [113–117], as well as fish [1, 118, 119] were reported. For the birds, the order “flocking” phenomena were observed in [67, 105, 110, 120]. For the midges and the fish, the observed movements were disordered [1, 68, 116].

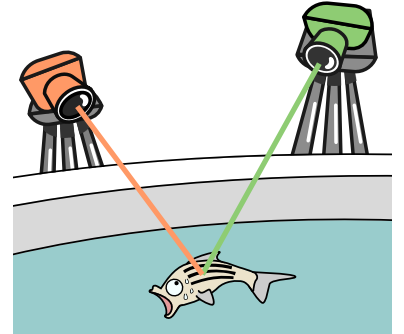


Figure 2.5: Schematic illustration for locating a zebrafish in 3D with two cameras.

<sup>8</sup> I was told that the lack of long trajectory is the reason why the author of [121] chose midges over birds.

There are still two major technical challenges for the 3D animal tracking problem. Firstly, it is very hard to track a large flock of birds for a long time, because the flock would move outside the view of the cameras quickly. This is the reason some of the large scale statistical analysis are only performed on midges [121], rather than the birds<sup>8</sup>. There is a recent breakthrough to track birds for a long period of time, by moving the cameras in a synchronised fashion [122], but no experimental results were reported from the new system so far. Another challenge is the 3D tracking of a large school of fish in the sea, which requires underwater equipments. In fact, there is still no quantitative field observation for the a large amount of fish in the milling phase, like those in Fig. 2.4. Recently, the underwater 3D tracking methods were being developed [123, 124], but only for fish groups with small sizes ( $N < 10$ ).

## 2.3 The Analysis of the Collective Motion

Analysing the animal movement involves two major steps. Firstly, we need to identify the different kinds of behavioural patterns of the animals, and assign the patterns to different phases. For patterns in a particular phase, we can study its feature with different correlation functions.

### 2.3.1 Identifying Behavioural Patterns with *Order Parameters*

This classification of different phases is important, because different phases have different properties. We can use an *order parameter*, which indicates the breaking of one kind of symmetry [18], to identify different phases. For instance, we could define the vector sum of the orientation of each individual as a order parameter ( $\mathbf{P}$ ) [35]:

$$\mathbf{P} = \frac{1}{N} \sum_i^N \mathbf{o}_i \quad (2.1)$$

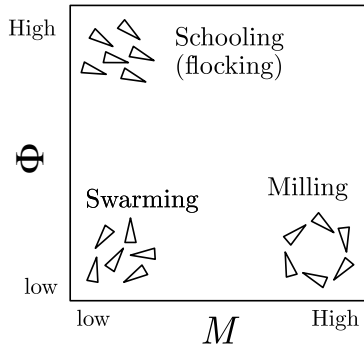


Figure 2.6: The schooling, milling, and swarming phases described by two order parameters. The parameter  $\Phi$  indicates the degree of synchronised movement, while the parameter  $M$  indicates the existence of collective rotation.

where  $\mathbf{o}_i$  is the orientation of the  $i$ th individual in a group with  $N$  members. We use symbol  $\Phi$  to represent the norm of the vector  $\mathbf{P}$ . For a very large group, the value of  $\Phi$  would approach zero if the orientations of the individuals were completely de-correlated. On the other hand, the value of  $\Phi$  would tend to unity if all the individuals have the same orientation. In the latter case, the rotational symmetry is broken because the group has one single moving direction, where the vector  $\mathbf{P}$  is pointing at. The order-disorder transition in Fig. 2.3 (b) is characterised by a discontinuous change of  $\Phi$ . For a flock of birds moving towards the same direction, the value of  $\Phi \sim 1$  [111]. For a swarm of randomly moving midges, the value of  $\Phi \sim 0$  [68].

The milling behaviour of the fish, shown in Fig. 2.4, needs a different order parameter that focuses on the angular momentum of each fish. This order parameter is written as,

$$\mathbf{M} = \frac{1}{N} \sum_i \left( \mathbf{o}_i \times \frac{\mathbf{r}_i - \mathbf{c}}{|\mathbf{r}_i - \mathbf{c}|} \right)$$

where  $\mathbf{r}_i$  represent the location of the  $i$ th individual, and  $\mathbf{c}$  represents the location of the group centre. Again, we use the symbol  $M$  to represent the norm of  $\mathbf{M}$ . For a group of fish that are rotating around a common axis, the value of  $M$  would be close to one [80, 125]. For the system that does not perform the collective rotation, the value of  $M$  would approach zero.

With the two order parameters, the behavioural pattern of the fish, as well as other species, could be categorised into the swarming, the milling, and the schooling phases, as shown in Fig. 2.6. The existence of these phases were observed in the a group of golden shiners (*Notemigonus crysoleucas*) [126]. Operationally, establishing the order parameters helps the identification of the phase that the experimental data (or simulation results) belongs to, without visual inspection.

Inside each phase, we could study its feature by examining the *correlations* in the time and in the space [127]. The spatial correlations gives us information about the structure of the animal group, while the temporal correlations reveals the dynamics of the system.

### 2.3.2 Probing the Structure: the Radial Distribution Function

The radial distribution function (RDF)<sup>9</sup> can be used to reveal the structure of the animal group. An example of the RDF, also known as the  $g(r)$ , is shown in Fig. 2.7 (d). This RDF probes the structural features of a system shown in Fig. 2.7(a). The value of  $g(r)$  at very short range is zero, which represents the short ranged repulsion. The location of the peak of the  $g(r)$  is a proxy to the nearest neighbour distance, while the height of the peak indicate the cohesiveness of the group [128]. The slow decay in Fig. 2.7 shows the presence of large clusters in Fig. 2.7(a). The size of these large clusters can be captured by the  $r$  value when  $g(r)$  decays to zero. This distance value is called *correlation length* of the density  $\xi_\rho$ .

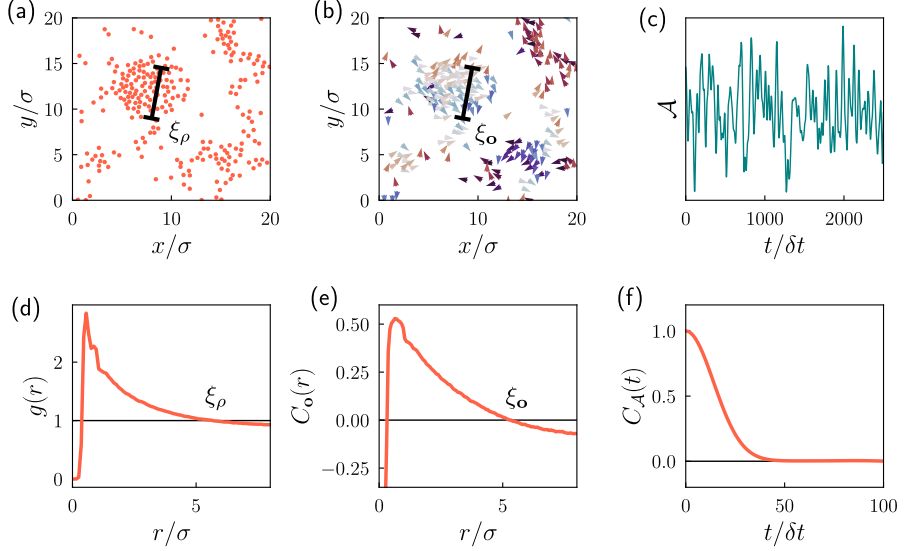
Notably, the RDF is an important tool for the study of the fluid in equilibrium, because it determines the thermodynamic behaviour of the system [128, 129]. For instance, the internal energy, the pressure, and the compressibility can be calculated from  $g(r)$ . However, this validity does not hold for animal groups due to their non-equilibrium nature<sup>10</sup>. Nevertheless, the RDF is still a very useful tool to characterise the structure of animal groups, which had been applied to study the fruit flies [90], birds [131], the fish [132], and the penguins [87].

Finally it should be mentioned that the  $g(r)$  is a two point correlation function, which is not aware of the possible many-body correlations. It was recently revealed by Kürsten et al. that higher order correlations are important for the alignment dominating system [133], typically the ordered phase in Fig. 2.3 (b). The measurements of higher order correlation functions is rare in the study of animal behaviours, but the tools are available in the studies of liquid [134–136]. Biologically, the existence of high order structure would be expected. For instance, the formation of the typical V-shape pattern [137] for a flock of geese could not emerge as a result of simple pairwise interaction.

<sup>9</sup> The radial distribution function is also named  $g(r)$ , which is read as the “ $g$  of  $r$ ”. We use the term RDF and  $g(r)$  interchangeably in this thesis.

<sup>10</sup> Recent study suggested that the  $g(r)$  can be used to calculate the compressibility for active Brownian particles [130].

**Figure 2.7:** Examples of common correlation functions and the structure/dynamics that they probe. (a) The coordinates of 256 particles with short-ranged repulsion and alignment interaction. (b) The orientation of the particles in (a) represented as arrows located at their corresponding coordinates. (c) A time series signal of quantity  $\mathcal{A}$ . (d) The radial distribution function ( $g(r)$ ) calculated from the model that generated (a) and (b). (e) The connected correlation function of the orientations of particles calculated from the model that generated (a) and (b). (f) The auto-correlation function of the signal shown in (c).



#### Implicit Assumption of the Pairwise Distance $r$

Using the scalar variable  $r$  in a correlation function, we implicitly assumed two conditions. Firstly, the interaction of two particles only depends on their relative distance. In other words, the interaction should be spherically symmetrical. In addition, we assume the system is isotropic with translational symmetry. Therefore, shifting two particles together would not affect their interaction. Without these assumptions, the correlation should be changed from  $g(r)$  or  $C(r)$  to  $g(\mathbf{r}_1, \mathbf{r}_2)$  or  $C(\mathbf{r}_1, \mathbf{r}_2)$ .

### 2.3.3 Probing the Dynamics: the Correlation function of Orientation

For a group of animals, as well as other active matter systems, their dynamical features are important. To characterise the dynamics, we can calculate the correlation of the orientations ( $\text{o}$ ) of each animal at different distances ( $r$ ). An example of such a correlation function,  $C_o(r)$ , is shown in Fig. 2.7 (e), which characterised the local alignment of particles in Fig. 2.7 (b). These particles are shown to align with nearby neighbours, exhibiting a positive value in the correlation value at short distances. The correlation function reaches 0 at a distance  $\approx 5\sigma$ , corresponding to the correlation length of orientation ( $\xi_o = 5\sigma$ ). If we compare the correlation functions from both Fig. 2.7 (d) and (e), it is obvious that the two correlation lengths,  $\xi_\rho$  and  $\xi_o$ , are similar. This means the large clusters in Fig. 2.7 (a) and (b) move together, thanks to the local alignment of particles which leads to effective attraction.

Orientational correlation functions are widely applied in the study of animal behaviour, particularly for systems where alignment is the dominating interaction. For instance, the orientational correlation functions of midges

[68, 138], fish [1], and birds [67] have been reported, presenting short or long ranged orientational correlations.

This function is important also because its integral,  $\int C_{\mathbf{o}}(r)dr$ , is related to the *susceptibility* ( $\chi$ ) of the animal orientation under an external perturbation, under two assumptions. Firstly, the alignment interaction should dominate the animal behaviour, so that the energy<sup>11</sup> of the system  $E$  follows,

$$E = - \sum_{i,j} J_{ij}(\mathbf{o}_i \cdot \mathbf{o}_j) - h \sum_i \mathbf{o}_i \quad (2.2)$$

where  $\mathbf{o}_i$  is the orientation of the  $i$ th member in the group,  $J_{ij}$  is a coupling constant for a pair of member  $i$  and member  $j$ , and  $h$  represents the effect of an external field affecting the individuals' orientations. With the energy term, it is further assumed that the system is in equilibrium, where the entropy is maximised [141], so that the probability of the system in a microscopic state with energy  $E$  is,

$$P(E) = \frac{\exp(-\beta E)}{\int \exp(-\beta E)},$$

where the integral in the denominator yields the *partition function* of the system. These two assumptions ignored many biological details of the animals, but were confirmed to fit the experimental data [141].

Acknowledging the two discussed assumptions, the relationship between  $C_{\mathbf{o}}(r)$  and  $\chi = \langle \partial\Phi/\partial h \rangle$  can be derived with the linear response theory<sup>12</sup> [68, 140]. The susceptibility is biologically important, because it could be related to the ability of each individuals to change their moving direction, under the influence of a predator (which generates the field  $h$  in Eq. 2.2). And it is been utilised in the study of midges by different research groups [68, 142].

### 2.3.4 Probing the Dynamics: the Auto-Correlation Function

Another way to probe the dynamics of the system is to calculate the auto-correlation<sup>13</sup> function (ACF). We use the notation  $C_{\mathcal{A}}(t)$  for the ACF for quantity  $\mathcal{A}$ , whose value typically fluctuates at different time points, like the signal in Fig. 2.7 (c). The corresponding  $C_{\mathcal{A}}(t)$  is shown in Fig. 2.7 (f), which decays from one to zero. The value of  $C_{\mathcal{A}}(t)$  indicates the average similarity of the signal to itself after some lag time  $t$ . The auto-correlation function in Fig. 2.7 (f) indicates that the system forgets its microscopic state, characterised by  $\mathcal{A}$ , after  $50 \delta t$  (the time unit). This timescale is called the *relaxation time*, noted by  $\tau_{\mathcal{A}}$ . Knowing the values of relaxation time for different features let us grasp the dynamics of the system, typically for the identification of fast process and slow process. For instance, the orientational relaxation time of the fruit flies [90] and fish [144–146] were estimated from the ACFs.

Beyond the determination of relaxation time, the ACF is important because its integral relates to the transport coefficient, a relation known as the Green-Kubo formula [69, 147]. For instance, the integral of the ACF of the velocity ( $\mathbf{v}$ ),  $\int C_{\mathbf{v}}(t)dt$  yields the diffusion coefficient. However, this relation requires the collective motion of the animals, treated as a stochastic

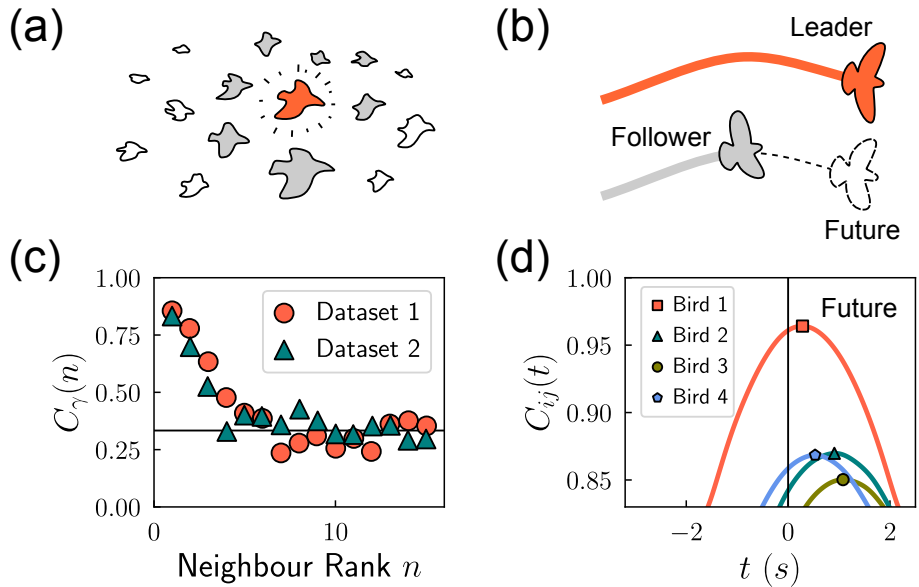
<sup>11</sup> The “energy” in Eq. 2.2 ( $E : \mathbb{R}^{N \times d} \rightarrow \mathbb{R}$ ) is effectively a function that maps the  $d$  dimensional orientations of  $N$  individuals to a probability weight. It is more likely to observe an animal group with a lower energy value.

Notice the similarity of Eq. 2.2 to the energy function (the *Hamiltonian*) to those in magnetic systems, for instance the Ising model and the spin glass [139, 140].

<sup>12</sup> The susceptibility can also be obtained from the fluctuations of the polarisation order parameter ( $|\mathbf{P}|$ ). Practically, estimating the susceptibility with  $\int C_{\mathbf{o}}(r)dr$  is better for experimental data, because this route suffers less from measurement error and finite trajectory length [115].

<sup>13</sup> The prefix “auto” comes from Greek word *autos*, which means “self” [143].

**Figure 2.8:** Examples of special correlation functions to characterise animals. (a) The illustration of a topological interaction, where a highlighted focal bird interact with 7 nearby neighbours, regardless of the distances. This topological interaction is supported by correlation function  $C_\gamma(n)$ . (b) The sketch of a leading bird and a following bird. The following bird will align with the leader, after a short lag time. The leadership is supported by correlation function  $C_{ij}(t)$ . (c) The anisotropy correlation function  $C_\gamma(n)$  of the European starlings. The data was obtained from [120]. (d) The orientational cross-correlation function  $C_{ij}(t)$  between a pigeon and its group members. The data was obtained from [110].



process, to be second-order stationary, where the ACF does not change with time. In chapter 5, we will see that this assumption is not true for the fish, as the  $C_o(t)$  of 50 zebrafish changes with time.

### 2.3.5 Novel Correlation Functions for Animals

It is possible to craft novel correlation functions, like the  $g(r)$ , to study the structural features of animal groups. For example, Ballerini et al. studied the distribution anisotropy of the neighbours of each bird in a group of European starlings [120]. This anisotropy factor, noted as  $\gamma$  in [120], could be used to construct a correlation function  $C_\gamma(n)$ , with different neighbours rank ( $n$ ) values<sup>14</sup>, shown in Fig. 2.8(a). This function  $C_\gamma(n)$  presents the decay of  $\gamma$  with increasing  $n$  values, and leads to a remarkable conclusion: a bird in a flocking group interacts with 7 neighbours on average [120, 148], regardless of its distances to these neighbours. This behavioural feature is called a *topological* interaction, as opposed to a metric interaction based on physical distances. This special correlation function was also used by Ling et al. to study the changing behavioural rules of jackdaw flocks [149].

The correlation function  $C_{ij}(t)$  is another tool to study animals, proposed by Bumann and Krause [150] in 1990s, and revisited by Nagy et al. in 2010 [110]. It is essentially the orientational cross-correlation between two individuals (labelled as  $i$  and  $j$ ) in time. Such function revealed the leader-follower relationship among the individuals in the group. An example is plotted in Fig. 2.8 (b), where a following bird would try to align its orientation to a leader. Because of the behavioural inertia of the birds, there will be a slight lag time, for the follower to adjust its orientation. In other words, the follower will try to align with the leader “now”, but the alignment is not instantaneous, and it could only happen in the “future”. This lag time could be captured by the orientational cross-correlation function

$$C_{ij}(t) = \langle \mathbf{o}_i(\tau) \cdot \mathbf{o}_j(\tau + t) \rangle, \quad (2.3)$$

<sup>14</sup> For a bird, its nearest neighbour has the rank 1, the next nearest neighbour has the rank 2. The value of  $\gamma$  for the  $n$ th nearest neighbour is calculated for the entire animal group, in order to quantify the fact, that the neighbours are less likely to be distributed in the moving direction of the group. Specifically,  $\gamma(n) = \mathbf{w}(n) \cdot \mathbf{P}$ . The vector  $\mathbf{w}(n) \in \mathbb{R}^{m \times 3}$  is the eigenvector of the matrix  $\mathbf{M}(n) = \mathbf{u}(n)^\top \cdot \mathbf{u}(n)$ , and  $\mathbf{w}(n)$  corresponds to the smallest eigenvalue. The vector  $\mathbf{u}(n) \in \mathbb{R}^{m \times 3}$  stores all the unit vectors pointing from all  $m$  birds in the group, to their  $n$ th closest neighbours. The vector  $\mathbf{P} \in \mathbb{R}^3$  is the polarisation order parameter defined in eq. 2.1.

where the angular brackets  $\langle \dots \rangle$  represents a time average. Examples of such cross-correlation functions, calculated from pigeons, are shown in Fig. 2.8 (d). For a leading bird, the cross-correlation with its follower would lead to a peak at  $t > 0$ , because the follower's alignment would happen in the future. This leader-follower relationship of pigeons was also observed by Chen et al. [151]. And this correlation function as used by Yomosa et al. for the study of gulls [152].

Finally, we want to mention a recent method to quantify the hidden order [153], and its correlation length [154]. This method used the compression algorithm in computer science to quantify the entropy, as the information with high entropy could not be compressed effectively [155]. This method was demonstrated to be useful for the study of both kind of active matter systems in Fig. 2.3 [50, 153].

## 2.4 Understanding the Animal Behaviour

The order parameters, and the correlations calculated from a group of animal can be used to construct mathematical models. These models can be studied numerically or analytically, to make predictive conclusions about the animal behaviour.

### 2.4.1 Microscopic Approach: Agent Based Models

The most famous model in the active matter community is arguably the Vicsek model proposed by Vicsek et al. in 1995. The model assumed the individual animal in a group align with nearby neighbours. This alignment process is interrupted by the orientational noise ( $\eta$  in Fig. 2.2). The phase diagram in Fig. 2.3 (b) depicted the behaviour of the Vicsek model. The movement of active particles in the ordered phase is visually similar to the collective motion of birds shown in Fig. 2.4 [156].

The Vicsek model is a very simple model, which often lack essential elements to reproduce the behaviour of animals accurately. For instance, the lack of inertia in the Vicsek model makes it incapable of describing the collective turning behaviour of European Starlings [111]. To explain the experimental results, an inertial spin model [111, 157] was proposed. In addition, the topological interaction rule [120], shown in Fig. 2.8 (a), could also be added into the Vicsek model, which suppressed the travelling bands<sup>15</sup>.

The milling behaviour of the fish [126], shown in Fig. 2.4 was also modelled by Couzin et al. in early 2000s, known as the Couzin model. This proposed model includes a short ranged repulsion, with an alignment interaction in intermediate range, as well as a long-ranged attraction [80]. All the phases introduced in Fig. 2.6, the schooling, milling, and the swarming, can be reproduced in the Couzin model [126]. The same phases could also be reproduced in a model with topological interaction rules [125, 162], as well as a model with only local attraction interactions [163].

### 2.4.2 Hydrodynamic Approach: Continuum Models

One further step to understand the animal behaviour is to convert the microscopic description of the individuals, into large scale, *hydrodynamic*

<sup>15</sup> The existence of the bands for the topological Vicsek model is still under scrutiny. Early results, both simulations and theories, suggested the absence of the band [53, 158, 159]. But recent simulations and theories suggested the existence of the band [160, 161].

<sup>16</sup> Also known as the continuum models.

models<sup>16</sup>. By doing so, we ignored the details of the particles, and treat the system as flowing liquid. This approach is demonstrated by Toner and Tu, who derived qualitative predictions for the large scale behaviour of active particles, from hydrodynamic equations. Typically, these hydrodynamic equations describe the evolution of density field and the polarisation field ( $\mathbf{P}$  in Eq. 2.1), in the form of coupled partial differential equations [52, 164, 165]. The hydrodynamic description of active matter are expected to recreate the result of the microscopic model at a large-scale [166]. The introduction of various continuum models is beyond the scope of this thesis, but we want to discuss some predictive conclusions from theoretical analysis of these models.

The major conclusion from Toner and Tu in their early analysis is that the ordered phase discovered by Vicsek et al., shown in Fig. 2.3 (b), exists in 2D. This confirmation is important because the ordered phase could not be proved by numerical simulation in the computer<sup>17</sup>. In addition, the analysis carried out by Mermin and Wagner [169] explicitly ruled out the possibility for the long ranged order in 2D in equilibrium [18, 170]. In other words, the activity of particles in the Vicsek model is surprisingly crucial for the flocking phenomena.

Beyond the existence of the ordered phase in the 2D Vicsek model (Fig. 2.3), the analysis of the continuum models also yields other useful results such as the scaling of velocity correlation function and the discontinuous nature of the order-disorder transition [40, 160]. However, as Ouellette commented recently, it is challenging to link the continuum models to animal groups, especially to compare the theoretical prediction with experimental results, due to the lack of large scale experimental results [171].

#### 2.4.3 Thermodynamic Approach: Equation of State

It is also possible to take a *thermodynamic* approach to study the animal behaviour. Thermodynamics is capable of describing the behaviour of equilibrium systems, whose underlying microscopic dynamics are unknown [171]. For instance, the laws of thermodynamics were established and applied, long before the discovery of atoms and before the development of statistical mechanics [18, 171]. To do something conceptually similar, we will need to define some *state variables*, which are conceptually similar to the pressure ( $P$ ), volume ( $V$ ), temperature ( $T$ ), entropy ( $S$ ), chemical potential ( $\mu$ ) and particle number ( $N$ ), to summarise the behaviour of animals. If the animals were behaving in an equilibrated way, these state variables would be constrained, yielding an equation of state, that would be useful to develop predictive theories.

For instance, the *virial equation*<sup>18</sup> of an equilibrium system is

$$PV = Nk_B T + \langle \mathcal{W} \rangle \quad (2.4)$$

where  $k_B$  is the Boltzmann constant,  $\langle \dots \rangle$  denotes the time average, and  $\mathcal{W}$  is the internal pressure caused by the interaction of particles [69, 172]. Similar relation is observed in [173] for a group of midges, which can be used to calculate the pressure  $P$  exerted on the animals by the external field. In addition, a small perturbation filed acted on the equilibrium system will

<sup>17</sup> The numerical simulation could generate misleading results, mainly due to the finite system size. For instance, a discontinuous phase transition in the thermodynamic limit ( $N \rightarrow \infty$ ) might appear continuous in a small system ( $N \sim 10^4$ ) [35, 167, 168].

<sup>18</sup> Notice the law for the ideal gas is  $PV = Nk_B T$ .

cause a *linear* response. This linear relationship is observed experimentally in [174]. Further more, Sinhuber and Ouellette were able to observe a constant chemical potential difference between dilute clusters and dense clusters in a swarm of midges, suggesting the existence of phase equilibrium<sup>19</sup>. Remarkably, their experimental results also suggest that detailed balance is maintained, for midges that switch between the two phases [175]. That is to say, the probability that one midge goes from a dilute region to a dense region, is equal to its counterpart for the reverse process. The detailed balance suggested an equilibrated behaviour of animals at large scale, even though the animal individuals are active and out of equilibrium. This “regained equilibrium” at large scales had also been reported from computer simulation [177].

Following this path, Sinhuber et al. presented a equation of state for midges, written as

$$PV^{1.7} = cNT^2 \quad (2.5)$$

where  $c$  is a constant, while  $P$  represents an effective pressure,  $V$  represents the volume of the convex hull constructed from the animal coordinates, and  $T$  represents the effective temperature that links to the second moment of the speed distribution. Even though this equation contains quantities with heuristic definitions (the  $P, V, T$  have special definitions), and fitting parameters obtained from experiments (the value of  $c$ , and some exponents), it predicted the changing macroscopic states of midges under different perturbations successfully [178].

Even though the thermodynamic approach is capable of predicting the macroscopic behaviour the the animals, it is less used compared to other approaches, perhaps for the lack of consensus on the definition of the suitable thermodynamic state variables. However, it is valuable also from a data science perspective, as a guide for us to project high dimensional data (the phase space) to a low dimensional feature space (the space spanned by few thermodynamic state variables). Such dimensional reduction analysis was also carried out manually [1], or with machine learning methods[179], without the thermodynamic inspiration.

## 2.5 Is Active Matter an *Useful* Concept?

Physicists mention animals as typical active matter in the literatures [35, 51, 79, 168, 180], but the biology community rarely acknowledges this perspective [171], except for some ecology literatures [179, 181]. The lack of mutual engagement is understandable, as it is difficult to apply the knowledge of active matter physics to biological topics. For instance, how does the activity affect the fitness of the animal group in a given environment? Would sick animals be less active in the wild? My fish is swimming strangely, does activity help to explain the data? To the best of my knowledge, the answers still remain elusive.

However, there are successful examples that bridge this gap between statistical physics and biology. For instance, the observation and analysis on the European starlings revealed two unexpected features, the topological interaction [120], and the scale-free correlation [67]. These two findings

<sup>19</sup> It is important to point out that the chemical potential in [175] took a special definition from [176], which depends on the pressure. Again, the pressure in [175] took another special definition, with underlying assumption that the midges were active particles without interaction, and were bounded together by an harmonic potential. Even though the definition of state variables are not very rigorous, their results are still surprising, which should not be discredited.

are biological facts, even though their connection to the physiology is still missing [171].

In chapter 7 we will present another attempt, to reduce the gap between the biology and physics. Operationally, we studied the behaviour of the mutant fish, whose genetic modification is related to human diseases. Using the correlation function introduced in section 2.3.4, we discovered the mutant fish are, surprisingly, more active. We characterised the collective behaviour of the mutant fish with the order parameter introduced in section 2.3.1. We then explained the behaviour of mutant fish with a microscopic active matter model, introduced in section 2.4. We hope this is an example that the active matter physics can be *useful*.

## Summary of Chapter 2

- We gave a brief introduction on active matter, featuring the following concepts.

### Active Matter

A out-of-equilibrium system, containing active particles which constantly inject energy to the system.

### Activity

The ratio of deterministic, self-propelling movement and the stochastic movement because of thermal fluctuation. We can increase the activity, by increasing the self-propelling speed, or by reducing the level of randomness.

### Phase Behaviour

Active particles could exhibit different phase behaviours under different conditions, for instance the MIPS and the order-disorder transition.

- We reviewed recent progress and challenges in the observation of collective motion of animals. Tracking the 2D movement of animals is an easy task, but the 3D tracking of a large group of animals for a long period of time is still challenging.
- We introduced following tools to analyse the collective motion for a group of animals.

### Order Parameters

We can use order parameters to summarise the symmetry of the collective motion of animals. Animals could be in different macroscopic states, and these states might belong to different phases, characterised by different order parameters.

### Correlation Functions

The different states can be characterised by correlation functions.

- We discussed three ways to model the animal behaviour, in order to get more insights and to create predictive theory.

### Microscopic Approach

Model the behavioural rules for each individual, and predict the animal behaviour with computer simulation.

### Hydrodynamic Approach

Model the coupled evolution of the density field, velocity field, and other fields for order parameters. Then predict the animal behaviour by analysing the solutions.

### Thermodynamic Approach

Describe the macroscopic state of the animals with thermodynamic state variables, and predict the animal behaviour with the equation of state, which constrains the thermodynamic state variables.

- The linkage between active matter physics and biology is discussed.

# Chapter 3

## Observing Zebrafish in 2D

In this chapter we will focus on the methodology to observe zebrafish, swimming in a quasi two dimensional environment. The system was chosen for technical conveniences, as the 2D movement of fish can be captured by a digital camera easily. In comparison, recording the 3D movement of fish is a harder task, which will be discussed in chapter 4.

### 3.1 Introduction

The majority of the studies on the collective behaviour of fish were performed in a quasi-2D environment, where the fish were confined in a shallow water tank [76, 182–184]. The collective motion of the fish can be captured by digital cameras and process by image processing algorithms, generating the trajectories for all fish individuals.

The crucial step in this tracking process, is to correctly locate the fish, and identify their identities. A considerable amount of softwares have been designed to tackle the problem. For instance, Pérez-Escudero et al. published an algorithm that is capable of determining the identity of the fish from its image, and using the information to obtain correct trajectories [92]. The key observation from Pérez-Escudero et al., is that the joint probability distribution of pixel distance and pixel intensity of a fish is unique. Five years later in 2019, the same group published an update method, that utilised an artificial neural network to identify the individual fish [94]. Unlike most machine learning solutions to computer vision problems, the algorithm from Romero-Ferrero et al. requires no human label, thanks to a very carefully constructed preprocess pipeline, which makes it stands out as the state of art method in the year of 2022 [95].

In addition to the ideas and algorithms, the realistic development and deploy of an animal tracking software requires a lot of engineering work. For instance, it is important to have a suitable programming language to maximise the performance of the algorithm. An accessible graphical user interface ([GUI](#)) and application programming interface ([API](#)) are also crucial. In addition, the software should be easy to install on a new machine. Practically, large research groups will develop a versatile research software, like those from Walter and Couzin [95].

In this chapter, We will present a new 2D tracking method, whose results are suitable for the calculation of 3D locations of the fish. The key

feature of our algorithm is the ability to locate fish without relying on their morphological details (see Fig. 3.1 for examples). Our new method is necessary, because the fish can swim closer or further to the camera in the 3D experiment, casting different shapes on the camera. Therefore, the identity of the fish can not be uniquely determined from their shapes in the image, causing the identity-based approach ([92, 94, 95]) to have reduced validity. The problem is termed *no-detail tracking*, as the details (the size, darkness, and shape) of a fish in the image is not a reliable source for its identification.

In the methods section, the ideas needed to carry out no-detail tracking will be discussed. The result of 2D swimming experiment, analysed by our method, will be presented in the results section. The 2D coordinates of zebrafish revealed two essential features. Firstly the spatial distribution of the fish was inhomogeneous. The effective pairwise interaction of the fish seemed attractive, and the attraction appear to decrease with the number of individuals in a group.

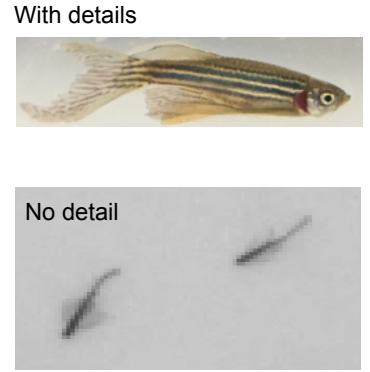


Figure 3.1: Top: a picture of zebrafish with various details. Bottom: a picture of two zebrafish with no detail.

## 3.2 Methods

### 3.2.1 Fish and Appratus

The adult zebrafish, whose age is over one year old, were used to carry out the experiment. Most experiments in this section was carried out in the fish facility in Bristol, while some experiments were performed in room G59 in the HH Physics Laboratory in Bristol. The fish were fed three times a day, with natural day to night circles. The fish were hosted in their living tank before the experiments, with a density of 5 fish per litre of water. The water was filtered constantly, with a pH value close to 7 and the temperature close or above 25 °C.

Before each experiment, the fish were transferred from their living tank to the experimental environment, which will be referred to as the observation tank. During the transfer, the fish were placed inside a temporary container, and then released into the observation tank. To make the fish stay in a quasi-2D environment, a flat plate was placed in a bowl-shaped tank, creating a shallow water environment (Fig. 3.2). The shape of the bowl is especially chosen for a 3D tracking task, which will be introduced in chapter 4.

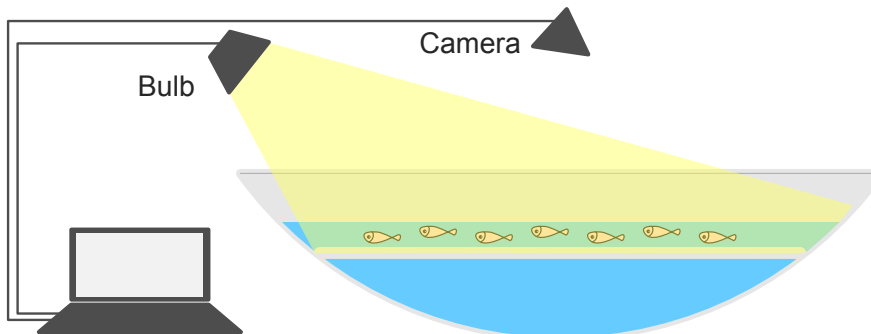


Figure 3.2: The appratus to track the movement fish in a quasi-2D environment. The camera is placed above the fish to capture the top view. A computer controls the recording process as well as the illumination.

### 3.2.2 Metric Rectification

To record the video of the fish, a camera (Basler AC2040um) was fixed on top of the tank, as illustrated in Fig. 3.2. The image size produced by our camera is 2056 pixels  $\times$  1540 pixels, at a frequency of 15 frames per second. We mounted a 6 mm fixed focal length lens (C Series, Edmund Optics) on the camera, which yields a wide view, allowing us to place the camera closer to the fish group. The typical distance between the camera and the fish group is around 2 meters. With such setup, the fish (body length  $\sim$  30 mm) appear as black rods in the videos, as shown in Fig. 3.3.

The image and videos obtained from the camera have three limitations, preventing it from being an accurate measurement tool. The first issue is the distortion of images caused by the camera lens. In addition, the cameras should be orientated exactly perpendicular to the water surface, so that the captured images were from the top view. Such accurate orientation is difficult to achieve without especially designed camera holders. Finally, we also need to convert the unit of the image (pixels) to real life units (e.g. meters). It is worth mentioning that these issues were more or less ignored in conventional 2D animal tracking tasks [96], and the present method is novel in the context of animal tracking.<sup>20</sup>

To solve the problems, we need to *calibrate* the camera, so that we know the distortion of the camera lens, the orientation of the camera, as well as the scale of objects in the images. To carry out the calibration, a chessboard (the calibration board) was placed on the surface of the water. And the image of the calibration board will offer enough information to tackle the aforementioned issues.

The distortion can be recovered with standard camera calibration methods<sup>21</sup> from the computer vision community [102, 185]. The distortion is described with the following model,

$$\begin{aligned}x_{\text{distorted}} &= x(1 + k_1r^2 + k_2r^4 + k_3r^6) \\y_{\text{distorted}} &= y(1 + k_1r^2 + k_2r^4 + k_3r^6)\end{aligned}$$

where  $r$  is the radius of the pixels in the image with respect to the optical centre. And  $k_i$  values are the distortion coefficients, which will be used to recover the undistorted image.

The imperfect orientation can be fixed by the knowledge of the camera as well. Briefly, the same 2D plane in the 3D space, will form different projections with different cameras. These different 2D projections are related to each other by a projective transformation. Likewise, the same 2D plane for the fish in the imperfectly orientated camera is also related to its counterpart from a perfectly orientated camera. Such a relation is termed as *homography*, and can be represented by a matrix  $\mathbf{H} \in \mathbb{R}^{3 \times 3}$ . This matrix can be calculated easily with the knowledge of the camera, following the method from Hartley and Zisserman [102]. The homography allows us to transform the image from the imperfectly orientated camera, to a virtual image captured from a perfectly orientated camera. The transformed image is called the *rectified image*. From the rectified image, the scale can be recovered easily as we know the physical size of the calibration board. We call the rectified image with a known scale the *metrically rectified image*.

<sup>20</sup> Addressing these issues is “less novel” in the computer vision community focusing on the 3D reconstruction. It is impossible to retrieve 3D information correctly without understanding all the details about computers and photos.

<sup>21</sup> The functions from the “opencv” library were used for the calibrations.

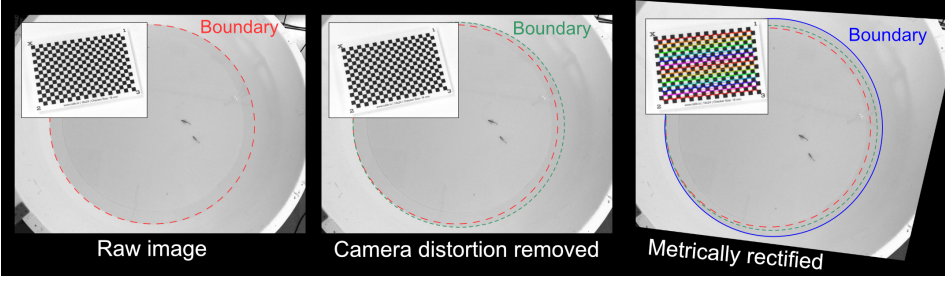


**Figure 3.3:** The process of metrical rectification. Left: the original image. Middle: the image where camera distortion being removed. Right: the metrically rectified image. The circular outline of the 2D boundary were outlined and overlaid, to stress the change of the image in different steps. The inserts in the figures correspond to the calibration pattern in each process.

Figure 3.3 shows an example of the metric rectification. Comparing the outline of boundary with/without distortion removed, it is clear that the raw image from the camera were distorted by the lens. The camera in the experiment were not perfectly perpendicular to the water surface, therefore the outline of the tank boundary appears to be an ellipse, because of the perspective transformation ( $\mathbf{H}$ ). The ellipse were reverted back to a circle (right subfigure, Fig. 3.3) after the rectification process.

Notably, the image rectification only “works” for the plane, where the calibration chessboard lies. For the fish data, the rectification is only accurate for the fish exactly swimming on the water-air interface. In other works, there will be tiny errors for the fish locations, when they swim inside the water. Such inaccuracy is fundamental for 2D fish tracking, since the fish is swimming a 3D space. To eliminate such error, we can carry out real 3D measurements, which will be introduced in chapter 4.

### 3.2.3 Image Processing

The metrically rectified images of the fish contain the information about their behaviour. To get useful information out of the image, we still need to perform image processing, to extract the coordinates of the fish from the images.

In a normal image, the fish appear as a dark spot (see Fig. 3.3 and Fig. 3.4 for instances). Ideally, we want to work with images containing a collection of delta functions (see middle subplot of Fig. 3.8 for instance), where the pixel intensities in the centres of each individual fish is maximised, and the pixel intensities are zero everywhere else. Extracting the coordinates of fish from such image, will therefore be a trivial task, as we only need to find the pixels with non-zero values. Even though it is possible to construct such transformation directly with machine learning based approaches [186], it is still not an easy task, without large amount of human labelled training data. Therefore, we restrict our goal for the image processing process to be the removal of the static background. As a result, the processed image should only contain the fish.

Traditional image processing methods, such as thresholding, blurring, and morphological operations, were used in this project to perform the background removal task. As a result, we get a *foreground video* where each fish has high pixel intensity values, and the background intensity values are zero. Figure 3.4 illustrates the result of the transformation. One frame of the recorded video was shown in the left subfigure, while the same frame from the foreground video was shown in the right subfigure.

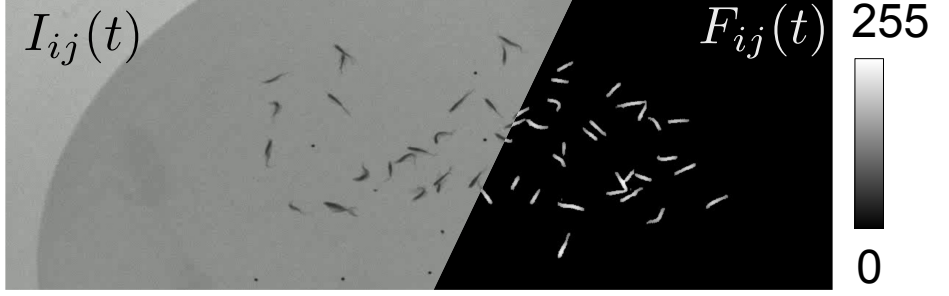


**Figure 3.4:** The screenshot of the video at time point  $t$ , and its corresponding foreground image.

<sup>22</sup> The brightness of the environment might change in the field observation, where the sunlight might be temporally covered by the cloud. In the laboratory, the sunlight will also change the overall brightness indoors.

The foreground videos of the fish are obtained after two steps, the removal of the background and the removal of the noises. The background is defined as the temporal average of the image, since the fish are constantly moving while rest of the scene is static. In order to tackle the varying illumination conditions<sup>22</sup>, we can take a running average of a time–window, instead of calculating the overall average. The pixel intensity of the background ( $B_{ij}(t)$ ) at time  $t$ , of pixel  $(i, j)$ , can be written as

$$B_{ij}(t) = \frac{1}{T_w} \sum_{\tau=t}^{t+T} I_{ij}(\tau) \quad (3.1)$$

where  $I_{ij}(t)$  is the pixel intensity of the video at time  $t$  in position  $(i, j)$ , and  $T_w$  is the duration of the window, usually taken as 40 seconds. The difference between the background video and original video yields a foreground video ( $F_{ij}(t)$ ), written as

$$F_{ij}(t) = B_{ij}(t) - I_{ij} \quad (3.2)$$

and the order of the subtraction ensures the fish, originally appear darker in the video, to be represented by brighter pixels in the foreground video. The subtraction result can be very noisy. To remove the noise, the gaussian filter was applied to the foreground image. Then, the combination of the Ōtsu threshold and local Gaussian threshold was applied to the image, to separate the pixels belonging to the fish and other pixels. The Ōtsu threshold is a single value that split the image into two groups, where the inter-group variance was minimised. The local Gaussian threshold, on the other hand, gives a collection of different values for different pixels, featuring the locally bright pixels as foreground. Finally, the morphological operation “binary opening” was applied to the image, to remove any possible remaining noise. The results shown in Fig. 3.4 was obtained with this method.

Our method requires 3 parameters, including the standard deviation ( $\sigma_{\text{blur}}$ ) of the Gaussian kernel of the blurring process, the length scale for the local threshold ( $l_{\text{local}}$ ), and the length scale of the binary open operation ( $l_{\text{open}}$ ). In the different experiments, the images were similar, therefore the same set of parameters ( $\sigma_{\text{blur}} = 2, l_{\text{local}} = 3, l_{\text{open}} = 3$ ) was applied, and works well for most videos.

### 3.2.4 Extracting Features from the Image

<sup>23</sup> We explained the term “features” by the end of the section.

From the processed video, we need to extract the features<sup>23</sup> in each frame that correspond to the fish. In order to tackle the problem, we employed

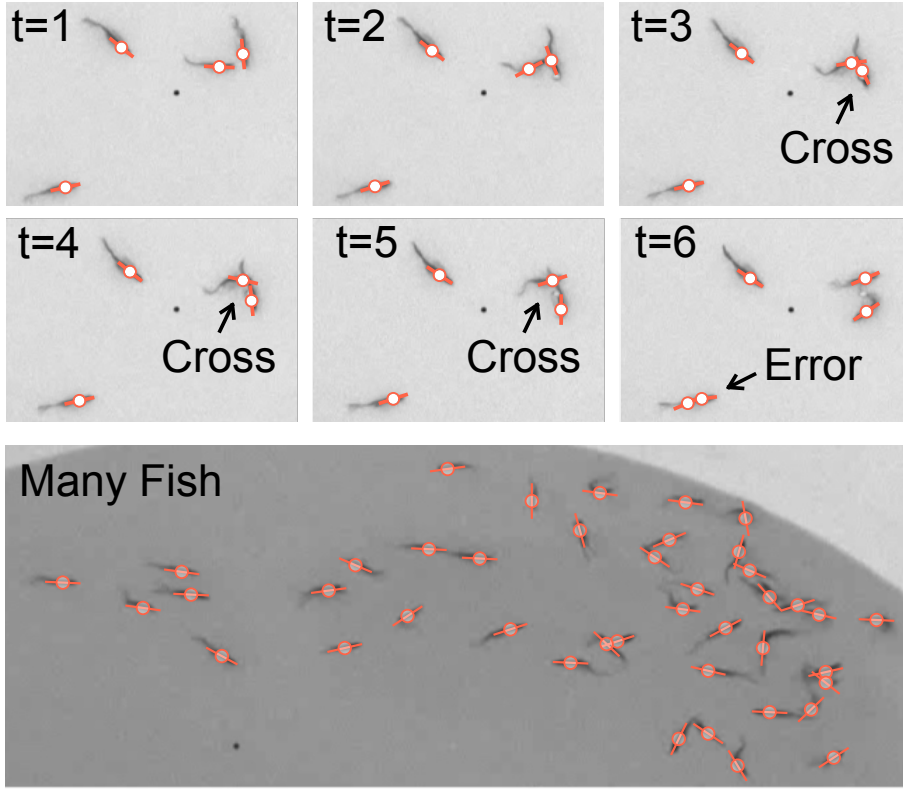


**Figure 3.5:** The locations and orientations,  $\{(i_m, j_m, o_m)\}$ , of different fish. The locations are rendered as circles, while the orientations were rendered as short line segments. The features were calculated from the feature tensor ( $C_{ijo}$ ). Top: the movement of 4 fish in 6 successive frames labelled with the detected features. An error where one fish was mistakenly labelled as two fish happened in the 6th frame. Bottom: the movement of many fish labelled with the detected features.

a method that not only captured the positions, but also the information of the fish orientations and body shapes. The basic idea is to calculate the cross-correlation between the image ( $F_{ij}$ ) and a templated fish shape ( $T_{ij}$ ), as the local maxima in the result would indicate the presence of a fish, because cross-correlation is a measure of similarity between signals.

For a fixed 2D fish template ( $T_{ij}$ ), we can rotate it so that it contains  $o$  different orientations. Calculating the cross-correlation of all the rotated templates, we can effectively get  $o$  different results, and they can be concatenated into a 3D tensor, written as  $C_{ijo}$ . One can think of the tensor  $C_{ijo}$  as a 3D volumetric image. A local maximum in  $C_{ijo}$ , with coordinate  $(i_m, j_m, o_m)$ , indicates the presence of a fish at location  $(i_m, j_m)$ , with orientation  $o_m$ .

In addition, we are free to choose different templates for the fish shape, to capture the different postures. The choice for the template will be discussed in section 3.2.5. If  $s$  different shapes were selected as templates, all of which were rotated into  $o$  different orientations, then there will be  $s \times o$  different templates. The cross-correlation of these templates with the image would yield a 4D tensor that can be shaped into  $C_{ijos}$ , noted as the *feature tensor*. A local maximum of the feature tensor, with coordinate  $(i_m, j_m, o_m, s_m)$ , represents a fish located at  $(i_m, j_m)$ , whose shape is like the  $s_m$ th template, with orientation  $o_m$ . All the local maxima,  $\{(i_m^i, j_m^i, o_m^i, s_m^i)\}$ , captured the locations, orientations and shapes of all the fish in the image.

In summary, the cross-correlation between the image and the many templates yields a 4D feature tensor, whose local maxima give us the locations, orientations, and shapes of different fish. This approach is especially help-

ful for the dense system, where the fish constantly overlap with each other. In such dense scenario, the overlapping fish will be separated into different regions in the shape–rotation dimension in the feature tensor. For example, the overlapped fish pair in Fig. 3.5 was correctly labelled, by calculating the local maxima in the 4D tensor.

There is a fundamental flaw of our algorithm, where a big fish might be mistakenly labelled as two small fish. One example of such error was presented in Fig 3.5 (top row, t=6). This is partially due to the loss of morphological details of the fish, as the cameras were placed relatively far from the fish, in order to capture larger groups. Without the details, it can also be hard for a human being to tell, whether a dark blob is a big fish or it belongs to two smaller fish. Realistically, some of the errors produced by our algorithm can be easily distinguished by human beings. Some post processing methods of the features, based on the geometry of the fish, might be useful to further refine our algorithm. The ultimate goal is to make the feature detection algorithm being compatible with human observations.

#### Why are features called features, not positions?

In the computer vision community, people call the locations of objects “features”. This term is rooted in the 3D reconstruction problem, which will be discussed in the chapter 4. Briefly, the 3D information can not be recovered from the background, like a purely white wall. Instead, some “features” with intensity gradients are required [185]. Alternative names would be “positions” or “locations”. However, we are interested in a “feature” of the photo, rather than a (physical) location of a fish.

### 3.2.5 Finding Templates for the Features

To calculate the feature tensor  $C_{ijos}$ , it is important to use suitable templates for the fish. The templates should represent characteristic fish shapes. The following operations were carried out to find suitable templates.

1. Segment the individual fish and align the segmented images.
2. Project all the segmented images to a space with reduced dimension.
3. Find clusters for the data points in the reduced space, and the average of each cluster to be the template.

The individual fish, defined as connected bright pixels, were segmented from the foreground video ( $F_{ij}(t)$ ). The orientation of the segmented fish were determined by the principle component analysis (PCA) [187]. These segmentations were then reoriented, so that its first principle axis align with the  $x$  axis. The reoriented individual fish were then zero-padded to have the same shape, noted as  $\mathbf{S} \in \mathbb{R}^{s \times s}$  where  $s$  is the size of the padded images. Examples of the segmented and aligned images are illustrated in Fig. 3.6. These images were collected over 1000 different frames, in a video of 4 swimming fish. A total of 3070 individual shapes were collected.



**Figure 3.6:** Top: the selected individual fish segmented from the images taken by the camera. Bottom: the fish shapes reconstructed from a low dimensional feature space  $\mathbf{X}_{\text{red}}$ .

The collection of segmented fish is a very large dataset. For example, if we use a small image of size  $50 \times 50$  pixels, to stored each fish, then each fish corresponds to a point in a 2500 dimensional space. The dimension of such images can be drastically reduced by PCA [188, 189]. Operationally, all of the  $m$  images of individual fish were flattened ( $\mathbb{R}^{s \times s} \rightarrow \mathbb{R}^{s^2}$ ), and concatenated into a matrix ( $\mathbf{X} \in \mathbb{R}^{m \times s^2}$ ). The singular value decomposition (SVD) is then performed on the dataset  $\mathbf{X}$ , following

$$\mathbf{X} = \mathbf{U}\Sigma\mathbf{V}^T,$$

where the matrices  $\mathbf{U}$  and  $\mathbf{V}$  contains all the left and right singular vectors, and the matrix  $\Sigma$  contains all the singular values. The images ( $\mathbf{X}$ ) were then project on the first  $k$  axes ordered by their corresponding singular values. Effectively, the dimension of the matrix  $\mathbf{X}$  were reduced from  $m \times s^2$  to  $m \times k$ , forming a new matrix  $\mathbf{X}_{\text{red}} \in \mathbb{R}^{m \times k}$ . Each row in  $\mathbf{X}_{\text{red}}$  described one fish.

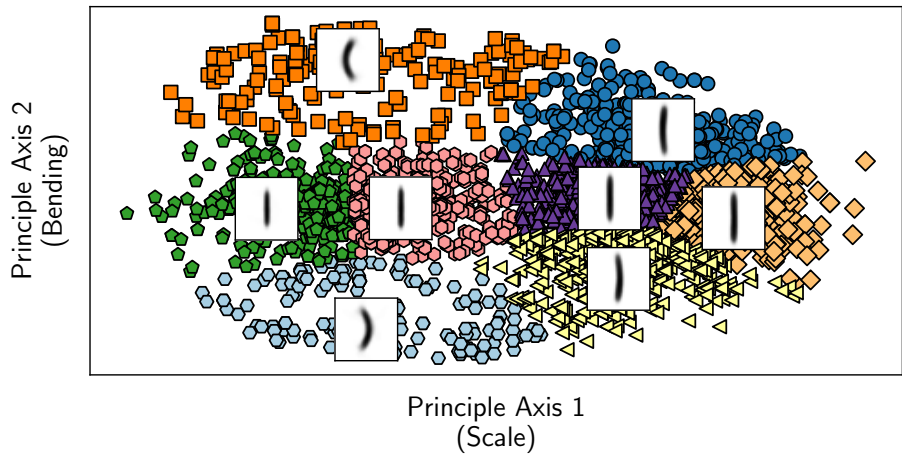
Figure 3.7 shows the average fish shape as well as the projection of all the segmented fish ( $\mathbf{X}$ ) on the first two principle axes. The first principle axis (the  $x$  axis of Fig. 3.7) roughly captured the scale of the fish, and the second principle axis (the  $y$  axis of Fig. 3.7) captures the information about the bending of the fish. The overall distribution of those projected data can be understood by the fact that the same fish can have different distances and orientations, relative to the camera, so that their shapes will appear different. The distribution of Fig. 3.7 is symmetric in the  $y$  direction, which indicates the absence of chirality for the bending of fish. That is to say, the fish do not prefer bending to the left, or the right.

With all the segmented fish being projected to low dimensional space, we can use the *k-means cluster* algorithm to find representative cliques of the fish shapes. Briefly, different data points (different fish images in Fig. 3.6) will be assigned to different clusters. And the variance of points in the same cluster will be minimised, while the variance of points from different clusters will be maximised.

Each cluster corresponds to similar fish images with similar shapes. The average shape of different clusters were used as the template. The different scatters in Fig. 3.7 shows the different clusters, and their corresponding average shapers were inserted. Here, the images ( $\mathbf{X}$ ) were projected to a 2 dimensional space ( $k = 2, \mathbf{X}_{\text{red}} \in \mathbb{R}^{3070 \times 2}$ ). And the overall 3070 points were separated into 7 different clusters. And the average shape of different clusters (the inserted subplots in Fig. 3.7) can be used as the templates to calculate the 4D tensor for tracking.

The number of clusters and the dimension of the reduced space ( $k$ ) are

**Figure 3.7:** A collection of 2170 different fish shapes, projected onto the first two principle component axes. The data points were clustered using the K-means algorithm, into six different clusters, indicated by different marker styles. The average shape of each cluster were plotted in the inserted axes.



<sup>24</sup> If the 2D features are not good, the corresponding 3D reconstruction (chapter 4) will fail.

free parameters, whose optimal values were hard to determine. Practically, I always set  $k = 5$ , and separate the points into 8 different clusters, which yields good<sup>24</sup> results for 2D tracking. The dimensional reduction method (PCA) and the clustering algorithm (K-means) can be changed to other tools with similar effects. For instance, it is possible to use non-linear dimensional reduction method such as isomap, and a gaussian mixture model to obtain different clusters.

The mapping from the image to the large 4D tensor,  $I_{ij} \rightarrow C_{ijos}$  requires a large amount of calculation. The feature tensor is normally sparse, since only a few pixels in the image contain the centre of the fish. The calculation can be faster if such sparsity were to be exploited. Practically, we can only calculate “promising” pixels, where fish is likely to appear. These pixels correspond to the local intensity maxima in the foreground image  $F_{ij}$ . Such reduction of calculation improved the calculation speed significantly.

### 3.2.6 Convolutional Neural Network

There are two steps in the image processing that can be improved in the image processing pipeline. The first one is the removal of background. In my current method, I calculated a rolling average of the entire video. The window size of the averaging operation is set by the user, which is very difficult to optimise because the video processing typically takes hours to finish. Practically, a rule-of-thumb number (600 frames) was applied. However, the fish in the video are very distinct from their background, and it is an easy task for people to spot the fish in a static image. This suggests a static image contains enough information to distinguish the foreground (fish) and background (tank).

The convolutional neural network (**CNN**) is very suitable for carrying out both tasks at the same time, with far better efficiency. The overall data process introduced from section 3.2.3 to section 3.2.5, is essentially a transformation from the image ( $I_{ij}$ ) to a tensor ( $C_{ijos}$ ). In addition, the information about the kernel is unnecessary<sup>25</sup> in most cases, as we often only care about the orientation and location of the fish, rather than its shape. Hence, we need a model with the capacity to carryout the following

<sup>25</sup> The shapes might be informative for people studying the postures of the swimming fish. But we will ignore the shapes in this thesis as we are interested in the *collective motion* of the fish.

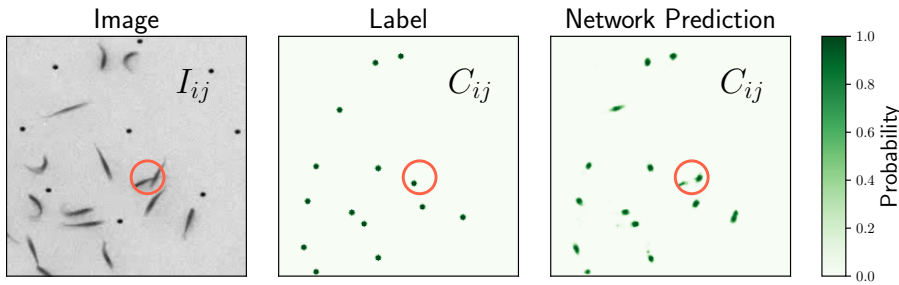


**Figure 3.8:** The tracking result of a convolutional neural network (CNN). Left: the image ( $I_{ij}$ ) from which the fish will be detected. (The black dots in the image are the holes drilled on the tank.) Middle: the feature tensor ( $C_{ij}$ ) for all the pixels generated by a conventional 2D tracking algorithm. This data is used as training data for the neural network. The value of a pixel in the tensor represents the probability that a fish centre being located inside this pixel. Right: the feature tensor ( $C_{ij}$ ) for all the pixels predicted by the CNN model. The network prediction should be close to the label after the network being trained.

transformations depending on our desired results:

$$I_{ij} \rightarrow C_{ijos} \quad \text{location, orientation, and shape}$$

$$I_{ij} \rightarrow C_{ijo} (= \max_s C_{ijos}) \quad \text{location, and orientation}$$

$$I_{ij} \rightarrow C_{ij} (= \max_o C_{ijo}) \quad \text{location}$$

And we can generate a big dataset containing images ( $I_{ij}$ ) and their corresponding feature tensors ( $C_{ijos}$ ), and make a CNN to learn the underlying rules for the transformation ( $I_{ij} \rightarrow C_{ijos}$ ). If we need less information from the result, the targeted  $C$  can be contracted, by taking the maximum value along the dimension of the unnecessary information.

As a proof of concept, a CNN model was built to carry out the transformation of  $I_{ij} \rightarrow C_{ij}$ . The training data for the network was generated from the existing tracking result  $C_{ijos}$ . The model was built with popular framework tensorflow [190], and trained on the Colab online platform provided by Google [191]. Figure 3.8 shows the output of a trained network. The network does not generate the exact same picture of the label, but their results were similar. Notably, the network even fixed an error of the original feature detection algorithm. This error is highlighted in Fig. 3.8.

However, due to the limited time for this project, the final CNN model did not improve the calculation accuracy nor the processing speed significantly. Nevertheless, it is achievable to having the calculations to be optimised that the tracking can be performed in real time, since the prediction of  $C_{ij}$  on a GPU is very fast, reaching a speed of  $\sim 50$  frames per second. The current speed-limiting step is the calculation of local maxima in  $C_{ij}$  with CPU. This calculation can be accelerated by either exploiting the sparsity of  $C_{ij}$ , where local maxima detection can be converted to an overlapping removing problem (see section 5.2.1). Alternatively, it might also be helpful to carry out the calculation on GPU.

### 3.3 Results

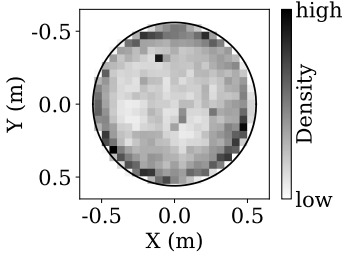


**Figure 3.9:** The spatial distribution of one adult zebrafish in a quasi 2D environment, present the joint distribution of the  $x$  coordinates and  $y$  coordinates of the fish positions, with the shape of the boundary being highlighted.

#### 3.3.1 A Single Fish

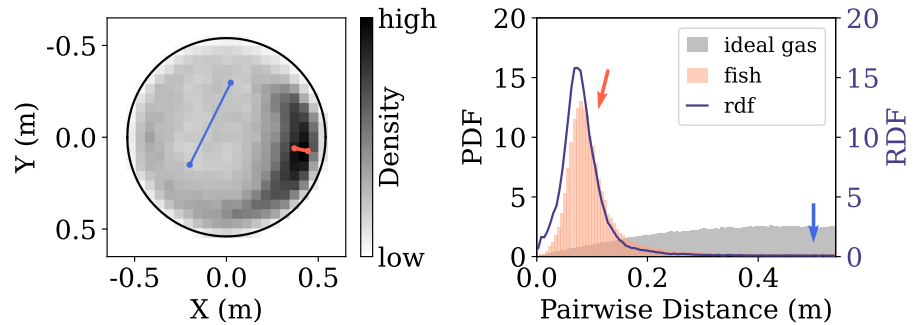
Figure 3.9 shows the spatial distribution of one adult wildtype zebrafish. We can see from the figure that the fish have a slightly higher tendency to stay near the boundary. The apparent attraction between the fish and the boundary can have two reasons. Firstly, the fish may biologically prefer to be near the boundary. The systematic preference for the wall of the tank was documented for zebrafish previously [192].

In addition, the preference to the wall of the fish could emerge as a physical consequence, if we think of fish as self-propelling particles [31, 193, 194], as justified in section 2.1. To understand this physical origin, it is helpful to imagine a fish who changes its orientation randomly. Without the boundary, the fish would move constantly, regardless of its orientation. On the other hand, if the fish were swimming against the wall, they have to wait until the orientation changes, to leave the wall and continue swimming. The extra waiting period near the wall would contribute to the spatial distribution.

#### 3.3.2 Two Fish

The movement of 2 adult zebrafish was recorded. The data was taken over 5 experiments, and each experiment lasted one hour. The spatial distribution of 2 fish were shown in Fig. 3.10 (left). It is clear that the fish were not uniformly distributed in the tank, which might also related to the environmental factors, such as the illumination level [21, 97, 195]. Practically, we also found the zebrafish would respond to the shadows casted by the objects around the tank.

**Figure 3.10:** The spatial distribution of two adult zebrafish in a quasi 2D environment. Left: the joint distribution of the  $X$  coordinates and  $Y$  coordinates of the fish positions, with the shape of the boundary being highlighted. Right: the probability density function (PDF) for the distance between two fish. The PDF for the distance of 2 ideal gas particles, uniformly distributed in the tank, were also plotted. The ratio of the two PDFs were taken as the radial distribution function (RDF).



The pairwise distance of the 2 fish offered us the way the characterise their cohesion. If the fish were attracted to each other, they would stay

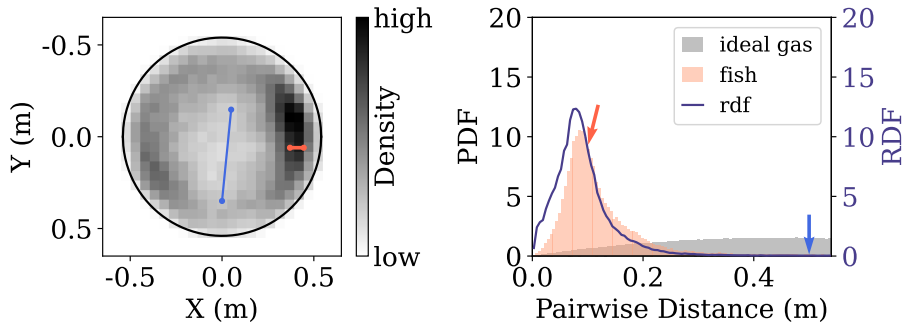


**Figure 3.11:** The spatial distribution of three adult zebrafish in a quasi 2D environment. Left: the joint distribution of the  $X$  coordinates and  $Y$  coordinates of the fish positions, with the shape of the boundary being highlighted. Right: the probability density function (PDF) for the distance between two fish. The PDF for the distance of 3 ideal gas, uniformly distributed in the tank, were also plotted. The ratio of the two PDFs were taken as the radial distribution function (RDF).

close, and vice versa. The distribution of the pairwise distances, shown as the probability density function (PDF), were plotted in the Fig. 3.10 (right). There is a peak in the distribution, and it seems to be dominated by the inhomogeneous distribution of the fish, as the length scale corresponding to the peak matches the size of the high density blob. Such a length scale was highlighted in Fig. 3.10 (left).

It is useful to compare the distribution of the pairwise distance of the fish, with the distribution from the ideal gas. Here ideal gas means random points uniformly distributed in the circular tank outlined in Fig. 3.10. The distribution of the ideal gas were presented in Fig. 3.10 (right). The probability of finding particles at large distances, like 0.5 meter, is higher for the ideal gas particles comparing with fish. This is also likely due to the inhomogeneous distribution of the fish, as such length scale corresponds to a big “void” in Fig. 3.10.

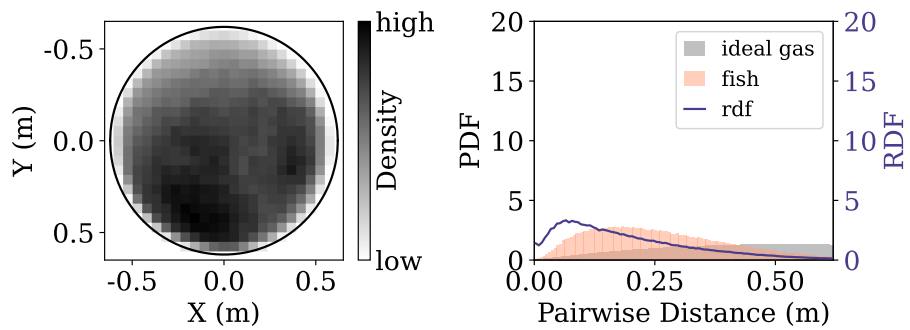
Inspired by liquid state theory, we define the ratio between the PDF of the fish and that of the ideal gas as the radial distribution function (RDF), which is also known as the  $g(r)$ , as introduced in section 2.3. For a dilute fluid at equilibrium, the shape of its RDF can be used to calculate the pairwise interaction potential. The mapping between pairwise potential and the  $g(r)$  is invalid for the fish, because the individuals were constantly spending their biological energy to swim, driving the system out of equilibrium. Nevertheless,  $g(r)$  is still a useful tool to characterise the cohesiveness of the fish group. The RDF of 2 fish are plotted in Fig. 3.10, and it presents a peak at very short separation. The hight of the peak ( $\sim 15$ ) offered a measure of the attraction amongst the fish, and more detailed analysis will be provided in chapter 5.

### 3.3.3 Three Fish

The behaviour of 3 adult zebrafish is very similar to that from 2 fish. The density distribution and the distribution of pairwise distances of 3 zebrafish were shown in Fig. 3.11. Like the situations in the one fish and 2 fish system, the distribution is not uniform. And the fish also present a typical peak in the pairwise distance, whose location ( $0.08$  m) corresponds to the size of the high density blob of the inhomogeneous distribution.

Comparing the PDF of the pairwise distance of the fish, with that from

**Figure 3.12:** The spatial distribution of 50 adult zebrafish in a quasi 2D environment. Left: the joint distribution of the  $X$  coordinates and  $Y$  coordinates of the fish positions, with the shape of the boundary being highlighted. Right: the probability density function (PDF) for the distance between two fish. The PDF for the distance of 50 ideal gas particles, uniformly distributed in the tank, were also plotted. The ratio of the two PDFs were taken as the radial distribution function (RDF).



3 ideal gas, the fish also presents the typical void like the 2 fish scenario. The RDF for 3 fish, shown in Fig. 3.11 (right) is very similar to that of 2 fish. The height value of the peak for 3 fish is close to 12, being slightly smaller than that from 2 fish experiments. One possible explanation for such reduced attraction, is the reduced danger perceived by the fish, when they were in a large group [26]. As the fish will form a denser group when they perceived danger [196]. As well be presented later, the reduced cohesion with increased group number is a general observation.

### 3.3.4 Many Fish

The distribution of 50 fish was significantly different from the 1/2/3 fish results, as presented in Fig. 3.12. Comparing with the 1/2/3 fish experimental results, the density distribution of 50 fish were more homogeneous, shown in the left subfigure in Fig. 3.12. However, it is still not uniform. The homogenised picture for 50 fish might be related to the fact, that the fish-fish interaction dominates the behaviour for 50 fish, while fish-environment interaction dominates the behaviour of 1/2/3 fish. The same trend was also observed in a 3D swimming experiment, which will be discussed in section 4.3.4.

In addition, the PDF of the pairwise distance for 50 fish were much broader comparing with its 2 or 3 fish counterpart. Nevertheless, we still see the same trend, where the fish were cohesive in short length scales, and presented “void” at larger separation distances. Such feature is also likely due to the inhomogeneity of the density distribution. However, the difference of the PDFs for the 50 fish and 50 ideal gas particles was less significant. As a result, the RDF of the 50 fish contains only a broad peak, whose height value ( $\sim 3$ ) is significantly smaller the height value of the RDF for 2 or 3 fish. This suggested a smaller effective attraction<sup>26</sup> between the fish when they were in a large group. Our observation, the reduction of peak height in the RDF, is consistent with previous study [132].

<sup>26</sup> The “attraction” is unlikely to be biased by our choice of the measurement, the RDF. The RDF is effectively a re-weighted PDF of the pairwise distances. Other measurements of the fish-fish distances are therefore related to the RDF in different ways, which will be discussed in Chapter 5. As an example, the nearest neighbour distance is proportional to the height of the peak in the RDF (Fig. 5.9 and 5.12 in Ch. 5).

## Summary of Chapter 3

- Locating a group of fish in 2D is necessary for their 3D reconstruction. For this task, existing methods utilise the morphological details of the fish for identification. These methods are only accurate for fish swimming in a quasi-2D system.
- We proposed a new method to locate fish in 2D, where the fish are swimming in a 3D environment. Our method includes the following process.

### 0. Metric Rectification (optional)

The distortion and imperfect orientation can be removed by camera calibration.

### 1. Image Processing

The images, captured by the cameras, are separated into the foreground and the background.

### 2. Finding Templates

The individual fish in the foreground are segmented, aligned, and projected to a low dimensional space. Characteristic shapes were identified with clustering algorithm for data points in the low dimensional space.

### 3. Constructing the Feature Tensor

The templates were rotated into different orientations. For every template and orientation, its cross-correlation with the foreground is calculated. The results correspond to a 4D feature tensor.

### 4. Extracting the Features

Local maxima in the 4D feature tensor correspond to the locations, orientations, and shapes of the fish in the image. Each maximum is called a feature in the image.

- We reported the analysis on the coordinates of zebrafish in a quasi-2D environment, featuring different fish numbers.

#### One Fish

The fish tend to swim near the boundary.

#### Two Fish

The fish tend to swim near one side of the boundary. The heterogeneity of the spatial distribution dominated the radial distribution function.

#### Three Fish

The behaviour of three adult zebrafish is very similar to that from two fish.

#### Fifty Fish

The spatial distribution of 50 fish presented a more uniformed manner, with significantly reduced cohesiveness.

## Chapter 4

# Observing Zebrafish in 3D

### 4.1 Introduction

This chapter presents the method to build up a system to observe a group of zebrafish in 3D, and obtain the 3D coordinates of individuals in a group of fish. The system is inspired by the pioneering work of Cavagna et al. [131] as well as Kelley and Ouellette [116], where the 3D locations of European starlings and midges were calculated and analysed.

The 3D observation is a difficult task. Compared to the the 2D observation introduced in chapter 3, both the hardware and the software were more complicated for the 3D observation. Typically, we need to use multiple cameras to capture the movement of the fish, where the images were taken in a synchronised way. The calculation also needs more attention, since the optical details, such as the refraction of light at the water–air interface, will affect the final result.

Mathematically, it is important to understand the formation of the image on a camera, because we need to reverse this process to calculate the 3D locations. For the relevant details, we refer the readers to [102, 185]. This chapter will instead focus on the *implementation* of the ideas. The code responsible for the methods in this chapter is open source, and hosted on website “GitHub”, with a project name of [yangyushi/FishPy](#).

It is worth mentioning that the 3D observation method is also widely applied in the study of fluid mechanics [197], dating back to the 1990s. The name of the method is formally *particle tracking velocimetry*<sup>27</sup> (PTV) in the fluid mechanics literatures. Therefore, the new development from the fluid mechanics community may provide opportunity to improve the animal. For instance, by applying the field-programmable gate array (**FPGA**), the 2D feature selection can be performed in real time, which reduced the amount of processing time and data-storage space significantly [198].

In addition, the physicists and zoologists have pushed the boundary of technology for field observations. For instance, Cavagna et al. developed the system that can track the 3D movement of animals while moving the cameras with a joypad<sup>28</sup>, enabling researchers to follow the movement of birds for a long period of time [122]. Another example of advanced observation techniques is the reconstruction of a group of fish in the field, with observers swimming together with the fish, while holding two cameras [123]. By incorporation the static environmental information, the movements of

<sup>27</sup> The term “particle tracking” in the fluid mechanics community and the soft-matter community refers to slightly different things. The former focus on the dynamic (velocities) of the particles, while the latter focus more on the structure (coordinates) of the particles.

<sup>28</sup> A joypad is a controller connected to a computer, or other game consoles. In many 3D video games, the players rotate the virtual cameras in the game to explore the environment. This movement is also needed to follow animals in the field.

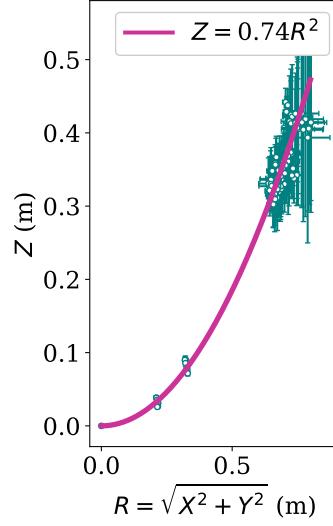
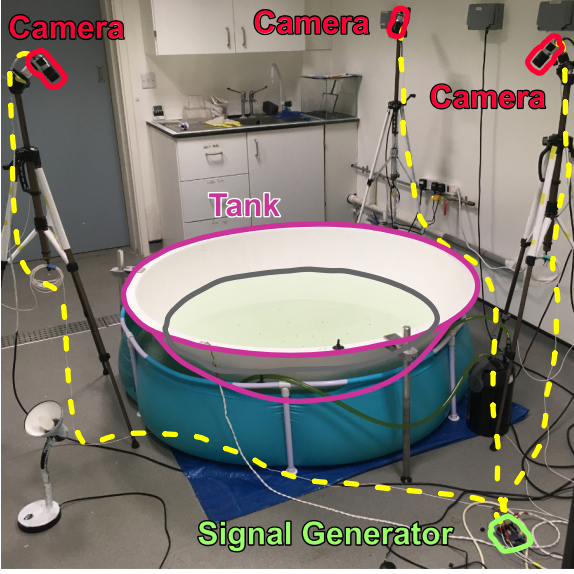


**Figure 4.1:** Left: The photo of one experimental setup. Three cameras are mounted to observe the fish in the bowl-shaped tank. Time-synchronised signals were generated by an Arduino chip to trigger the cameras for capturing synchronised videos. The bowl was immersed in a bigger tank, which is a framed swimming pool. The husbandry-related equipments, such as the water filter, the heaters, the UV lamp, were placed outside the bowl but inside the bigger tank. Right: The measured shape of the observation tank. The scatters were markers on the tank, which were fitted by function  $z = 0.74r^2$ , where the unit of both  $z$  and  $r$  is meter.

the cameras can be effectively estimated, which can be used to reconstruct the trajectories of the fish.

Using the developed 3D observation system, I studied the behaviour of one adult wildtype zebrafish, as well as groups of zebrafish with different sizes ( $N = 2, 3, 50$ ). The result section presents their spatial distribution and the distribution of their pairwise distance. The observed results revealed the important interaction between the fish and the environment. The *dynamic* of the system, which involves the time derivative of the locations, will be analysed and discussed in chapter 5.

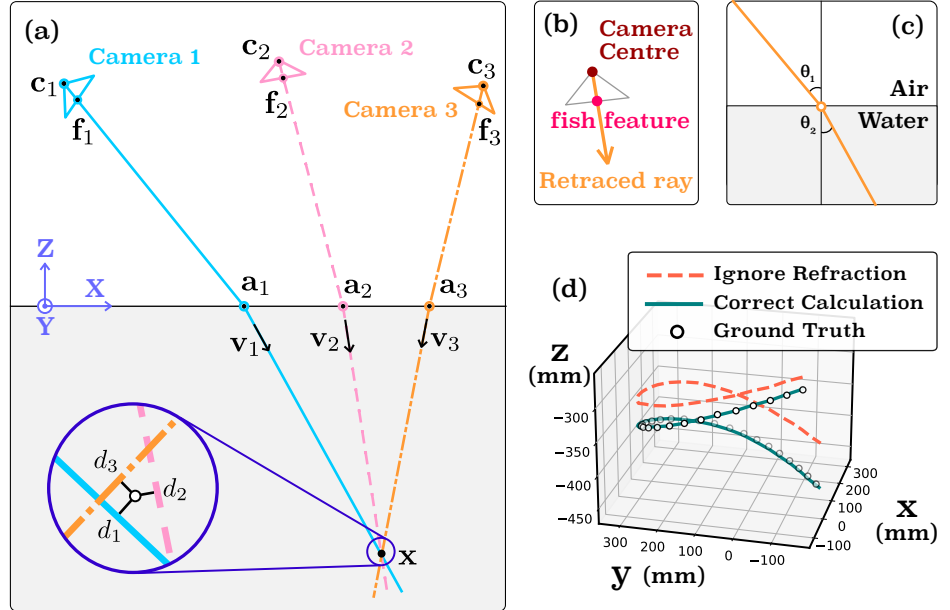
## 4.2 Methods

This section should serve as a practical tutorial for building a multiple view 3D system to track animals. This system is capable of extracting 3D location of the fish, with three commercial cameras. Our choice is not the only technology to extract 3D information about animals. Instead, there are alternative ways to follow the movement of animals such as binding animals with global positioning system (GPS) [110] and tagging the animal bodies [199]. Comparing with these solutions, our method is non-invasive and relatively cheap. However, the obtained results are affected by the errors of the 2D locating of fish individuals (section 3.2.3), and the ambiguity in the stereo matching process (section 4.3.4).

### 4.2.1 Tank Design and Hardware

Figure 4.1 shows the experimental setup in the laboratory, where I mounted 3 cameras pointing to a bowl-shaped tank. This big bowl was immersed in a framed swimming pool. Synchronised signals were generated with a Arduino chip, and the cameras are able to capture time-synchronised videos with the signals. The trigger signal for the camera is a 5V pulse, being the default HIGH output signal of an Arduino chip.

**Figure 4.2:** The illustrations for the concept for locating one fish in 3D. (a) the schematic for the calculation of the 3D fish location from three cameras. The “intersection” of the refracted rays were magnified, to stress the retrace distances. (b): The illustration of retraced ray from the 2D fish features. (c): The effect of the refraction; (d): The validation of the calculation for the 3D location of one simulated fish. The solid line is the result where the refraction is considered, and the dashed line is the calculation result that ignored the refraction effect. The scatters represent the ground truth.



The big, white plastic bowl was specially designed and manufactured to contain the fish. The choice of the shape was based on the fact that the fish tend to stay in the corner of the tank, when they entered an unfamiliar environment [200, 201]. Using a bowl-shaped container prevented the aggregation at the corners. Except for the corner effect, the bowl also provides no blind zone for all of the cameras, preventing the systematic disappear and reappearing of the fish in the video.

In order for the zebrafish to exhibit normal behaviour, they should have water conditions comparable to those used to house them. Typically, the fish need a temperature between 25 °C and 30 °C, and the water should be constantly filtered and sterilisation with UV light. All of the related apparatuses were placed outside the bowl-shaped tank, but inside the swimming pool, so that they would not affect the behaviours of the fish. The entire system was heated by two commercial heaters. The warm water was circulated into the inner bowl with a water pump. The bowl was able to exchange water with outside via small holes drilled inside. The measured temperature in the swimming pool ranges from 23 °C to 26 °C. The water circulation is turned off during observations of fish swimming.

The 3D shape of the tank was measured, so we know the exact boundary for the fish. The measurement was performed by placing markers on the surface of the tank, and then reconstruct the markers in 3D. Since the tank is rotationally symmetric around the  $z$ -axis, it is appropriate to describe its geometry in the cylindrical coordinate system with the height ( $z$ ) and the radius ( $r$ ). Figure 4.1 (Right) shows the results of the measurement, and the shape of the tank can be modelled by function  $z = 0.74r^2$ , where both length variables have the units of meter. The shape of the tank, together with the water level, are the boundaries for the movement of the fish.

## 4.2.2 Locating One Fish in 3D

Figure 4.2 summarises the essential concept to locate the 3D position with a three camera setup. The task of finding the 3D positions of zebrafish consists of two parts. The first part is finding the features of fish in individual cameras, as discussed in the chapter 3. These features corresponds to  $\mathbf{f}_i \in \mathbb{R}^3$  in Fig. 4.2(a).<sup>29</sup> The second part is to retrace the ray from the features  $\mathbf{f}_i$ , back to its original 3D location  $\mathbf{x}_i$ , as illustrated in Fig. 4.2 (b).

To carry out the 3D calculation procedure, we need to know the location, orientation, and optical details about the camera. This information can be obtained with the *camera calibration* [102, 202]. Essentially, the knowledge of the camera can be represented by a  $3 \times 4$  matrix  $\mathbf{P}_{3 \times 4}$ , named the *projection matrix*. For a 3D point  $\mathbf{x} = (x, y, z)^\top$ , the camera with projection matrix  $\mathbf{P}_{3 \times 4}$  will project the 3D point on a 2D plane, with coordinate  $(u, v)^\top$ , satisfying equation,<sup>30</sup>

$$\mathbf{P}_{3 \times 4} \cdot (x, y, z, 1)^\top = k(u, v, 1)^\top \quad (4.1)$$

where  $k$  can take any value. With proper decomposition of  $\mathbf{P}_{3 \times 4}$ , it is also possible to calculate the location of the camera centre, illustrated as  $\mathbf{c}$  in Fig. 4.2(a).

Equation 4.1 suggests an algebraical way to calculate 3D positions from 2D features. With known  $\mathbf{P}_{3 \times 4}$  and  $(u, v)$ , Eq. 4.1 offered 2 constrains on the values of  $\mathbf{x}$ . Therefore, the 3D vector  $\mathbf{x}$  can be uniquely determined by 2 or more “camera + feature” combinations.<sup>31</sup> However, the water in the fish tank will refract the light. Figure 4.2 (c) shows the effect of refraction, where the angle of incidence  $\theta_1$  and the angle of refraction  $\theta_2$  follows the Snell’s law:  $n_1 \sin \theta_1 = n_2 \sin \theta_2$ . In our experiment, we have  $n_1 = 1$  for the air, and  $n_2 = 1.333$  for the water. As a consequence, the calculation of  $\mathbf{x}$  involves the following steps,

1. For each feature  $\mathbf{f}_i$ , calculate its corresponding point on the water-air interface  $\mathbf{a}_i$ .
2. Calculate the direction of refracted ray  $\mathbf{v}_i$ .
3. Find the interception of multiple refracted rays, as the location of fish in 3D  $\mathbf{x}$ .

The calculation of  $\mathbf{a}_i$  and  $\mathbf{v}_i$  requires knowledge of the water-air interface, which was obtained during the camera calibration. Typically, we are free to choose the orientation and location of the *world coordinate frame*. And I set the frame so that the water-air interface is plane  $z = 0$ , as plotted in Fig. 4.2(a). This extra constrain ensures the value of  $\mathbf{a}_i$  being uniquely determined by a 2D feature  $(u, v)$ . Following Eq. 4.1:

$$\begin{pmatrix} P_{11} & P_{12} & P_{13} & P_{14} \\ P_{21} & P_{22} & P_{23} & P_{24} \\ P_{31} & P_{32} & P_{33} & P_{34} \end{pmatrix} \cdot \begin{pmatrix} a_x \\ a_y \\ 0 \\ 1 \end{pmatrix} = k \begin{pmatrix} u \\ v \\ 1 \end{pmatrix},$$

where  $\mathbf{a}_i = (a_x, a_y)^\top$ , and  $k$  is a scaling variable that can take any value. Notice there are 3 linear equations for 3 variables ( $a_x, a_y$  and  $k$ ), meaning

<sup>29</sup> The symbol  $\mathbf{f}_i$  stands for the 3D location of the detected 2D features. We need the knowledge of the camera to calculate  $\mathbf{f}_i$  from the features in the image.

<sup>30</sup> I use column vectors consistently in this thesis. For instance, the vector  $(x, y, z)^\top$  have the shape of  $4 \times 1$ ; while the vector  $(x, y, z)$  have the shape of  $1 \times 4$ .

<sup>31</sup> This method to find 3D location is called *triangulation*.

that we can easily calculate  $\mathbf{a}_i$ . The incident ray can be obtained from  $\mathbf{a}_i$  and corresponding  $\mathbf{c}_i$ . Applying Snell's law, we can calculate the direction of the refracted ray, yielding  $\mathbf{v}_i$ .

Ideally, the knowledge of the refracted rays ( $\mathbf{a}_i$  and  $\mathbf{v}_i$ ) from different cameras yields the 3D location of the fish. Realistically, because of the errors during the 2D feature detection and camera calibration, the retraced rays will not meet each other in 3D space exactly, as pictured in the inset in Fig. 4.2(a). Therefore, finding  $\mathbf{x}$  is a minimisation problem. And the value to be minimised is the sum of distances from  $\mathbf{x}$  to all the retraced rays. The distance from  $\mathbf{x}$  to the retraced ray from camera  $i$  is called the *retraced error*, noted as  $d_i$ . The value of  $d_i$  can be calculated as

$$d_i = |(\mathbf{x} - \mathbf{a}_i) \times \mathbf{v}_i|, \quad (4.2)$$

where the retraced ray from camera  $i$  passed through point  $\mathbf{a}_i \in \mathbb{R}^3$ , with the unit direction of  $\mathbf{v}_i \in \mathbb{R}^3$ . For the constant  $\mathbf{a}_i$  and  $\mathbf{v}_i$ , the squared sum of the retraced error is a function of  $\mathbf{x}$ , written as,

$$f(\mathbf{x}) = \sum_i d_i^2 = \sum_i (|\mathbf{x} - \mathbf{a}_i|^2 |\mathbf{v}_i^2| - |(\mathbf{x} - \mathbf{a}_i) \cdot \mathbf{v}_i|^2)$$

where the operator  $|\cdot|$  represents the norm of a 3D vector. We can think of  $f(\mathbf{x})$  as a scalar field (like temperature), and the minimum of the field can be found, by setting its gradient ( $\nabla f$ ) to zero. The relation ( $\nabla f = 0$ ) yields a set of linear equations,

$$\mathbf{M} \cdot \mathbf{x} = \mathbf{b}. \quad (4.3)$$

The values of  $\mathbf{M} \in \mathbb{R}^{3 \times 3}$  and  $\mathbf{b} \in \mathbb{R}^3$  can be calculated as,

$$\begin{aligned} \mathbf{M} &= \sum_i \mathbf{T}_i = \sum_i \mathbf{v}_i \cdot \mathbf{v}_i^T - \text{diag}(\mathbf{v}_i \circ \mathbf{v}_i) \\ \mathbf{b} &= \sum_i \mathbf{T}_i \cdot \mathbf{a}_i, \end{aligned}$$

where the symbol  $\circ$  represents the Hadamard product. The function  $\text{diag}(\mathbf{x})$  transform the vector  $\mathbf{x} \in \mathbb{R}^n$  to a diagonal matrix  $\mathbf{D} \in \mathbb{R}^{n \times n}$ , where  $D_{ii} = x_i$ . Solving the equation 4.3 is easy with standard linear algebra methods such as Gaussian elimination.<sup>32</sup>

Figure 4.2 (d) shows the calculation of the 3D location of simulated fish. The simulation was performed with software Blender, in which the experimental apparatus was constructed virtually. The video was recorded with virtual cameras in the software, and the aforementioned procedure was used to calculate the fish locations. Comparing the calculation result with the known ground truth, it is clear that our calculation yields correct results. Since the water is relatively deep (300 - 400 mm in depth) in our experiment, the effect of the refraction could not be ignored. In Fig. 4.2 (d) we also present the consequence of ignoring the refraction, which leads to a significant deviation from the ground truth.

<sup>32</sup> Using the Python language, the solution can be found with function `numpy.linalg.solve(M, b)`. In C++ the task can be performed with `M.ldlt().solve(b)`, where both  $\mathbf{M}$  and  $\mathbf{b}$  are matrix and vector from the `Eigen` library.

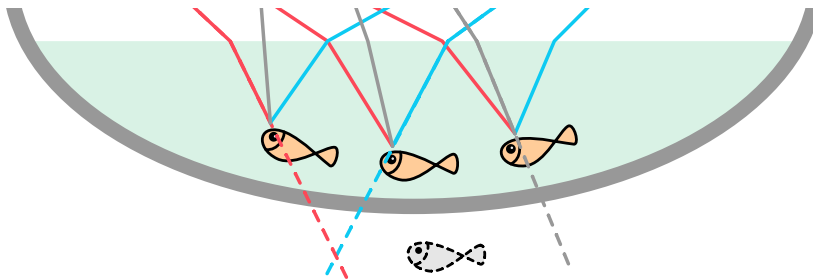


**Figure 4.3:** Tracking many fish with three cameras. The correct identity match from different views yields the intersection between the retraced rays, plotted as solid lines. The unmatched rays will not meet each other, illustrated by the dashed lines.

#### 4.2.3 Locating Many Fish in 3D

Calculating the 3D locations of many fish requires more work than locating one fish in 3D. This is because the different fish in different views (captured by different cameras) have to be matched correctly. An example of mismatched fish were shown in Fig. 4.3 as dashed lines. Since the three dashed lines correspond to different fish identities, they do not meet together. It is possible to use brute-force enumeration to generate all the possible identities matches, and then discarded the invalid ones. This algorithm was summarised in algorithm 1, where all possible solutions were generated in a triple **for** loop. These possible solutions were validated, and the invalid values were discarded.

---

**Algorithm 1:** Brute force algorithm for locate many fish in 3D.

---

**Result:** A collection of valid location  $\mathbf{x}$

```

for  $i \leftarrow 1, n_1$  do
    for  $j \leftarrow 1, n_2$  do
        for  $k \leftarrow 1, n_3$  do
             $\mathbf{x} \leftarrow$  Solution of  $\mathbf{M} \cdot \mathbf{x} = \mathbf{b}$ ;
            if  $\mathbf{x}$  is valid then
                put  $\mathbf{x}$  in Result

```

---

Naively, we will use the retraced error (Eq. 4.2) to validate every solution  $\mathbf{x}$ . The operation is summarised in algorithm 2, where a threshold value of  $d_m$  is used to discard the solutions with large retraced errors.

---

**Algorithm 2:** Validate a 3D location with retraced error.

---

```

 $d_i \leftarrow (\mathbf{x} - \mathbf{a}_i) \times \mathbf{v}_i;$ 
 $d_j \leftarrow (\mathbf{x} - \mathbf{a}_j) \times \mathbf{v}_j;$ 
 $d_k \leftarrow (\mathbf{x} - \mathbf{a}_k) \times \mathbf{v}_k;$ 
if  $(d_i + d_j + d_k)/3 < d_m$  then
    return True
else
    return False

```

---

However, this method is inadequate because of the correlation of the retraced error and the location of the fish: The retraced error is larger when the fish is deeper in the water. Such correlation is exhibited in Fig. 4.4, with simulated data. The correlation between error values and depth will lead to a systematic error, where the fish closer to the water-air interface will be preferred. Such correlation might originate from the arrangement of the

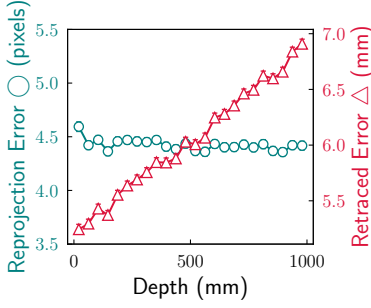


Figure 4.4: The reprojection error ( $\epsilon$ ) and retraced error ( $d_i$  in Eq. 4.2) as a function of fish location.

<sup>33</sup> Unfortunately, the reprojection error can not be used to find  $\mathbf{x}$ . The minimisation of  $\sum_i \epsilon_i^2$  will not yield a set of linear equations like Eq. 4.2.

camera. As they were pointed to the water from above, the retraced rays will be closer to each other when they were close to the water-air interface (see Fig. 4.3).

To overcome such bias, we can use the *reprojection error* [102] to separate the valid and invalid solutions of Eq. 4.3. The reprojection error is defined as

$$\epsilon_i = \left| (\mathbf{u}_x, v_x)^\top - (u, v)^\top \right| \quad (4.4)$$

where  $(u, v)^\top$  represents the 2D fish features in the camera, and  $(\mathbf{u}_x, v_x)^\top$  represents the projection of solution  $\mathbf{x}$  to camera  $i$ . The essential calculation for  $\epsilon$  is to re-project a 3D point  $\mathbf{x}$  back to the camera correctly, with the optical details being considered explicitly. The reprojection error exhibits no correlation with respect to the location of the fish, as shown in Fig. 4.4, which makes it a suitable choice for the validation of fish locations  $\mathbf{x}$ .<sup>33</sup> The algorithm for the validation with the reprojection error is summarised in algorithm 3.

---

**Algorithm 3:** Validate 3D location with reprojection error.

---

```

 $\epsilon_i \leftarrow \text{reprojection-error}(\mathbf{x}, i);$ 
 $\epsilon_j \leftarrow \text{reprojection-error}(\mathbf{x}, j);$ 
 $\epsilon_k \leftarrow \text{reprojection-error}(\mathbf{x}, k);$ 
if  $(\epsilon_i + \epsilon_j + \epsilon_k)/3 < d_m$  then
    return True
else
    return False

```

---

The result of 3D locating of 10 simulated fish were shown in Fig. 4.5. The simulated 3D data were reprojected to different cameras. These projected coordinates were mixed with Gaussian noise, forming the 2D features, to mimic the real life feature measurement. The information of the identity across different cameras was removed. Then our 3D locating method (algorithm 1 and 3) was used to calculate the 3D locations from these 2D features. It is clear from Fig. 4.5 that all of the 10 fish were correctly located, even in the existence of 2D measurement errors.

#### 4.2.4 Optimising the Stereo Matching

It is worth mentioning an optimisation idea proposed by Attanasi et al. to refine the stereo matching of fish identities<sup>34</sup> across different cameras [107]. The idea is to minimise the sum of reprojection error while ensuring the existence of all fish features in the valid solutions. For instance, in a collection of valid 3d locations  $\{\mathbf{x}_{ijk}\}$ , we want to minimise the sum of their corresponding reprojection errors (Eq. 4.4), by discarding some “bad” solutions. The result of this process is a subset of  $\{\mathbf{x}_{ijk}\}$ , noted as  $\{\mathbf{x}_{ijk}\}_{\text{opt}}$ . And the solutions in  $\{\mathbf{x}_{ijk}\}_{\text{opt}}$  are termed as the *optimised solutions*.

Without any constraint, the result of minimised error will be an empty set, meaning  $\{\mathbf{x}_{ijk}\}_{\text{opt}} = \emptyset$ . This is not very effective because the algorithm will trivially return nothing. A sensible way to remedy this situation is to

<sup>34</sup> The same process is called stereoscopic linking in [107].

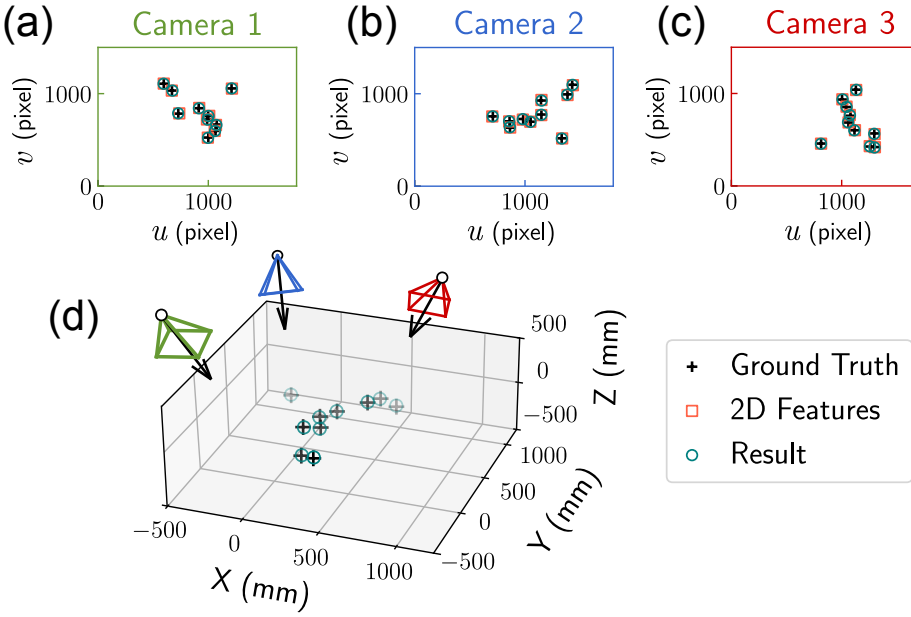


**Figure 4.5:** Calculating the 3D locations of 10 simulated fish locations. (a)-(c): the location captured by different cameras. The cross markers represent the known ground truth. The squares represent the measured 2D features, containing Gaussian noise. The circles represent the projection of the calculated 3D fish locations. (d): the ground truth and the calculated fish location in 3D.

enforce some kind of constraint, to ensure the existence of good results. The essence of the idea from Attanasi et al., is the following constraint,

$$\forall i \sum_{jk} x_{ijk} \geq 1, \forall j \sum_{ki} x_{ijk} \geq 1, \text{ and } \forall k \sum_{ij} x_{ijk} \geq 1,$$

where  $i, j, k$  are the indices for features in the 3 cameras. The symbol  $x_{ijk}$  represents a 3D boolean tensor, whose elements can take values of 0 or 1. If the value of  $x_{ijk} = 1$ , then the feature  $i$  in camera 1, the feature  $j$  in camera 2, and the feature  $k$  in camera 3 will form a optimised solution (in  $\{\mathbf{x}_{ijk}\}_{\text{opt}}$ ). Formally, the task can be written as a *linear programming* problem, written as,

$$\begin{aligned}
 & \text{Minimize} && \sum_{ijk} \epsilon_{ijk} \\
 & \text{Subject to} && \forall i \sum_{jk} x_{ijk} \geq 1, \\
 & && \forall j \sum_{ki} x_{ijk} \geq 1 \\
 & && \forall k \sum_{ij} x_{ijk} \geq 1
 \end{aligned} \tag{4.5}$$

This problem can be solved effectively by modern optimisation libraries, and they give satisfying results without significant increase in the computation time.

## What is “Linear Programming”

The method *linear programming* is a very useful optimisation method. We can use it to find the maximum value of a function, plus a set of linear constraints. Equation 4.5 is an example of the problem that linear programming could solve. To actually solve the problem, we need to apply some complicated algorithms like the *simplex algorithm*. The details of these algorithms are beyond the scope of this thesis.

Practically, we can use many existing libraries and softwares to solve the linear programming problems. I used the CPLEX package from the company IBM to carry out the linear programming calculation, following [107]. The package is not open-source, but offers free academic licence for researchers. Being a powerful solver, the CPLEX package can solve optimisation problems with quadratic constraints. We will utilise this feature in chapter 5 to remove overlapping particles.

Confusingly, the “programming” in the name does not refer to computer programmes. It originates from its first application, where George B. Dantzig was invited to solve an assignment problem for American military after world war II [203]. Internally, the schedules in the army was called the programme. Dantzig formulated the problem into a system of linear inequalities, and published a paper under the name of *Programming in a Linear Structure*. Later, he took the suggestion from a friend, and changed the name of this method to *linear programming*, while strolling on the Santa Monica beach in the summer of 1948 [203].

### 4.2.5 Assessing the Algorithm

For the experimental videos, the realistic accuracy of the algorithm depends on the distribution of the 2D error as well as the error in the camera calibration process. It is difficult to estimate the effects of theses uncertainties theoretically, and we refer the readers to [204] for relevant studies.

Practically, we can inspect the reprojected locations  $(u_x, v_x)$  to check the accuracy. An example is shown Fig. 4.6 (a), where the reprojected 3D tracking result as well as the detected 2D features were plotted on top of the captured image from one camera. The distribution of the reprojection error  $\epsilon$  was plotted in Fig. 4.6 (c), featuring a peak at  $\sim 2$  pixels. The distribution of  $\epsilon$  indicates that the reprojected coordinates  $(u_x, v_x)$  are close to the 2D features  $(u, v)$ . Such proximity should give us confidence about the algorithm on the experimental data. Notably, the 3D locating algorithm is even capable of discarding some invalid 2D features, since their corresponding invalid 3D result would be discarded by algorithm 3.

The complexity of the 3D locating algorithm is  $\mathcal{O}(n^3)$ , because of the triple `for` loop in algorithm 1. The performance of the algorithm is shown in Fig 4.6 (d), where the wall time<sup>35</sup> exhibits the expected cubic increase. To get even better performance, one needs to improve the algorithm to reduce the complexity from  $\mathcal{O}(n^3)$ . A possible option is to exploit the epipolar

<sup>35</sup> The wall time refers to time spent in real life, counted by a clock on the “wall”

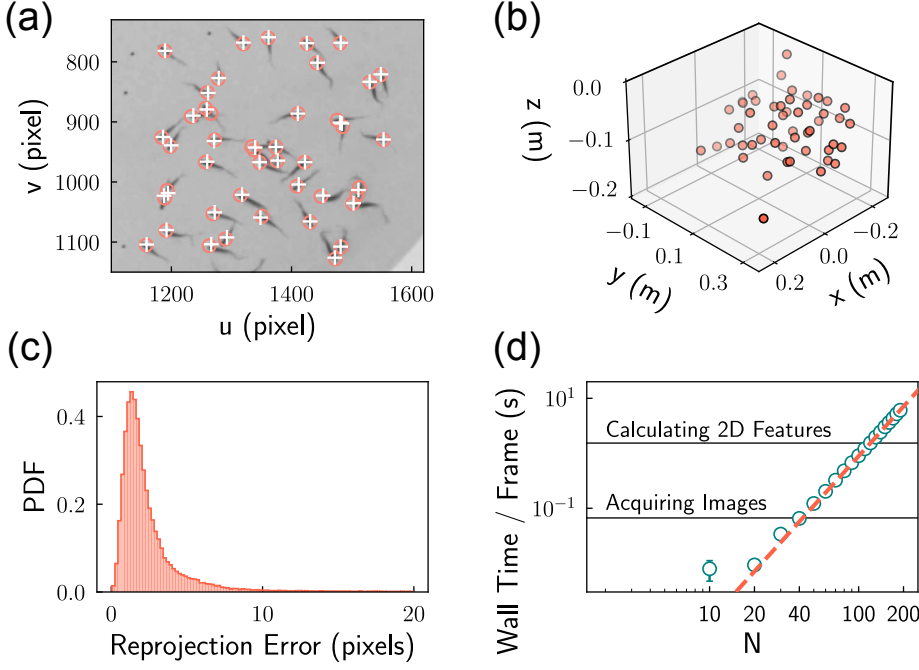


**Figure 4.6:** (a) An image of 40 zebrafish in the experimental setup. The detected 2D features, corresponding to  $(u, v)$  in Eq. 4.4, were plotted as white circles. The re-projected 3D tracking result, corresponding to  $(u_x, v_x)$  in Eq. 4.4, were plotted as the red cross markers. We cropped the image to focus on the fish group. (b) The reconstructed 3D locations of 40 zebrafish from three different cameras. (c) The distribution of reprojection error  $\epsilon$ . (d) The wall time of the 3D locating algorithm for different numbers of fish. The dashed line shows the cubic fitting ( $y = ax^3 + b$ ).

geometry [102], which can reduce the complexity of the algorithm. Further optimisation of the 3D locating algorithm will be an important task of this project in the future.

Even though the 3D locating algorithm was not optimised, it is good enough<sup>36</sup> for relatively small group sizes (less than 100 fish). For these small numbers, the bottleneck of the calculation is the 2D feature detection, which took about 2s for each frame. With an image acquisition frequency of 15 FPS, the 3D locating calculation for group size  $< 40$  can even be performed in real time, if the 2D feature calculation time can be decreased dramatically.

## 4.3 Results

The 3D tracking yields the positions of the fish. From the positions, we can estimate the spatial distribution, and measure the structure of a group of fish.

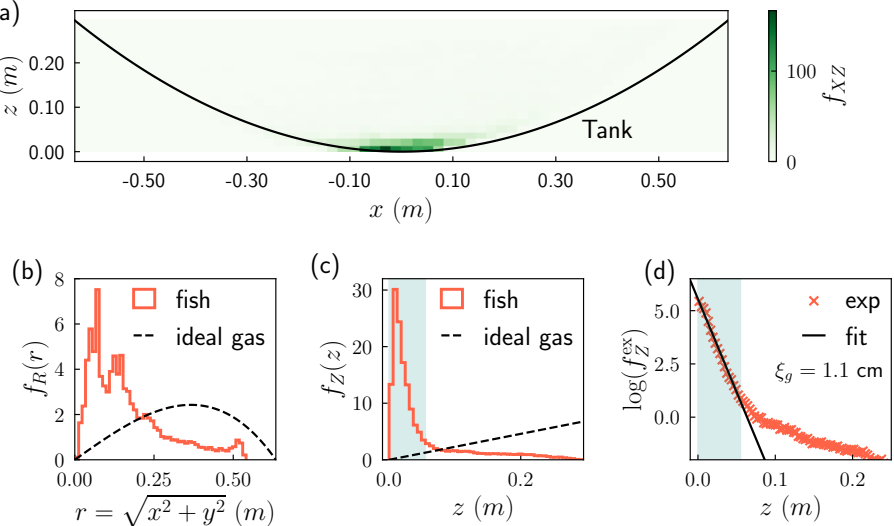
### 4.3.1 A Single Fish

Figure 4.7 (a) shows the joint probability density function (PDF) of the  $x$  and  $z$  coordinates of the fish, noted as  $f_{XY}$ . This spatial distribution shows that the fish tend to stay in the bottom of the tank. We observe this behaviour repeatedly, when the fish were subjected to a new environment. It is likely to be related to the “depth preference” of zebrafish [200], where the fish prefer deep water naturally. In addition, the increasing anxiety would also drive the fish to go to the bottom of the tank [205, 206].

The distribution of the planer radius,  $r = \sqrt{x^2 + y^2}$  is shown in Fig. 4.7 (b), noted as  $f_R(r)$ . The shape of  $f_R(r)$  is affected by the geometry of the tank. To understand the effect of this boundary, we calculated the

<sup>36</sup> To achieve high performance, a fast programming language is important: the result in Fig. 4.6 was from an implementation using the C++ language, which is 1,000 times faster than a Python implementation.

**Figure 4.7:** The spatial distribution of one zebrafish. (a) The joint probability density function of  $x$  and  $z$  components of the fish. (b) The PDF for the planer radius  $r$  of the fish. The dashed line shows the same PDF for the ideal gas particles distributed uniformly in the tank. (c) The PDF for the  $z$  component of the fish. The dashed line shows the same PDF for the ideal gas particles distributed uniformly in the tank. (d) The semi-log plot of the excess PDF,  $f_Z^{\text{ex}}$  in Eq. 4.6, for the  $z$  component for the fish. Fitting its initial decay revealed a lengthscale of 1.1 cm. The region of the initial decay is highlighted in (c) and (d).



distribution of the ideal gas particles, distributed uniformly inside the fish tank (see chapter 6 for details). Compared to the ideal gas particles, the distribution of  $r$  is closer to the centre. The shifted distribution of the fish is related to their depth preference, since the fish will be forced to the central region of the tank as they swim deeper in the water. There are two peaks in  $f_R(r)$ , and this bimodal feature can be explained by the holes drilled on the tank, which will be discussed in section 4.3.5.

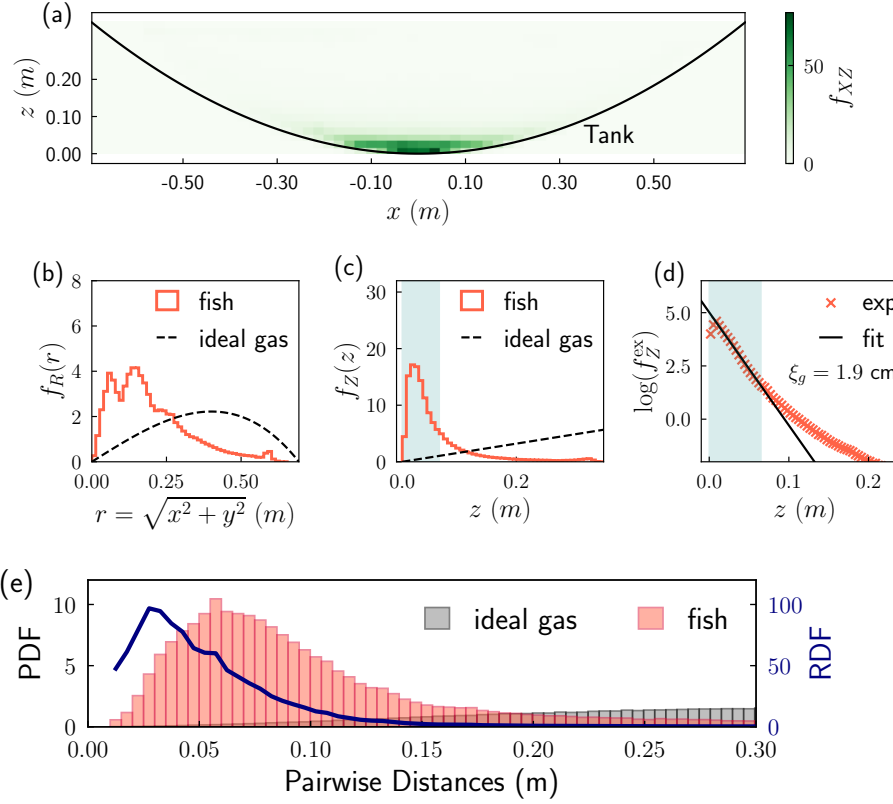
The distribution of  $z$  component of the coordinate of the fish, noted as  $f_Z(z)$ , is shown in Fig. 4.7 (c), which presents a very sharp peak around  $z = 0$  m. To get a better understanding of the fish, we calculated the *excess probability density function*,  $f_Z^{\text{ex}}(z)$ , as

$$f_Z^{\text{ex}}(z) = \frac{f_Z^{\text{fish}}(z)}{f_Z^{\text{id}}(z)} \quad (4.6)$$

where the term  $f_Z^{\text{fish}}(z)$  represents the height distribution of the fish, while  $f_Z^{\text{id}}(z)$  represents the distribution of the ideal gas particles. The logarithm of  $f_Z^{\text{ex}}(z)$  is shown in Fig. 4.7 (d), featuring a linear decay of the peak, and a subsequent tail. This initial exponential decay is surprising, and it is reminiscent of the height distribution of one colloidal particle, under the gravitational field [207, 208]. We can fit this exponential decay with the following function,

$$f_Z^{\text{ex}}(z) = a \exp\left(\frac{z}{\xi_g}\right)$$

where  $a$  is free parameter, and  $\xi_g$  is a length scale related to the depth preference of the fish. The value of  $\xi_g$  is a measure of the “effective gravity” exhibited by fish, that is related to its depth preference. For one adult zebrafish, the value of  $\xi_g$  is 1.2 cm. The effective gravity for the fish will be further discussed in chapter 6.



### 4.3.2 Two Fish

The spatial distribution of 2 zebrafish is presented in Fig 4.8. The behaviour of two fish is similar to that of one fish, exhibiting the typical depth preference. However, the distribution of two fish is broader compared to that of one fish. The broader distribution indicates an increased randomness, which might relate to the decreased level of anxiety<sup>37</sup>, as the fish were swimming in pairs. In other words, one fish might be very vigilant in a new environment, exhibiting the anxiety-driven depth preference [205], which leads to a narrow distribution of  $f_Z(z)$ . For a pair of fish, this depth preference was reduced. The fitting result of  $f_Z^{\text{ex}}(z)$  yields a  $\xi_g$  value of 1.8 cm, which is larger than the  $\xi_g$  value of one fish (1.2 cm), as a result of reduced depth preference.

The fish-fish interaction can be probed by the distribution of the pairwise distances as well as the radial distribution function (RDF), as discussed in chapter 3. The probability density function (PDF) of the pairwise distance of 2 fish was shown in Fig. 4.8, along with the corresponding PDF of the ideal gas particles uniformly distributed in the fish tank. The PDFs of the fish distance exhibit a peak around 5 cm, which is dominated by the inhomogeneity of the density distribution.

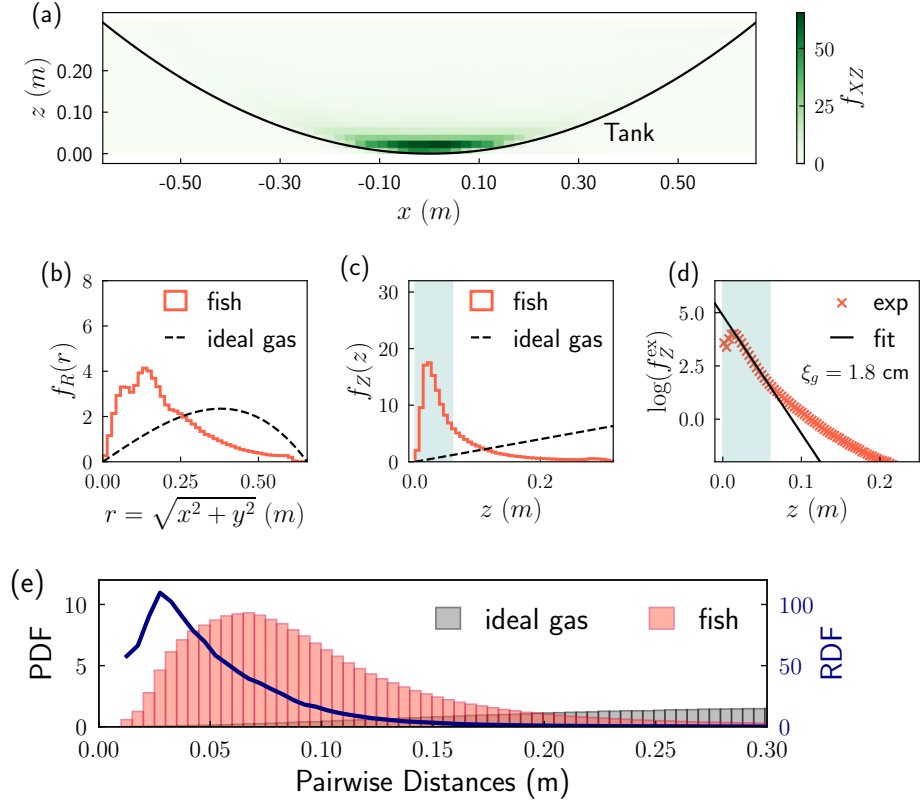
The RDF of 2 fish in the system exhibits a peak around 0.03m, with a height<sup>38</sup> value of  $\sim 100$ . The height value is significantly larger, comparing with the RDF peak height ( $\sim 15$ ) of 2 fish in 2D. However, this does *not* imply the fish were swimming in a more cohesive fashion in 3D. Instead, the RDF describes the depth preference of the fish, which generated significant density inhomogeneity, illustrated in Fig. 3.10 (a). In other words, the fish

**Figure 4.8:** The spatial distribution of two adult zebrafish. (a) The joint probability density function of  $x$  and  $z$  components of the fish. (b) The PDF for the planer radius  $r$  of the fish. The dashed line shows the same PDF for the ideal gas particles distributed uniformly in the tank. (c) The PDF for the  $z$  component of the fish. The dashed line shows the same PDF for the ideal gas particles distributed uniformly in the tank. (d) The semi-log plot of the excess PDF,  $f_Z^{\text{ex}}$  in Eq. 4.6, for the  $z$  component for the fish. Fitting its initial decay revealed a lengthscale of 1.9 cm. The region of the initial decay is highlighted in (c) and (d). (e) The PDF of pairwise distances of the fish and the ideal gas particles in the tank. The ratio of the two, the radial distribution function (RDF), is plotted as a solid line.

<sup>37</sup> To the best of my knowledge, there is no direct proof to suggest that zebrafish perceive less danger in a larger group. It is a reasonable speculation, since zebrafish form groups naturally in the wild [21].

<sup>38</sup> For the densely packed fluid, like a collection of hard spheres at volume fraction of 54%, the peak height is  $\sim 6$ .

**Figure 4.9:** The spatial distribution of three adult zebrafish. (a) The joint probability density function of  $x$  and  $z$  components of the fish. (b) The PDF for the planer radius  $r$  of the fish. The dashed line shows the same PDF for the ideal gas particles distributed uniformly in the tank. (c) The PDF for the  $z$  component of the fish. The dashed line shows the same PDF for the ideal gas particles distributed uniformly in the tank. (d) The semi-log plot of the excess PDF,  $f_Z^{\text{ex}}$  in Eq. 4.6, for the  $z$  component for the fish. Fitting its initial decay revealed a lengthscale of 1.8 cm. The region of the initial decay is highlighted in (c) and (d). (e) The PDF of pairwise distances of the fish and the ideal gas particles in the tank. The ratio of the two, the radial distribution function (RDF), is plotted as a solid line.



appear to swim together in a more cohesive fashion in 3D, according to the numerical value of the RDF. But the cohesion was not driven by the (biological) fish-fish attraction. Instead, these fish were just bounded together by their interaction with the environment, i.e. the depth preference. This bias induced by the depth preference can be corrected with advanced sampling method, which will be covered in chapter 5.

### 4.3.3 Three Fish

The spatial distribution of 3 zebrafish is presented in Fig 4.9. Being similar to the 1-fish and 2-fish system, a group of 3 zebrafish presents the depth preference, indicated by the biased joint PDF of  $z$  and  $z$  components of the fish coordinates. The PDFs ( $f_Z(z)$ ,  $f_R(r)$ , and  $f_{XZ}$ ) of 3 fish is very similar to the results from 2 fish experiments. This similarity was also observed in the 2D experiments (section 3.3.2).

The distribution of the pairwise distance of 3 zebrafish exhibits one peak around 0.08m. The length scale matched the size of the high-density blob in Fig. 4.9 (a), thanks to the depth preference of the fish. The RDF of 3 fish is similar to the RDF of 2 fish, with a peak at around 0.03 m. The height of the peak is close to 100, due to the depth preference of the fish, as discussed in section 4.3.2.

### 4.3.4 Many Fish

Figure 4.10 shows the spatial distribution of 50 adult zebrafish, as well as the distribution of their pairwise distances and the RDF. The depth

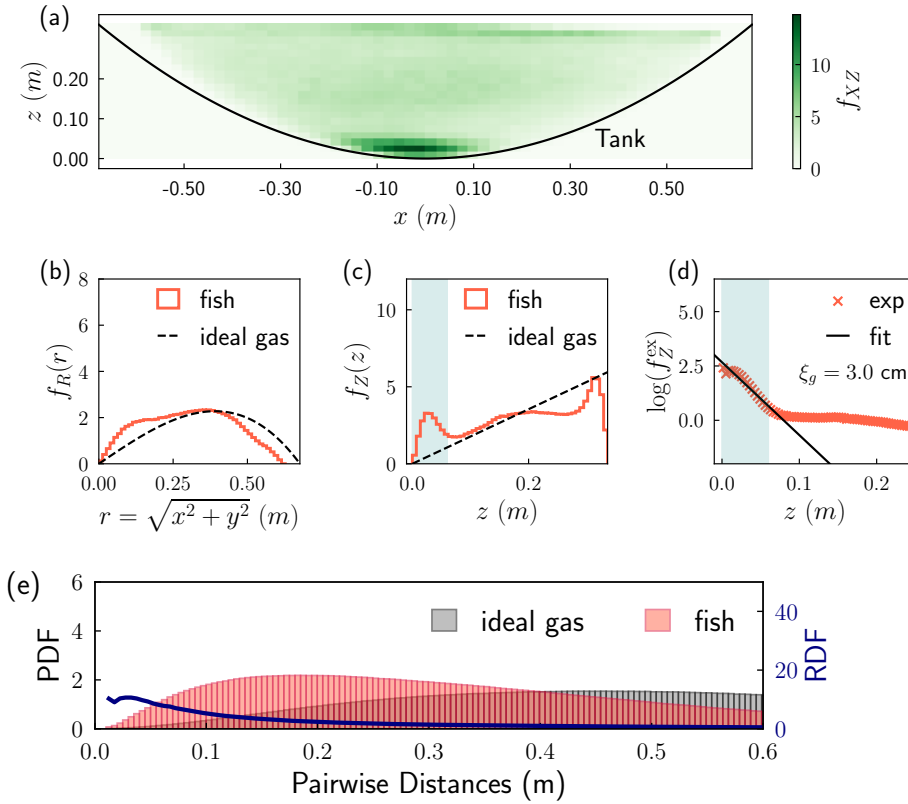


**Figure 4.10:** The spatial distribution of fifty adult zebrafish. (a) The joint probability density function of  $x$  and  $z$  components of the fish. (b) The PDF for the planer radius  $r$  of the fish. The dashed line shows the same PDF for the ideal gas particles distributed uniformly in the tank. (c) The PDF for the  $z$  component of the fish. The dashed line shows the same PDF for the ideal gas particles distributed uniformly in the tank. (d) The semi-log plot of the excess PDF,  $f_Z^{\text{ex}}$  in Eq. 4.6, for the  $z$  component for the fish. Fitting its initial decay revealed a lengthscale of 3.0 cm. The region of the initial decay is highlighted in (c) and (d). (e) The PDF of pairwise distances of the fish and the ideal gas particles in the tank. The ratio of the two, the radial distribution function (RDF), is plotted as a solid line.

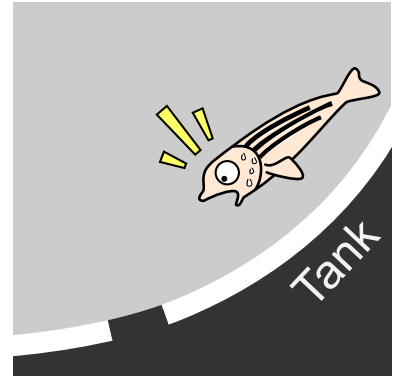
preference is obvious for a group of 50 fish, as shown in the joint PDF of  $x$  and  $z$  components of the fish coordinates. However, the distribution is more homogeneous comparing with the 1/2/3 fish results. This homogeneity could be the result of reduced depth preference, as the  $\xi_g$  value for 50 zebrafish is larger than that of the 1/2/3 fish. Biologically, the reduction of depth preference (the increase of  $\xi_g$ ) can be explained by our assumption, that the fish perceive less danger in a larger group.

The distribution of the  $z$  component, interestingly, exhibits two separated peaks. One of the peak is close to  $z = 0$  m which can be explained with the depth preference. The other peak is located at  $z = 0.35$  m, which corresponds to the top of the tank. This suggests the fish were also attracted by the water-air interface. Such bimodal distribution is likely due to the biological preference of the fish, which will be further analysed in chapter 5.

The 50 zebrafish also shows a broad distribution for their pairwise distances. This can be explained by the reduced density inhomogeneity of the fish. Consequently, the group of 50 fish appears to be less cohesive, indicated by the absence of sharp peak in their RDF, as shown in the bottom panel of Fig. 4.10. The observation that a large group of fish exhibits less cohesion and less spatial inhomogeneity, was also captured by the 2D fish experiments shown in section 3.3.4.

### 4.3.5 The Holes on the Tank

The holes drilled on the surface of the tank had an unexpectedly large effect on the spatial distribution of the zebrafish. These holes were designed for the



The holes on the tank affected the zebrafish.

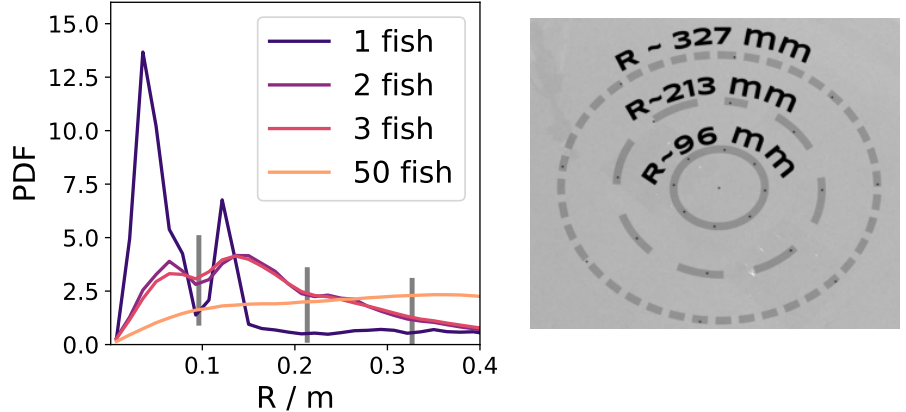


**Figure 4.11:** Left: the distribution of the planar radius ( $R$ ), where the location of the drilled holes were marked with vertical lines. Right: a photo of the bottom of the fish tank, highlighting the location and planar radius of the holes.

circulation of the water in the tank. They appear as black dots in Fig. 4.11 (right). However, the location of these holes matched the  $R$  values of the density distribution, where the discontinuous singularity happens, as shown in Fig 4.11 (left). This indicates that the fish actively avoids swimming on top of these holes.

For the distribution of 1 fish, the fish-hole interaction is very significant, indicated by a very clear separation of peaks around  $R = 0.1$ . Such separation is less significant in from the result of 2 fish and 3 fish experiments. For 50 fish, the effect of the holes is not observed in Fig. 4.11. The result is consistent with the observation in 2D, were the fish-tank interaction dominates the 1/2/3 fish behaviour, while the fish-fish interaction dominates the behaviour of 50 fish. Such observation indicates the necessity for the large group animal behaviour experiments, if we are interested in the interaction between animal individuals.

This information about the fish-tank interaction is important for the purpose of the modelling. In chapter 6 we will show that a small group of fish can be modelled as a system in equilibrium with pairwise interaction, under the influence of the tank, the gravity, as well as the holes. The Boltzmann energy weight, as a result of our equilibrium assumption for the system, gives a good match for the observed spatial distribution.

## Summary of Chapter 4

- Locating fish in 3D requires synchronised images from different cameras. We Presented the experimental setup for this task.
- We introduced the idea to calculate the 3D location of one fish from its corresponding 2D features from different cameras.
- We presented a brute-force algorithm to locate multiple fish in 3D, highlighting the importance of the reprojection error. We also introduced the optimisation of the result with the help of linear programming. The accuracy and complexity of the multiple-fish locating algorithm is assessed.
- We reported the analysis on the coordinates of zebrafish in a 3D environment, featuring different fish numbers.

### One Fish

The fish tend to swim near the bottom of the tank. The height distribution exhibit an exponential decay, featuring the depth preference of the fish, which can be characterised by a length scale  $\xi_g$ .

### Two Fish

The fish tend to swim near the bottom of the tank, with slightly increased  $\xi_g$  value, suggesting a reduced depth preference. The depth preference dominated the radial distribution function.

### Three Fish

The behaviour of three adult zebrafish is very similar to that from two fish.

### Fifty Fish

The spatial distribution of 50 fish is more uniform, compared to the 1/2/3 fish results. As a result, the RDF of 50 zebrafish shows significantly reduced cohesiveness.

- Surprisingly, the fish responded strongly to the small holes drilled on the surface of the tank, leading to the peak split in the distribution of the planar radius, for the 1/2/3 fish behaviour. For 50 fish, the interaction between the fish and the holes was not observable, indicating the behaviour of 50 zebrafish were dominated by the fish-fish interaction, instead of the interaction between the fish and the environment.

# Chapter 5

## Analysing Zebrafish Behaviour

鱼相忘乎江湖

---

庄子

### 5.1 Introduction

The experimental setup described in chapters 3 and 4 provides the coordinates of individual fish in 2D or 3D. These numbers give us the information about the structure of the fish group. To further obtain the “dynamics” of the system, we need to *link* the coordinates into trajectories<sup>39</sup>. With the linked trajectories, we have access to the full phase space that a group of fish explored. This information is similar to that we get from a molecular dynamics simulation, or a real-space colloidal experiment.

From the trajectories, we can analyse the *correlations* of the fish in the space and time. For instance, we may ask questions like “if a fish appears at location A, what is the chance that another fish appears at location B?”, or “if this fish is swimming very fast at time  $t$ , what is the most likely speed of the same fish at time  $t + \delta t$ ?”. Answers to these questions<sup>40</sup> gave us the characteristic lengthscale (the correlation length) and timescale (the relaxation time) of the fish group. These quantities could help us understanding the collective behaviour of the system. For instance, the divergence of the correlation length and the relaxation time may indicate the system being at a critical point [209]; and the existence of dynamical heterogeneity is a feature for glassy systems [210].

For the purpose of pursuing lengthscales and timescales, a more explicit and biology-orientated example is the dynamic scaling hypothesis [121]. For animal systems near a critical state, a universal form of their spatial-temporal correlation function,  $\hat{C}(k, t)$ , was proposed from this hypothesis, written as

$$\hat{C}(k, t) = f(t/\tau_k; k\xi); \quad \tau_k = k^{-z} g(k\xi), \quad (5.1)$$

where  $k$  and  $t$  represent the wavenumber (the reciprocal space) and the time, while the  $\tau_k$  and  $\xi$  are the typical timescale and lengthscale, respectively.

The functions  $f(x)$  and  $g(x)$  are scaling functions, which only depend on one variable,  $k\xi$ . The exact forms of  $f$  and  $g$  are often not important, since the truly remarkable thing about Eq. 5.1 is that all the correlations will depend only on the correlation length  $\xi$ . That is to say, we can predict the behaviour of the animals knowing just one quantity (`lcorr`), which absorbs many biological features of the animal group. This reductionist picture of animal behaviour seemed too good to be true, but it was indeed supported by field observations of midges [121].<sup>41</sup>

In this chapter, the necessary data processing tools will be introduced. These methods include the refinement of the coordinates and the linking procedure, which transforms the coordinates into trajectories. With the trajectories, we will calculate the useful structural and dynamical quantities, to describe the behaviour of the fish. To obtain different lengthscales and timescales, some spatial and temporal correlation functions will be calculated. All the analysis in this section are applicable for results from both 2D and 3D observations, being potentially useful for the analysis of different animal behaviour.

Having established all the necessary analytical tools, we will study the behaviour of 50 zebrafish from 2D observations (chapter 3) and 3D observations (chapter 4). Crucially, we will see that the behaviour of a group of zebrafish can be described by a dimensionless number, such as the ratio of two lengthscales, the persistence length and the nearest neighbour distance. This conclusion will be rationalised in chapter 6, in which we explain the behaviour of fish with a simple self-propelling particle model with alignment interactions.

<sup>41</sup> However, there is a catch. This idea of a universal behaviour for animals only works, if the biological system were in a mysterious “critical state”, whose nature is not exactly clear. In addition, the existence of such criticality is questionable, with evidence suggesting the flocking transition is discontinuous[160].

## 5.2 From Locations to Better Locations

To correctly carry out the linking problem, where coordinates were connected into trajectories, it is necessary to preprocess the locations of the fish. The calculated fish locations contains overlapping pairs, where two fish locations appear at an impossibly close distance. This error happens during the tracking procedure introduced in chapter 3 and 4. In the practical calculation, these overlapping coordinates make the linking result inaccurate. A process to refine the coordinates, getting rid of the overlaps, helps the final quality of the trajectory significantly.

### 5.2.1 Removing Overlapping and *Hard* Particles

When the overlap happens, the correct result can be obtained by discarding one “bad” coordinate. Conceptually, the process is identical to the way we optimise the stereo matching result in section 4.2.4. Likewise, we will apply the linear programming method, to obtain a set of optimised coordinates ( $\{\mathbf{x}\}_{\text{opt}}$ ) from the measured, error-prone coordinates ( $\{\mathbf{x}\}$ ).

Suppose there are  $N$  particles in total, and we wish to find  $K$  non-overlapping particles, where each particle has an uncertainty value<sup>42</sup> of  $e_i$ . The task can be written as a minimisation problem with quadratic constraints:

<sup>42</sup> For 2D coordinates, the error values can be the brightness of the coordinate in the foreground image (section 3.2.3). For 3D coordinates, the error values would be the reprojection error defined in Eq. 4.4.

$$\begin{aligned}
& \text{Minimize} && \sum_i e_i x_i \\
& \text{Subject to} && x_1 d_{12} x_2 \leq \sigma \\
& && x_1 d_{13} x_3 \leq \sigma \\
& && \vdots \\
& && x_i d_{ij} x_j \leq \sigma \\
& && \sum_i x_i = K
\end{aligned} \tag{5.2}$$

where  $d_{ij}$  is the distance between particle  $i$  and  $j$ ,  $\sigma$  is the diameter of the non-overlapping hard core of each particle, and  $K$  is the total number of particles. The variable  $x_i$  is an element in a boolean array, that take the values of 0 and 1. If  $x_i = 1$ , then the  $i$ th coordinate will be retained in  $\{\mathbf{x}\}_{\text{opt}}$ . If  $x_i = 0$  the corresponding location will be discarded. The solution to above cost function and constraints can be effectively solved by the CPLEX optimisation package.

The value of  $K$  is a free parameter, whose optimum value is difficult to estimate. A working heuristic is to find the maximum value of  $K$  that satisfies the constraint in Eq. 5.2. Therefore, the overlapping problem is solved with the following algorithm<sup>43</sup>.

---

**Algorithm 4:** Remove overlapping locations.

---

**Data:** Locations  $\{\mathbf{x}\}$ , cutoff  $\sigma$   
**Result:** Optimised locations  $\{\mathbf{x}\}_{\text{opt}}$

$$\begin{aligned}
N &\leftarrow \text{Size-of}(\{\mathbf{x}\}); \\
\{d_{ij}\} &\leftarrow \text{Pairwise-distance}(\{\mathbf{x}\}); \\
\text{for } K &\leftarrow N \text{ to } 1 \text{ do} \\
\{x_i\} &\leftarrow \text{Solve Eq. 5.2}; \\
\text{if } \{x_i\} &\text{ is valid then} \\
&\quad \text{break}; \\
\{\mathbf{x}\}_{\text{opt}} &\leftarrow \emptyset; \\
\text{for } i &\leftarrow 1 \text{ to } N \text{ do} \\
\text{if } x_i > 0 &\text{ then} \\
&\quad \text{Put } \mathbf{x}_i \text{ in } \{\mathbf{x}\}_{\text{opt}};
\end{aligned}$$


---

An alternative choice, instead of the linear programming approach, is to apply a greedy algorithm. The idea is to gradually add “good particles” to the optimised set  $\{\mathbf{x}\}_{\text{opt}}$ , until particle overlap happens<sup>44</sup>. This approach is summarised in algorithm 5. The greedy algorithm is easier to implement, but it is not guaranteed to find the optimum solution [211]. This is because the greedy algorithm only compares the quality of two solutions iteratively, rather than trying to find the best solution out of all possibilities.

Figure 5.1 shows the removal of overlapping particles with both algorithm 4 and 5. The locations were sampled randomly, representing the ideal gas particles. For both algorithms, the overlap was successfully removed while the remaining particles are those with smaller error values. However, the linear programming method find more non-overlapping particles, com-

<sup>43</sup> Algorithm 4 can also be applied in the real-space colloidal microscopy, where the error term can be the inverse of the fluorescent intensity (to favour brighter centres) or the response to a kernel function (to favour a particular shape).

<sup>44</sup> Equivalently, we can use algorithm where “bad particles” were removed from  $\mathbf{x}_{\text{opt}}$  gradually.

---

**Algorithm 5:** Greedy algorithm to remove overlapping locations.

---

**Data:** Locations  $\{\mathbf{x}\}$ , cutoff  $\sigma$ , error  $\{e\}$

**Result:** Optimised locations  $\{\mathbf{x}\}_{\text{opt}}$

$N \leftarrow \text{Size-of}(\{\mathbf{x}\})$ ;

$\{\mathbf{x}\}_{\text{opt}} \leftarrow \emptyset$ ;

$\{d_{ij}\} \leftarrow \text{Pairwise-distance}(\{\mathbf{x}\}_{\text{opt}})$ ;

**while**  $\min(\{d_{ij}\}) > \sigma$  **do**

$i \leftarrow \text{argmin}(\{e\})$ ;

    put  $\mathbf{x}_i$  in  $\{\mathbf{x}\}_{\text{opt}}$ ;

$\{d_{ij}\} \leftarrow \text{Pairwise-distance}(\{\mathbf{x}\}_{\text{opt}})$ ;

---

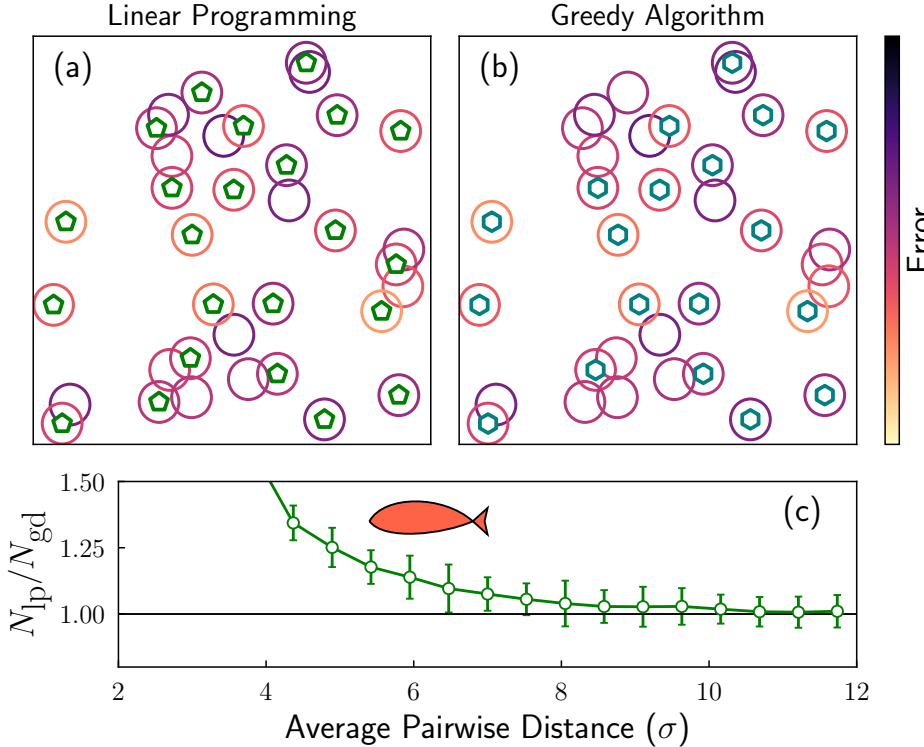


**Figure 5.1:** The removal of overlapping particles with different algorithms. The circles represent particles. Their locations corresponds to  $\{\mathbf{x}\}$ , and their radius values are the hard core diameters ( $\sigma$  in Eq. 5.2). The colour of the circles represents the error to be minimised. (a): the result of solving Eq. 5.2, implemented as algorithm 4. The pentagons represent the optimised result ( $\{\mathbf{x}\}_{\text{opt}}$ ). (b): the result of greedy algorithm (algorithm 5). The hexagons represent the optimised result ( $\{\mathbf{x}\}_{\text{opt}}$ ). (c): the number ratio of optimised positions from algorithms 4 ( $N_{\text{ip}}$ ) and algorithm 5 ( $N_{\text{gd}}$ ) as a function of average pairwise. The positions were randomly sampled with different densities. The error bars were the standard error calculated from 25 different simulations.

pared to the greedy algorithm. This is expected, as the constrain of the linear programming forced the algorithm to maximise the size of  $\{\mathbf{x}\}_{\text{opt}}$ .

The systematic difference between the two algorithms is presented in Fig. 5.1(c). The ratio between the number of optimised particles, detected by different algorithms is plotted against the average pairwise distance of the particles. The linear programming method consistently generates larger optimised set, especially in the high density region, when the average pairwise distance is close to 2. For the dilute system, the difference between the two algorithms were negligible. The average pairwise distance of zebrafish were close to 20 cm[1, 182], while the average body length of the fish was  $\sim 3$  cm. As a result, the fish is similar to the ideal gas particles where the average pairwise distance is close to  $6\sigma$ , where the difference between the two algorithms is significant. Because of its better performance, the linear programming method was selected to remove the overlapping particles. In

the experiments, the size of the hard core was chosen to be 1 cm, a value that corresponds to the width of the fish.

### 5.2.2 Removing Overlapping and *Soft* Particles

The overlap removing algorithm can be improved slightly, to change the strictly hard length scale ( $\sigma$ ) to a “softer” counterpart. The idea was borrowed from the soft margin classification problem for the support vector machine (SVM) algorithm in the machine learning (ML) community [189]. Following the naming tradition in ML literatures, we introduce a *slack variable*  $\zeta_{ij}$  for particle  $i$  and  $j$ . The value of  $\zeta_{ij}$  measures how soft the repelling is between two particles. The larger  $\zeta_{ij}$  value corresponds to a softer particle. In the language of physics, the  $\zeta_{ij}$  variables are essentially the pairwise potential energy between atoms, whose sum ( $\sum_i \sum_j \zeta_{ij}$ ) gives the internal energy of a system, and should be minimised.

Formally, the overlap removing with soft interaction can be written down as follows,

$$\begin{aligned} \text{Minimize} \quad & \sum_i (e_i + \mu)x_i + \beta \sum_i \sum_j \zeta_{ij} \\ \text{Subject to} \quad & x_1 d_{12} x_2 \leq \sigma - \zeta_{12} \\ & x_1 d_{13} x_3 \leq \sigma - \zeta_{13} \\ & \vdots \\ & x_i d_{ij} x_j \leq \sigma - \zeta_{ij} \end{aligned} \tag{5.3}$$

which is a slight modification of Eq. 5.2. Firstly, we remove the constraint that forces the total number of particles to equal  $K$ . There are also two additional parameters,  $\mu$  and  $\beta$ . The parameter  $\mu$  controls the number of total particles in  $\{\mathbf{x}\}_{\text{opt}}$ . The smaller the  $\mu$  value is, the more particles will be included in the optimised set. In the context of statistical mechanics, we can think of  $\mu$  as the *chemical potential*. The parameter  $\beta$  before the energy term  $\sum_i \sum_j \zeta_{ij}$  controls the softness of the excluding zone around each coordinate, sharing the same meaning with the hyperparameter  $C$  in the SVM algorithm. Within the context of statistical physics, the parameter  $\beta$  is conceptually identical to the *inverse temperature*. Reducing the value of  $\beta$ , we increase the temperature, and we make every particle appear softer.

The solution of Eq. 5.3 will be identical to the solution of Eq. 5.2, when  $\beta \rightarrow \infty$  and  $\mu \sim -\max(\{e_i\})$ . These solutions were ascribed to the “hard removal” region in Fig. 5.2(c). Fixing the value of  $\mu$  but decrease  $\beta$  gradually, move overlap will be allowed, and more particles will be detected. These regions were labelled as “soft removal” in Fig. 5.2. When the values of both  $\mu$  and  $\beta$  were small, all the particles will be retained in  $\{\mathbf{x}_{\text{opt}}\}$ , corresponding to the “no removal” region in Fig. 5.2(c). On the other hand, the solution of Eq. 5.3 will lead to the removal of all particles, when the value of  $\mu$  is large. This scenario corresponds to the “excess removal” region in Fig. 5.2(c).

This soft overlap-removal algorithm was implemented, but not tested nor used for the fish data. This is because the determination of the parameters,  $\mu$  and  $\beta$ , is difficult. However, this soft overlap remove algorithm presents

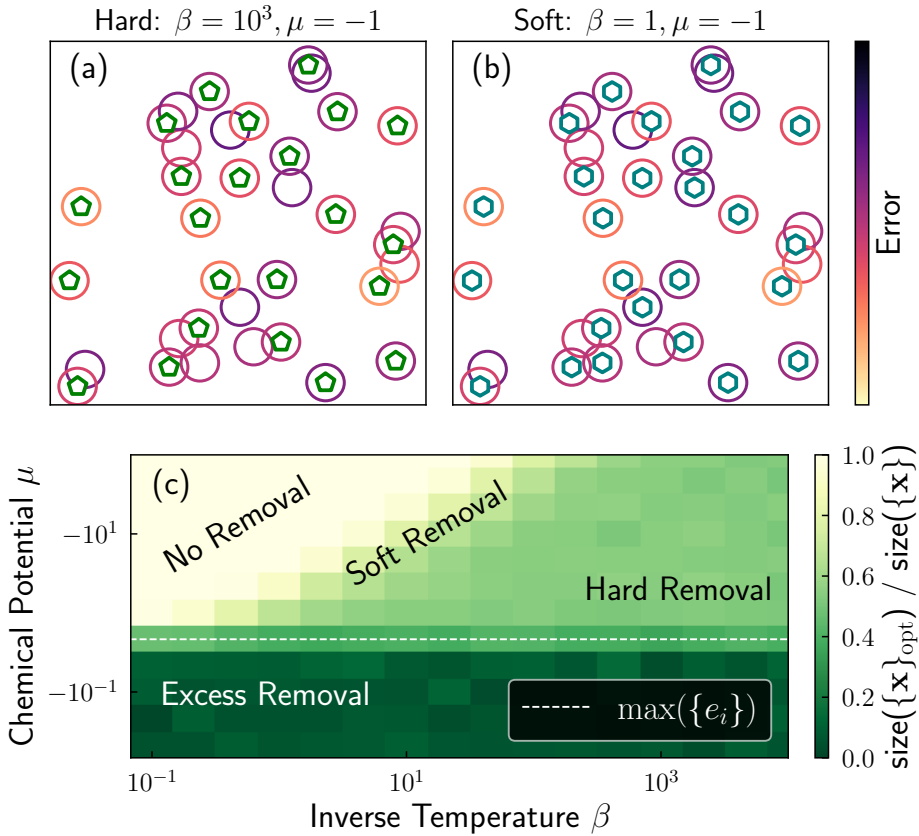


**Figure 5.2:** The removal of overlapping particles following equation 5.3. The circles represent particles ( $\{\mathbf{x}\}$ ). The colour of the circles represent their errors. (a): the result with parameters  $\beta = 10^3$  and  $\mu = -1$ . The pentagons represent the optimised result ( $\{\mathbf{x}\}_{\text{opt}}$ ). The result is identical to that in Fig. 5.1. (b): the result with parameters  $\beta = 1$  and  $\mu = -1$ . The pentagons represent the optimised result ( $\{\mathbf{x}\}_{\text{opt}}$ ). (c): the ratio between the number of particles after and before the optimisation, as a function of the two parameters. The  $x$  axis corresponds to the inverse temperature  $\beta$ , and the  $y$  axis corresponds to the chemical potential  $\mu$ . Different regions were labelled with their characteristic behaviour. The dashed line shows the maximum value of the error. Each grid in (c) represents the average of 25 ideal-gas simulations.

as a promising algorithm for the real-space colloidal microscopy, as the energy term can take realistic, inter-colloidal interaction form, to match the experimental system.

### 5.3 From Better Locations to Trajectories

The overlap-free positions can be linked into trajectories, from which we can get the velocities of the fish. The term “link” means finding the fish  $j$  at time  $t+1$ , which corresponds to the fish  $i$  at time  $t$ , and the pair  $(i, j)$  forms a link. Such a linking process therefore gives us the identity of each fish in different time points. The movement of a single fish, as a function of time, forms a *trajectory*. The process of linking coordinates into trajectories is commonly applied in different fields, for instance in the analysis of colloidal experiments[212] as well as fluid dynamic experiments[108].

Two examples of the linking process are illustrated in Fig. 5.3, where the locations of 6 simulated fish in 3 successive frames were linked into 6 trajectories. The good links were illustrated in Fig. 5.3(a) while the poor links were shown in Fig. 5.3(b). Visually, the trajectories in (b) were poor because the resulting trajectories contain sudden jumps between different locations. Intuitively, we would not expect the fish to jump back and forth from place to place.

The method of linking experimental coordinates of animals into trajectories always involves some “educated guesses”. This is because we do not know the underline dynamics of the animals that we were studying, as we

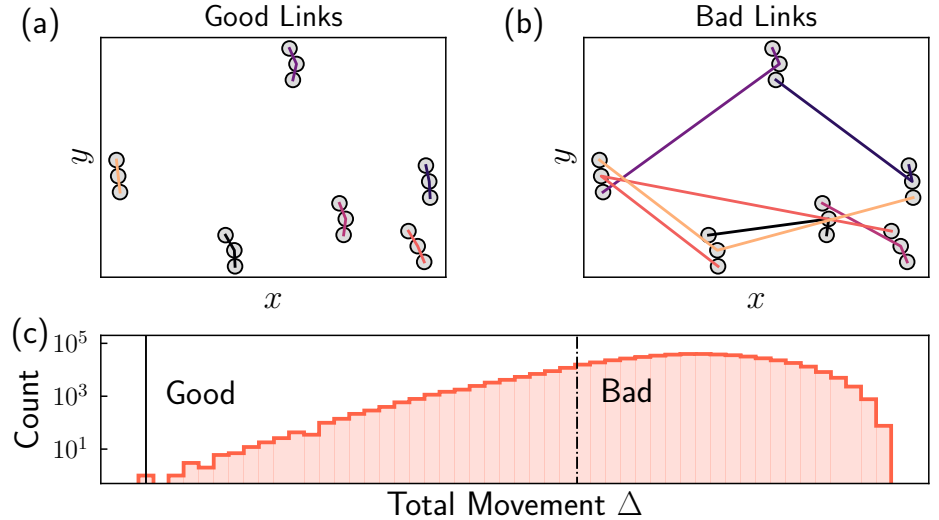


**Figure 5.3:** (a): the good way to link positions in 3 successive frames into trajectories. (b): the bad way to link positions in 3 successive frames into trajectories. (c): The distribution of total movement ( $\Delta$ ) for all the possible linking options ( $6!^2 = 518,400$  possibilities). The good linking result corresponds to the links that yields the minimum of  $\Delta$ .

could not predict precisely where the animal will move to from its past trajectory. In this section, two heuristic methods that “worked” will be introduced.

### 5.3.1 Equilibrium Linking

With the observation in Fig. 5.3, it is reasonable to assume that the links yielding smallest total movement for all the fish, are good links. Formally, our linking procedure will aim at minimising the total squared movement  $\Delta$ , which is written as

$$\Delta = \sum_i \sum_t \delta_i(t)^2,$$

where  $i$  corresponds to all the linked trajectories, and  $\delta_i(t)$  is the distance that a fish travelled between time  $t - 1$  and  $t$ . In fact, Crocker and Grier showed that the minimisation of  $\Delta$  is equivalent to maximising the probability, if the fish were non-interacting diffusive Brownian particles in equilibrium [212]. Even though the underlying assumption is crude, this method produces visually good trajectories for fish. The linking algorithm that minimises  $\Delta$  is termed as *equilibrium linking*, since it is suitable for physical systems in equilibrium.

Unfortunately, the minimisation of  $\Delta$  is a difficult task. Naively, we may attempt to list all the possible links, and choose the one with minimum  $\Delta$  value as our linking result. However, the complexity of this approach is  $\mathcal{O}((N!)^{T-1})$  [212], where  $N$  is the number of fish, and  $T$  is the total number of time points. For the experiment with 10 fish in 20 total frames, we need to enumerate  $\sim 10^{130}$  possible combinations, which is not practical.<sup>45</sup>

To reduce the complexity, we restrain the particles to have a maximum movement between two frames [212], and analyse the data frame-by-frame, rather than optimise the entire trajectory. A good implementation of this approach is available in the `Trackpy` package [213]. Unavoidably, the introduction of extra assumptions will deviate the obtained solution, the linked trajectories, away from the true global minimum of  $\Delta$ . And even with the

<sup>45</sup> To find the minimum number in an array with size of  $10^{130}$ , we need  $\sim 10^{103}$  years, using a laptop with infinite memory. People die in the timescale of  $\sim 10^2$  years.

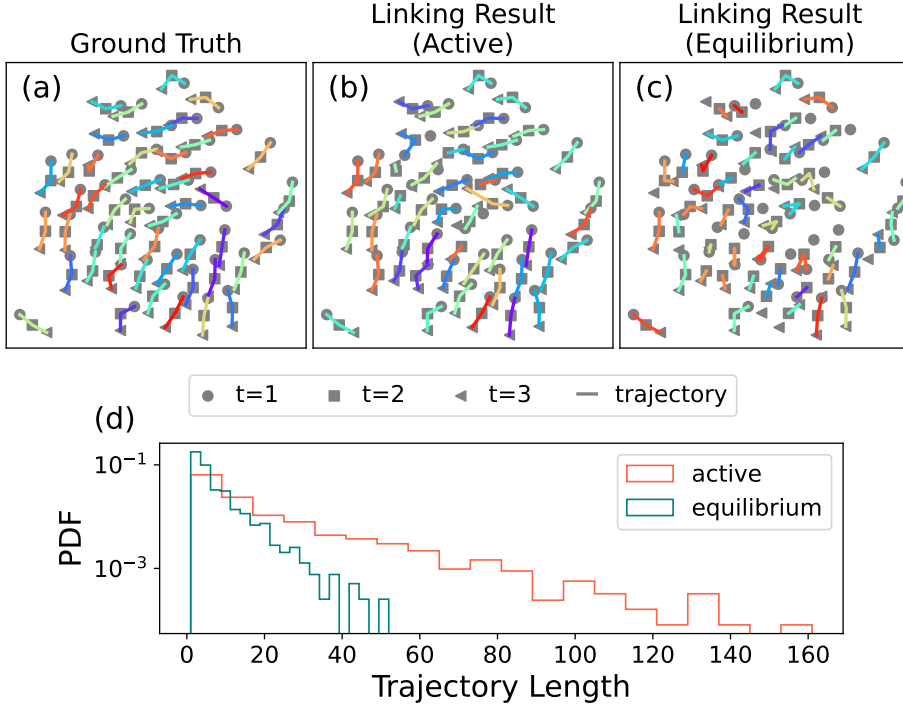


**Figure 5.4:** The linking process to get trajectories from positions. The grey solid scatters represents the location ( $\{\mathbf{x}\}$ ) of simulated particles. The coloured lines represent the linked trajectories. Some positions were discarded (rendered as empty scatters) randomly to mimic the experimental locations. (a) The ground truth. (b) The result with the active linking algorithm. (c) the result with the equilibrium linking algorithm. (d) The distribution of trajectory length values for different linking algorithms. Better algorithms are expected to produce longer trajectories.

reduced complexity, the equilibrium linking algorithm can be extremely slow, when multiple equally good linking options being available.

### 5.3.2 Active Linking

For systems that are out of equilibrium, like a school of fish, the assumption introduced in section 5.3.1 is not formally correct. In this project, another good heuristic approach proposed by Ouellette et al. was used to link the coordinates [108]. For particle  $i$  at time  $t$  and particle  $j$  at time  $t+1$ , the link  $(i, j)$  was established by minimising the *tracking cost*,

$$\phi_{ij}^t = \left\| \mathbf{x}_j^{t+2} - \hat{\mathbf{x}}_i^{t+2} \right\|,$$

where  $\mathbf{x}_j^{t+2}$  is the location of particle  $j$  in time point  $t+2$ , and  $\hat{\mathbf{x}}_i^{t+2}$  is the predicted location of particle  $i$  in time point  $t+2$ . The prediction was calculated with the following

$$\begin{aligned} \hat{\mathbf{x}}_i^{t+2} &= \mathbf{x}_i^t + \mathbf{v}_i^t + 2\mathbf{a}_i^t = 3\mathbf{x}_i^{t+1} - 3\mathbf{x}_i^t + \mathbf{x}_i^{t-1} \\ \mathbf{v}_i^t &= (\mathbf{x}_i^{t+1} - \mathbf{x}_i^{t-1})/2 \\ \mathbf{a}_i^t &= \mathbf{x}_i^{t+1} - 2\mathbf{x}_i^t + \mathbf{x}_i^{t-1}. \end{aligned}$$

In reference [108] this method was named as the four frame best estimate method. Operationally, for particle  $i$  in time point  $t$ , we search for all the possible particle  $j$  in time point  $t+1$ , and establish link with the minimum  $\phi_{ij}^t$ , by predicting the location of the trajectory with link  $(i, j)$  in time point  $t+2$ . This linking method is noted as the *active* linking method.

The behaviour of the two linking methods was exhibited in Fig. 5.4, where simulated trajectories were used for the test. The model used in the simulation is the inertial Vicsek model, which will be introduced in

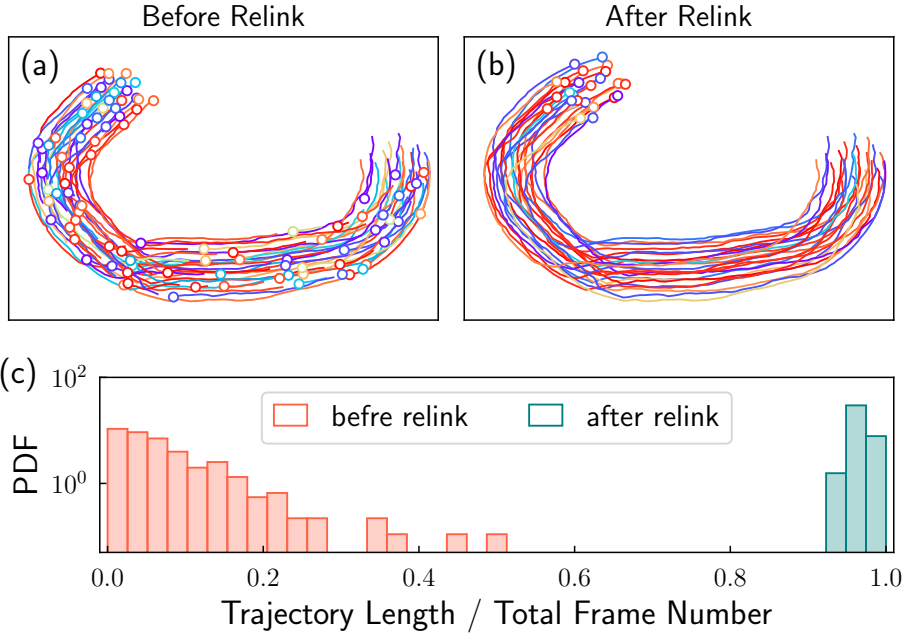


**Figure 5.5:** The effect of relinking process with simulated data. (a) The trajectories linked with the active linking method. (b) The trajectories extended with the relinking method. (c) The distribution of the trajectory length. The length values were rescaled by the total frame number. The trajectory with length value being close to 1 corresponds to a full trajectory through out the entire simulation.

chapter 6. The model generates trajectories that are similar to that of the zebrafish, and the generated coordinates were used to test the different linking algorithm. Both methods generated visually good trajectories. However, the equilibrium linking method obtain shorter trajectories, as shown in Fig. 5.4, which indicates that the behaviour of the equilibrium linking method is poor. For all the fish data, the active linking method was used.

### 5.3.3 Extending the Trajectories

The linking algorithms typically give us some short trajectory segments. These segments can be extended further following Xu's method. The idea is to join the two trajectories together, if the prediction from earlier trajectory matched the locations of the later trajectory [109].

The result of the relinking method is illustrated in Fig. 5.5. The coordinates to be linked and relinked was generated from simulation, where 25 simulated agents were performing a U-turn together. Some of the coordinates (2%) were deliberately removed during linking, in order to mimic the various locating errors in reality.

For perfect coordinates, the active linking method was capable of obtaining correct trajectories. However, the introduction of missing particles makes this linking process problematic. As illustrated in Fig. 5.5(a), many short trajectory segments were obtained. The relinking process successfully re-joined these segments into very long trajectories, as shown in Fig. 5.5(b). The relinked trajectories were very long, and half of them have the full length, as shown in Fig. 5.5(c). For the experimental fish coordinates, the relinking process is valuable, as it always extends the short trajectories (from the active linking method) into longer ones.

## 5.4 From Trajectories to Behaviour

The trajectories contain rich information about the behaviour of the zebrafish. The analysis to reveal the behaviour of the fish will be discussed in this section. For the structure of the fish group, we introduce the nearest neighbour distance, the convex hull, and the radial distribution function, as different characterisation tools. On the other hand, the average speed, the orientational relaxation time, the polarisation order and the persistence length will be discussed as the quantities to describe the dynamics of the fish.

### 5.4.1 The Structure

The coordinates of the fish shed light on the the *structure* of the group, giving answers to the following questions.

1. How close do a pair of fish stay to each other?
2. How big is the animal group in terms of the metric size?
3. Are the fish arranged in an ordered way (like atoms in a crystal) or a disordered way (like atoms in a fluid phase)?

To answer the first question, we can calculate the nearest neighbour distance of the fish, whose usage could be traced back to 1960s [100]. The average nearest neighbour distance of fish ( $\bar{l}_{\text{nn}}$ ) is defined as,

$$\bar{l}_{\text{nn}} = \frac{1}{N} \sum_i \min_{j(\neq i)} (d_{ij}) \quad (5.4)$$

where  $d_{ij}$  is the pairwise distance of fish  $i$  and  $j$ , and  $N$  is the total amount of fish. The average nearest neighbour distance of a group could serve as a measure of the cohesiveness of the fish. The group with smaller  $\bar{l}_{\text{nn}}$  value appear more cohesive.

To measure the size of the group, we can measure area (for 2D data) or the volume (for 3D data) of the *convex hull*, constructed from the coordinates of the fish. The convex hull is the smallest subset of the space, which contains all line segments connected by all pairs of points [214]. Intuitively, the convex hull is the smallest polygon (or polyhedron for 3D coordinates) that encloses all coordinates. An example of the convex hull constructed from 50 fish were provided in Fig. 5.7(a). The area ( $A_{\text{ch}}$ ) or the volume ( $V_{\text{ch}}$ ) of the hull can be transformed into a lengthscale<sup>46</sup>, termed as the *effective convex hull diameter*  $\bar{l}_{\text{ch}}$ , which is defined as

$$\begin{aligned} \bar{l}_{\text{ch}} &= \left( \frac{4}{\pi} A_{\text{ch}} \right)^{\frac{1}{2}} \text{ (2D Coordinates)} \\ &= \left( \frac{6}{\pi} V_{\text{ch}} \right)^{\frac{1}{3}} \text{ (3D Coordinates),} \end{aligned} \quad (5.5)$$

where the shape of the convex hull were assumed to be circular (for 2D coordinates) or spherical (for 3D coordinates). The effective convex hull diameter is a measure of the group size.

<sup>46</sup> To describe the completely geometry of the group, we need to consider more details, since a group of fish does not always present the shape of a sphere. These extra details include the aspect ratio, or the thickness. By assuming the group shape to be spherical, we can use just one number to describe it. Such simplified description can be thought of as a first order approximation.

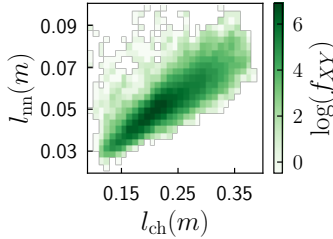


Figure 5.6: The joint probability density function ( $f_{XY}$ ) of  $l_{nn}$  and  $l_{ch}$ . The results were obtained from 3D experimental data of 50 adult zebrafish.

Both lengthscales, the effective convex hull diameter and the nearest neighbour distance, capture the cohesiveness of the group. In fact, they were often linearly correlated for the zebrafish, as shown in Fig. 5.6. Therefore, we only need one of them to describe the fish behaviour. The nearest neighbour distance was selected, because it is more widely used in the past.

Finally, we can calculate the radial distribution function (the  $g(r)$ ) of the fish to inspect whether the structure of the fish was ordered or not. However, the spatial distribution of a group of fish may not be homogeneous in the experiment, possibly being affected by environmental factors such as the distribution of brightness, as shown in the results in chapters 3 and 4. Therefore, the pairwise distances ( $\{d_{ij}\}$ ) would be biased to favour the lengthscales of the high density region. In other words, the fish appear to swim together. But they were driven by an external field, instead of being attractive to each other.

To remedy the effect of the external field, we can compare the pairwise distances of the fish  $\{d_{ij}\}_{\text{fish}}$  to the pairwise distances of the ideal gas particles  $\{d_{ij}\}_{\text{gas}}$ , that share the same inhomogeneous spatial distribution with the fish. Operationally, we calculate the density distribution of the fish, and sample ideal gas particles drawn randomly from the same density distribution, using the tower-sampling method [42]. Therefore, the sampling of the ideal gas particles is biased, in contrast to a uniform distribution in the boundary. The biased sampling result was illustrated in Fig. 5.7(a) and Fig. 5.10(a), where the distribution of the ideal gas is identical to that of the fish.

Even though the biased ideal gas particles share the same density distribution with the fish, these two systems are inherently different. The ideal gas particles do not interact with each other, but the fish do. Such a difference will lead to different pairwise distances, whose probability density function was noted as  $f_d(r)$ . For instance, we can not imagine two fish with a separation of zero, as the fish can not physically overlap. Such a repulsive interaction will decrease the likelihood of finding two fish at very short distances.

The ratio between the  $f_d(r)$  from the fish and the ideal gas, was defined as the radial distribution function,  $g(r)$ :

$$g(r) = \frac{f_d^{\text{fish}}(r)}{f_d^{\text{gas}}(r)}. \quad (5.6)$$

The value of  $g(r)$  indicates the likelihood of finding a pair of fish at the distance  $r$ , with respect to the ideal gas particles. When  $g(r)$  is equal to one, it is equally likely to find a pair of fish or to find a pair of ideal gas particles, indicating the lack of correlation. When the value of  $g(r)$  is greater than one, the density of the fish correlates positively, suggesting a cohesive behaviour.

For the structure of dilute liquid, we often get a peak in the  $g(r)$ , followed by a monotonic decay. The location of the peak is often close the  $l_{nn}$ . The subsequent decay revealed another lengthscale, which was termed the correlation length of the density ( $\xi_\rho$ ). The definition of  $\xi_\rho$  is

$$g(\xi_\rho) = 1; (\xi_\rho > l_{nn}). \quad (5.7)$$

Symbol	Definition	Value (2D)	Value (3D)	Meaning
$l_{nn}$	Eq. 5.4	$61 \pm 10$ mm	$51 \pm 10$ mm	Nearest Neighbour Distance
$l_{ch}$	Eq. 5.5	$0.8 \pm 0.46$ m	$0.29 \pm 0.25$ m	Convex Hull Diameter
$l_p$	Eq. 5.13	$\sim 0.13$ m	$\sim 0.14$ m	Persistence Length
$\xi_\rho$	Eq. 5.7	$\sim 0.4$ m	$\sim 0.32$ m	Correlation Length of the Density
$\xi_v$	Eq. 5.15	$\sim 0.15$ m	$\sim 0.12$ m	Correlation Length of the Speed
$\xi_o$	Eq. 5.15	$\sim 0.38$ m	$\sim 0.24$ m	Correlation Length of the Orientation
$\tau_o$	Eq. 5.12	$\sim 1.3$ s	$\sim 0.9$ s	Relaxation Time of the Orientation
$\tau_\rho$	Eq. 5.12	$\sim 900$ s	$\sim 180$ s	Relaxation Time of the Density

Table 5.1: Different Length Scales and Time Scales for 50 Zebrafish.

and we force the value of  $\xi_\rho$  to be greater than  $l_{nn}$ , effectively removing the situation where  $g(r)$  reaches zero at very small distance values.

In addition to the lengthscales, the height of the peak of  $g(r)$  give us a measure of the cohesiveness of the group. Inspired by liquid state theory, we define the logarithm of the peak value of  $g(r)$  as the *effective attraction*  $\epsilon$  [128]:

$$\epsilon = -\log(\max(g(r))). \quad (5.8)$$

The quantity  $\epsilon$  is a better measure of the cohesion of the fish, because it could differentiate whether the fish is cohesive or not. For a non-cohesive group, the value of the  $g(r)$  will be close to one, leading a value of 0 for  $\epsilon$ . The lack of cohesion could be identified by the lengthscales.

#### 5.4.2 The Dynamics

The velocities can be calculated as the time derivative of the positions along the trajectories, once we linked the coordinates. The velocities offered the *dynamics* of the system, giving answers to the following questions.

1. How fast do the fish swim?
2. Is the movement of the fish ordered or random?
3. How long does it take for the fish group to forget its current state?

To answer the first question, we could simple calculate the average speed of the fish, which is defined as,

$$v = \frac{1}{N} \sum_i \|\mathbf{v}_i\|, \quad (5.9)$$

where the  $\mathbf{v}_i$  is the location of fish  $i$ , and  $N$  is the total amount of the fish. With higher  $v$  value, the animals on average move faster. The distribution of the average speed of 50 zebrafish in 3D was shown in Fig. 5.11(a).

Being conceptually similar to the average speed, the speed of the entire group can be calculated as,

$$v_g = \frac{1}{N} \left\| \sum_i \mathbf{v}_i \right\|.$$

This quantity indicates the speed of the group centre. A large group speed value indicates the fish moving collectively from one place to another. Formally, we define an *order parameter* to describe such behaviour, by modifying the group speed:

$$\Phi = \frac{1}{N} \left\| \sum_i \mathbf{o}_i \right\| = \frac{1}{N} \left\| \sum_i \frac{\mathbf{v}_i}{\|\mathbf{v}_i\|} \right\|, \quad (5.10)$$

<sup>47</sup> The polarisation is conceptually similar to the magnetisation per spin in the Ising model. When the order parameter approaches one, the system is ordered. The polarisation is identical to the magnetisation defined in XY model (in 2D) and Heisenberg model (in 3D), when the orientations of the fish was treated as the spin vectors [209].

where  $\Phi$  is called the *polarisation*<sup>47</sup>, and  $\mathbf{o}_i$  is the orientation of fish  $i$ . The definition of  $\Phi$  ensures it varies from 0 to 1, like other order parameters in statistical mechanics. The movement of a group of fish is ordered if the value of  $\Phi \sim 1$ , and the movement being disordered when  $\Phi \sim 0$ .

For a group of fish, their structural quantities ( $l_{nn}, l_{ch}, g(r)$ ) and their dynamic quantities ( $v, \Phi$ ) change constantly. With the *time-displaced autocorrelation function* (ACF) of these quantities, we can probe the typical timescale for the fluctuation of these quantities. The ACF of quantity  $C_A(t)$  is defined as, [209]

$$C_A(t) = \int d\tau (\mathcal{A}(\tau) - \bar{\mathcal{A}}) (\mathcal{A}(\tau + t) - \bar{\mathcal{A}}) = \langle \mathcal{A}(t) \mathcal{A}(t + \tau) \rangle. \quad (5.11)$$

where  $\bar{\mathcal{A}}$  is the time-average  $\mathcal{A}$ . For the ACF of the orientation of the fish, the shape of  $C_o(t)$  exhibits a typical exponential decay. Such ACF was commonly obtained from the Markov processes, where the  $C_A(t)$  could be written as a sum of exponential functions,

$$C_A(t) = \sum_i (a_i \exp -t/\tau_i) \sim \exp (-t/\tau). \quad (5.12)$$

<sup>48</sup> This timescale corresponds to the second largest eigenvector of the transition matrix of the Markov process.

Here the shape of  $C_A$  is often dominated by the largest time scale ( $\tau$ ).<sup>48</sup> Therefore, we define the timescale when  $C_o$  reaches  $1/e$  as the relaxation time orientation, noted as  $\tau_o$ . For other quantities, the shapes of their corresponding  $C_A(t)$  functions are complicated. We therefore define the time when their corresponding  $C_A(t)$  reach zero as their relaxation time scales.

Regardless of the slightly different definition, the value of the relaxation time  $\tau_A$  indicates the time taken for a system to forget its current state. For instance, the value of  $\tau_{nn}$  is the time for a group fish to forget their nearest neighbour distance. Because the two density-related quantities,  $l_{nn}$  and  $l_{ch}$ , are strongly correlated, their corresponding ACFs ( $C_{nn}(t)$  and  $C_{ch}(t)$ ) are also very similar. Therefore, we term their relaxation time as the relaxation time of density, written as  $\tau_\rho$ . The examples of relaxation time scales for the orientation and density are available in Table 5.1. Practically, these two time scales are the only dominating time scales for the fish, in all of our observations.

In addition to the timescale of the structural quantities, we could also calculate the lengthscale of the dynamical quantities. For instance, we can

take the product of the average speed  $v$  (Eq. 5.9) and the orientation relaxation time  $\tau_o$  (Eq. 5.12), as the *persistence length*:

$$l_p = v \tau_o. \quad (5.13)$$

The value of  $l_p$  corresponds to the distance that a fish travels in a straight fashion. For the fish with a small  $l_p$  value, its trajectory appear more curvy.

In addition to the persistence length, we can also measure the correlation length of the dynamics of the fish. If a fish changed its speed at a certain time point, it is interesting to know how far would such change reach. To do so, we calculate the *connected correlation function* of the dynamical quantities [148, 209]<sup>49</sup>:

$$\begin{aligned} C_{\mathcal{A}}(r) &= \iint d\mathbf{r} d\mathbf{r}' (\mathcal{A}(\mathbf{r}) - \bar{\mathcal{A}})(\mathcal{A}(\mathbf{r} + \mathbf{r}') - \bar{\mathcal{A}}) \delta(\|\mathbf{r} - \mathbf{r}'\| - r) \\ &= \frac{\sum_i \sum_{j \neq i} [(\mathcal{A}_i - \bar{\mathcal{A}})(\mathcal{A}_j - \bar{\mathcal{A}})\delta(r - r_{ij})]}{\sum_i \sum_{j \neq i} \delta(r - r_{ij})} \end{aligned} \quad (5.14)$$

where  $\delta(r - r_{ij}) = 1$  when  $r = r_{ij}$ , and it equals zeros otherwise. The correlation functions often exhibits a monotonic decay when  $r > l_{nn}$ . We define the length when the correlation function  $C_{\mathcal{A}}(r)$  reaches zero as the *correlation length* of  $\mathcal{A}$ :

$$C_{\mathcal{A}}(\xi_{\mathcal{A}}) = 0. \quad (5.15)$$

The examples of the correlation functions for the speed  $C_v(r)$  and for the orientation  $C_o(r)$  were shown in Fig. 5.8(e) and Fig. 5.11(e).

## 5.5 The Behaviour of 50 Zebrafish in 2D

The coordinates of 50 zebrafish in a quasi-2D experiment, obtained with the methods introduced in chapter 3, were linked into trajectories, from which the behaviour of these fish were analysed. The result for such experiment will be introduced in this section.

### 5.5.1 The Structure

The structure of 50 zebrafish was shown in Fig. 5.7. The spatial distribution was presented in Fig. 5.7(a), which was used to sample the biased ideal gas particles. The distribution of the pairwise distance,  $f_d(r)$ , was presented in Fig. 5.7(b). It is obvious the fish were more cohesive than the ideal gas particles, indicated by the mode of the distribution of the pairwise distances. The ratio of these distributions gives the  $g(r)$  of the fish (Eq. 5.6), which is shown in Fig 5.7 (c). The distribution of  $l_{nn}$  and  $l_{ch}$  are presented in Fig 5.7 (d).

The important structural feature revealed in Fig 5.7 is the separation of  $\xi_{\rho}$  and  $l_{ch}$ , as the effective convex hull diameter ( $l_{ch}$ , Eq. 5.5) is much larger than the correlation length of the density ( $\xi_{\rho}$ , Eq. 5.7). This corresponds to the fragmentation of the fish group, where the 50 fish separated into

<sup>49</sup> The correlation function  $C_{\mathcal{A}}(r)$  with variable “ $r$ ” is a spatial correlation function, which gives us a correlation length  $\xi_{\mathcal{A}}$ . The correlation function  $C_{\mathcal{A}}(t)$  with variable “ $t$ ” is a temporal correlation function, which gives us a relaxation time  $\tau_{\mathcal{A}}$ .

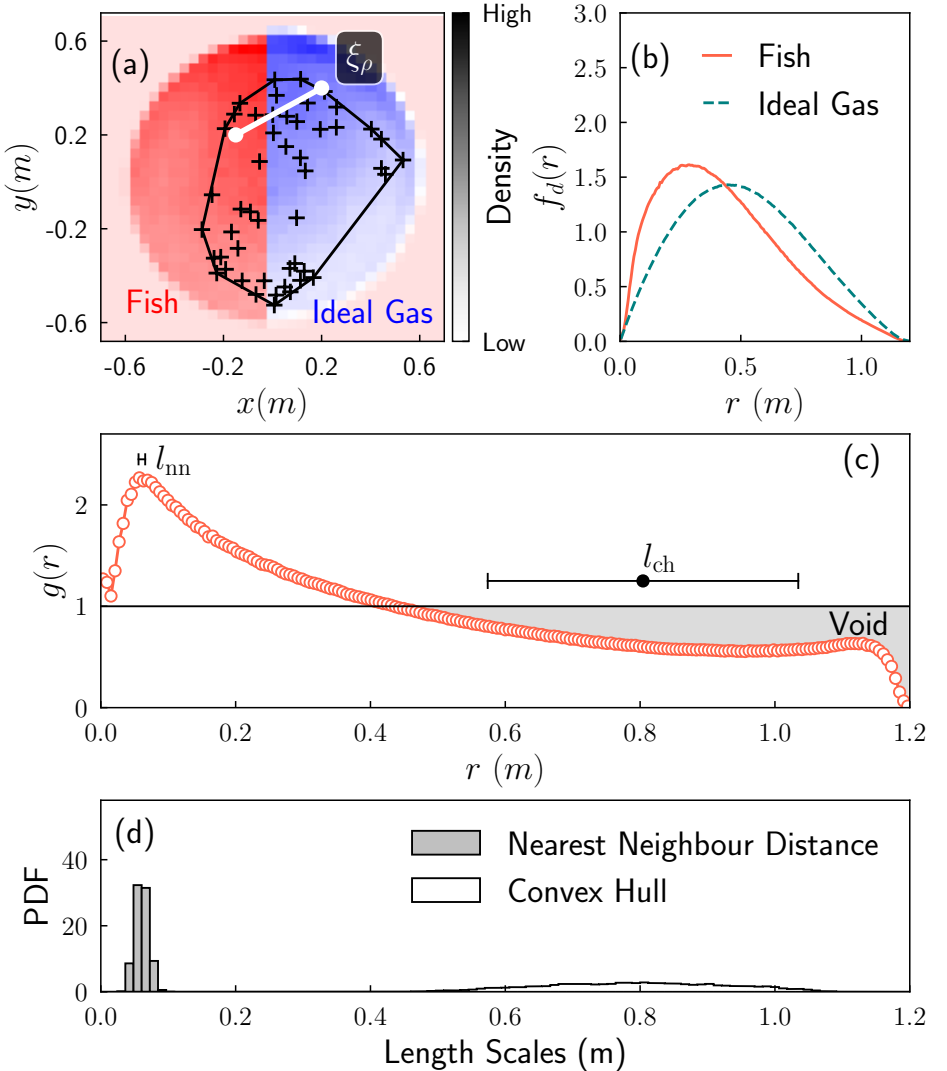


**Figure 5.7:** The structure of 50 zebrafish in a quasi-2D experiment. (a) The joint distribution of the  $x$  and  $y$  coordinates of the fish and the ideal gas particles. The distribution of the ideal gas were biased to be identical to the fish. The location of 50 fish at one time point were plotted as circles. The boundary convex hull of these 50 scatters were plotted as solid lines. (b) The probability density function of the pairwise distributions for the fish and the ideal gas particles in 2D. (c) The radial distribution function,  $g(r)$  (Eq. 5.6) of the fish. It is defined as the ratio between the two PDFs in (b). Two important length scales, the nearest neighbour distance and the size of the convex hull were captured by the  $g(r)$ . The long distance region where  $g(r) < 1$  corresponds to the void in the tank, where the group were able to explore. (d) The distribution of the nearest neighbour distance and the effective diameter of the convex hull, of the fish.

sub-clusters. This scenario was plotted in Fig. 5.7(a), where the locations of the fish were represented as cross markers. There are clearly two dense blobs within the convex hull. And the size of these dense blobs is accurately captured by  $\xi_\rho$ .

As a consequence of the monotonic decay in  $g(r)$ , the fish group present a void at larger separation distances, where the value of  $g(r) < 1$ , shown in Fig. 5.7(a). As a result of the fragmentation of the fish group, the void also appear inside the fish group. The fragmentation of the fish group could explain the very wide distribution of  $l_{ch}$  observed in Fig. 5.7(d). If two sub-groups meet, the entire group will have a small value for its  $l_{ch}$ . If the sub-groups were separated, the fish will exhibit a large  $l_{ch}$  value.

### 5.5.2 The Dynamics

The dynamics of the 50 fish are shown in Fig. 5.8. Figure 5.8 (a) - (c) shows the distribution of the polarisation  $\Phi$  (Eq. 5.10) and the average speed  $v$  (Eq. 5.9). Their joint distribution appear to be very weakly correlated, as exhibited in Fig. 5.8(b). Overall, the fish were in a random state where

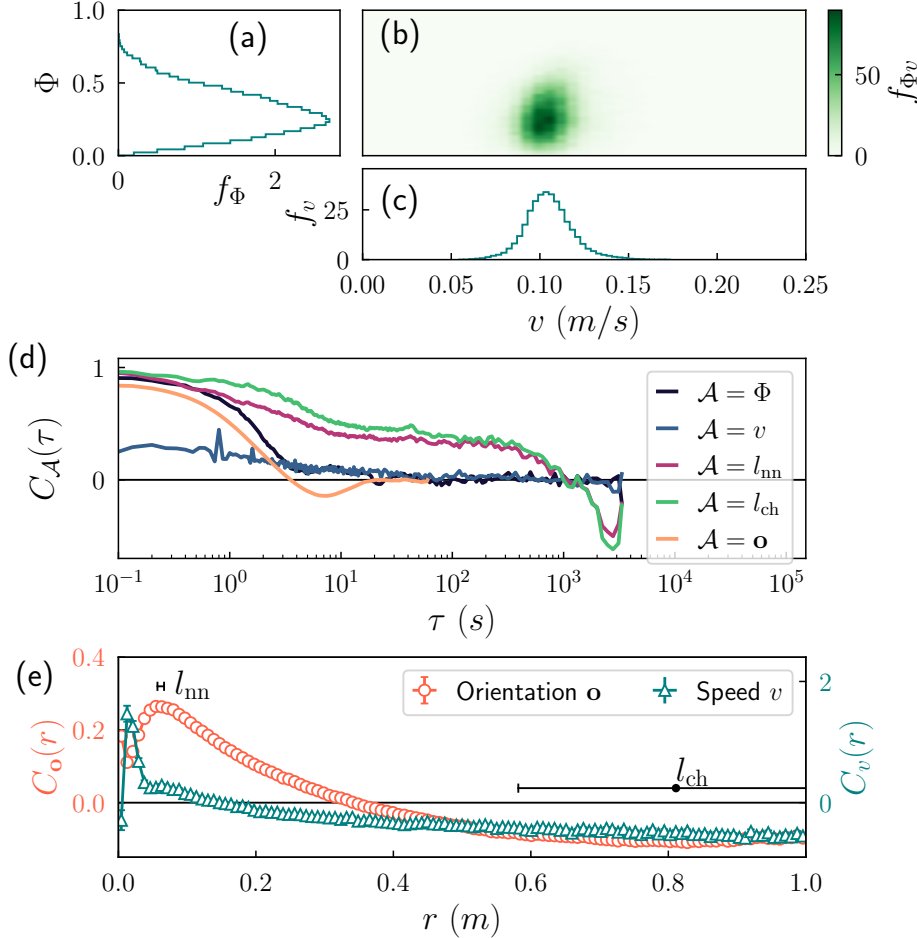


**Figure 5.8:** The dynamics of 50 adult zebrafish in 2D. (a) The probability density function ( $f_\Phi$ ) of the polarisation ( $\Phi$ , Eq. 5.10). (b) The joint probability density function ( $f_{\Phi v}$ ) for the polarisation ( $\Phi$ ) and the speed ( $v$ ). (c) The probability density function ( $f_v$ ) of the average speed (Eq. 5.9). (d) The auto-correlation function,  $C_A(\tau)$ , of the polarisation ( $\Phi$ ), the average speed ( $v$ ), the nearest neighbour distance ( $l_{nn}$ ), the effective convex hull diameter ( $l_{ch}$ ), and the orientation of each fish ( $o$ ). (e) The connected correlation function of the orientation ( $o$ ) and speed ( $v$ ), as a function of pairwise distances.

$$\Phi \sim 0.25.$$

The ACFs (Eq. 5.11) of different quantities were shown in Fig. 5.8(d). Two well separated time scales could be identified from these functions. For the time scale of  $\sim 1$ s, the fish changed its orientation, and the value of  $C_o(t)$  decays to  $1/e$ . This timescale also dominates the ACF of the polarisation ( $C_\Phi(t)$ ).

One possible explanation for this observation, is to assign an intrinsic orientational diffusion constant for the fish. In other words, we assume the fish will sporadically change its swimming direction every now and then. And these random changes make the fish forget its original orientation, in the timescale of one second. Since the orientational diffusion is an inherent property of the fish, it would affect the collective order ( $\Phi$ ) of a fish group.

On the other hand, the relaxation of the local density, as probed by the ACFs of  $l_{nn}$  and  $l_{ch}$ , is a much slower process. The two ACFs have two similar relaxation timescales of 900s (15 minutes). This process might correspond to the fragmentation of the group. As a result, we use this largest timescale ( $\tau_\rho \sim 900$ s) to characterise the time it took for 50 zebrafish to forget their state, in a quasi-2D experiment.

The connected correlation function of the fish, for their speed as well as their orientation was plotted in Fig. 5.8(e). Surprisingly, the correlation function of the orientation,  $C_o(r)$ , exhibits a much longer correlation length ( $\xi_o \sim 0.38$ m), compared to the correlation of the speed ( $\xi_v \sim 0.15$ m). This

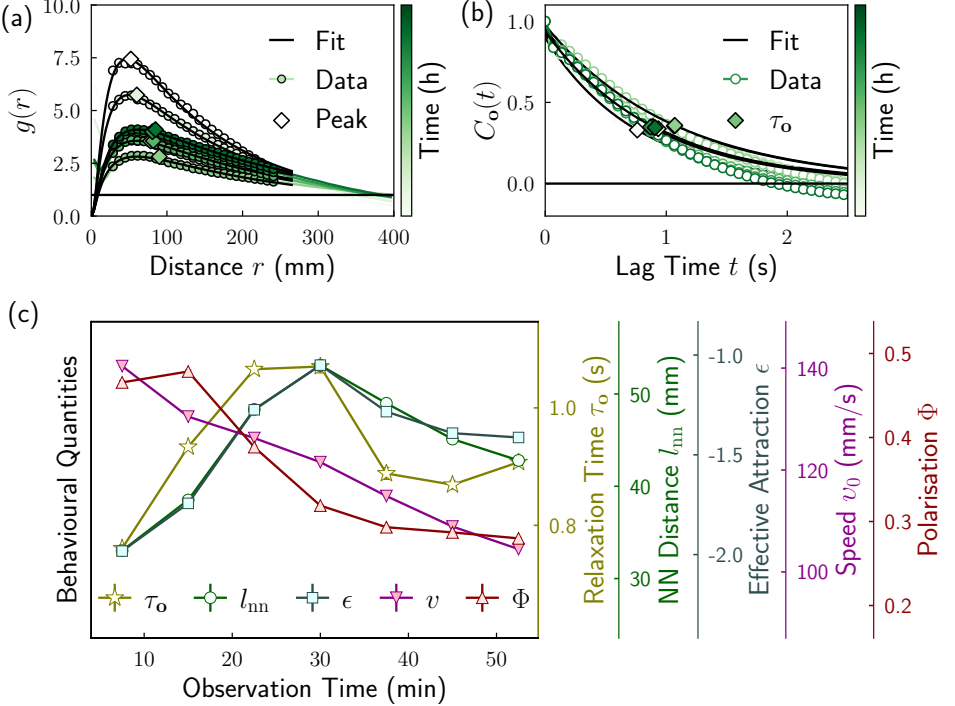


**Figure 5.9:** (a) Sequence of radial distribution functions, the  $g(r)$ , at different time points. In early times (top curves) the fish are clustered together so that the peak is large; at later times (bottom curves) the local density decreases and so does the peak height. (b) Sequence of the auto-correlation function of the orientations  $C_o(t)$  of the fish, at different time points. (c) The time evolution of the averaged behavioural quantities for 50 young fish. Each point corresponds to the average value in 15 minutes. The error bars illustrate the standard error values.

picture is very different from European starlings, whose correlations lengths for both orientation and speed were similar [67]. Our result suggests the lack of speed synchronisation for the zebrafish, which could be the reason that the fish were always in a randomised state with a low  $\Phi$  value.

### 5.5.3 The Changing States

Since the fish change their (macroscopic) states in a timescale of 15 minutes, we segment the trajectory into different sections with the duration of 15 minutes. By doing so, we could study the structure and dynamics of the fish as a function of time, since the fish could change their states continuously, rather than being in a steady state.

The changing states of the fish as a function of observation time as plotted in Fig. 5.9. The  $g(r)$  of the fish were shown in Fig. 5.9(a), where the peak of the  $g(r)$  gradually decreases with the evolution of time. This suggests a decrease of cohesiveness for the fish group. The ACF of the orientation of the fish,  $C_o(t)$ , at different time were plotted in Fig. 5.9(b), which exhibit less variation comparing with the  $g(r)$  functions.

The time evolution of 5 selected behavioural quantities, the orientational relaxation time ( $\tau_o$ , Eq. 5.12), the nearest neighbour distance ( $l_{nn}$ , Eq. 5.4), the effective attraction ( $\epsilon$ , Eq. 5.8), the average speed ( $v$ , Eq. 5.9), and the polarisation ( $\Phi$ , Eq. 5.10), was plotted in Fig. 5.9(c). Each point in Fig. 5.9(c) corresponds to the time average over 15 minutes. It is clear that the structural quantities ( $\epsilon$  and  $l_{nn}$ ) were correlated while the dynamical quantities ( $v$  and  $\Phi$ ) were correlated.

Surprisingly, the orientational relaxation time seems to correlate with the structural quantities, and the fish exhibit slower orientation relaxation when they were in a less cohesive state. One possible explanation is that

the orientation of the fish will be interrupted by a close neighbour, as a consequence of the avoidance for collision. These extra interruptions, on top of the intrinsic orientational diffusion of the fish, make the fish change their orientations faster in a dense group. This picture is also consistence with the observation that the polarisation of the fish increase as the nearest neighbour distances of the fish increase [215].

## 5.6 The Behaviour of 50 Zebrafish in 3D

Following the same data processing procedure and analysis, we also studied the behaviour of 50 zebrafish in a 3D observation. In contrast to the 2D experiments where the fish were confined in a shallow water environment, now the fish can explore a 3D space enclosed by the water-air interface and a bowl-shaped tank. The result for one representative 3D experiment will be introduced in this section, while multiple experiments have been repeatedly carried out. The other experimental results will be discussed in section 5.7.

### 5.6.1 The Structure

The spatial distribution of 50 zebrafish was shown in Fig. 5.10 (a), where the joint distribution of the  $x$  and  $z$  coordinate clearly shows the depth preference of the fish, as discussed in section 4.3.4. With the ideal gas sampled according to the distribution of the fish, we calculated the PDF of the pairwise distances,  $f_d(r)$ , of the fish and the ideal gas. The result is shown in Fig 5.10(b). It is clear that the fish are more cohesive, as the mode of  $f_d^{\text{fish}}(r)$  locates at a smaller distance value.

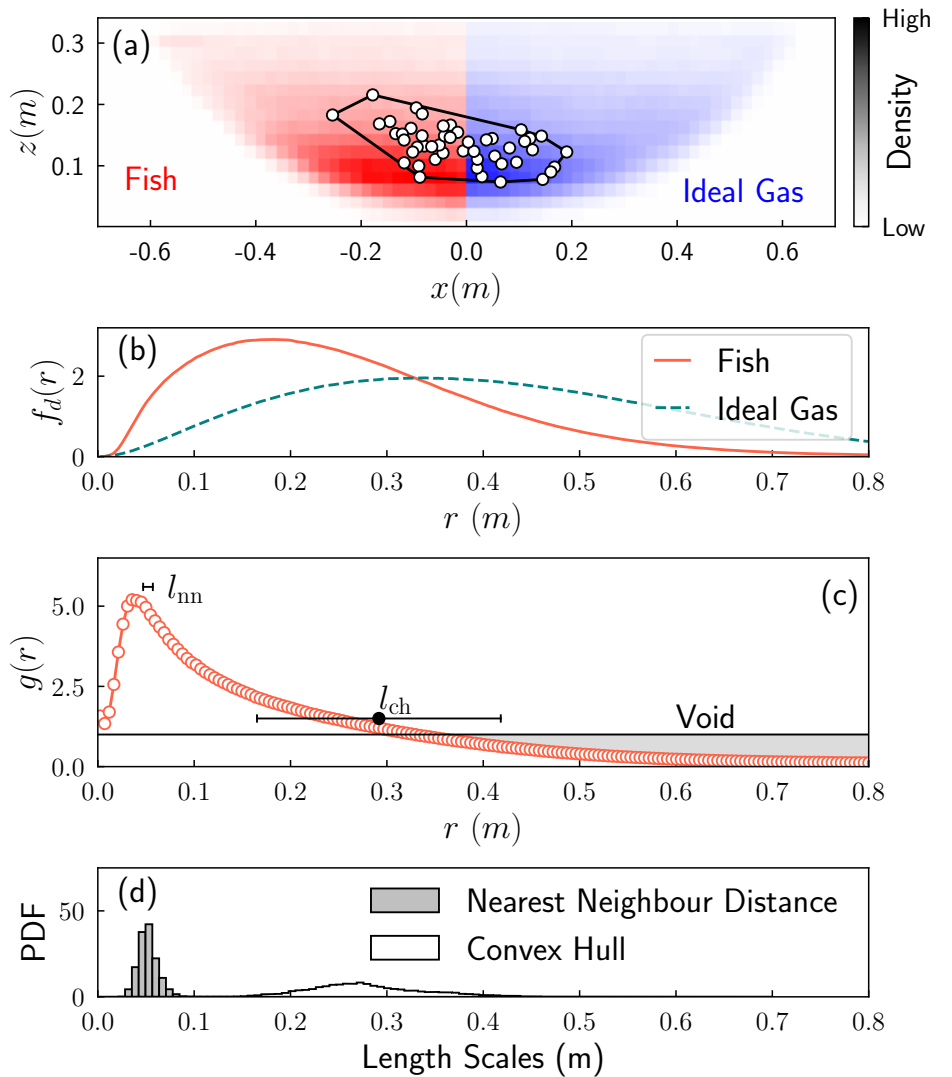
The ratio of two PDFs gives the  $g(r)$  (Eq. 5.6), presented in Fig. 5.10(c). Like the 2D results (Fig. 5.7), the  $g(r)$  exhibits a typical disordered, fluid-like shape, featuring a single peak at  $\sim l_{\text{nn}}$  with a monotonic decay. The height of the peak reaches the value of 5, being larger than the peak height ( $\sim 2.2$ , Fig. 5.7(c)) in the 2D experiment. This difference indicates that the 50 fish were swimming in a more cohesive way in the 3D experiment, comparing with the 2D experiment.

Importantly, the correlation length of the density ( $\xi_\rho$ , Eq. 5.7) is close to the effective convex hull diameter ( $l_{\text{ch}}$ , Eq. 5.5), as shown in Fig. 5.10. This suggests the fish remained a compact, and cohesive group in the 3D experiment. A snapshot of such a cohesive group was plotted as circular markers in Fig. 5.10 (a).

Since the fish always form a compact cluster, a cohesive clique, when they were swimming in the 3D observation tank, there is no void in the length scale of the convex hull of the group. Comparing with the size of the explorable environment, the  $l_{\text{ch}}$  is much smaller, and the void corresponds to the space where the fish aggregation could explore collectively.

The cohesive nature of the fish in the 3D experiment is also supported by the distribution of the  $l_{\text{ch}}$  shown in Fig. 5.10, which is much narrower than that from the 2D experiments. Interestingly, the distribution of  $l_{\text{nn}}$  for the fish swimming in both 3D and 2D environments were close. Numerically, the averaged  $l_{\text{nn}}$  value for the 3D experiments were slightly smaller than the value from 2D experiments (Table 5.1).

**Figure 5.10:** The structure of 50 adult zebrafish in 3D. (a) The joint distribution of the  $x$  and  $z$  coordinates of the fish and the ideal gas particles. The distribution of the ideal gas is biased to be identical to the fish. The location of 50 fish at one time point is plotted as circles. The boundary convex hull of these 50 scatters is plotted as solid lines. (b) The probability density function of the pairwise distributions for the fish and the ideal gas particles. (c) The radial distribution function,  $g(r)$  (Eq. 5.6) of the fish. It is defined as the ratio between the two PDFs in (b). Two important length scales, the nearest neighbour distance and the size of the convex hull were captured by the  $g(r)$ . The long distance region where  $g(r) < 1$  corresponds to the void in the tank, where the group were able to explore. (d) The distribution of the nearest neighbour distance and the effective diameter of the convex hull, of the fish.



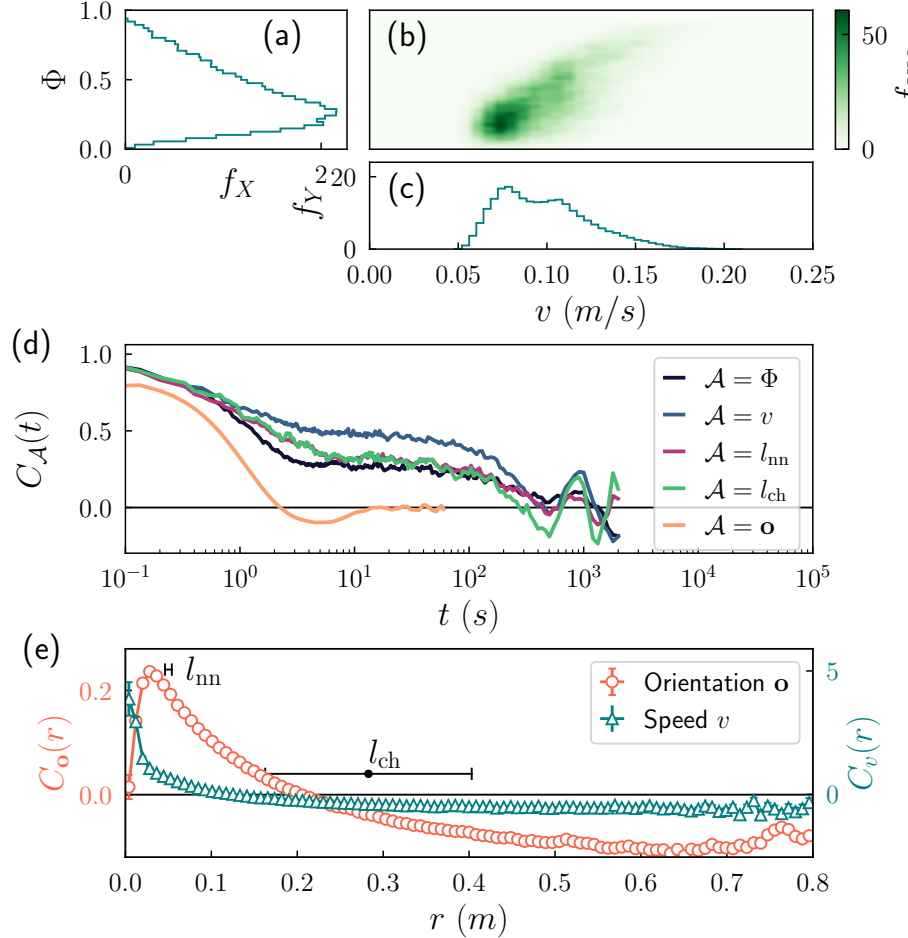


**Figure 5.11:** The dynamics of 50 adult zebrafish in 3D. (a) The probability density function ( $f_\Phi$ , Eq. 5.10). (b) The joint probability density function ( $f_{\Phi v}$ ) for the polarisation ( $\Phi$ ) and the speed ( $v$ ). (c) The probability density function ( $f_v$ ) of the average speed (Eq. 5.9). (d) The autocorrelation function,  $C_A(\tau)$ , of the polarisation ( $\Phi$ ), the average speed ( $v$ ), the nearest neighbour distance ( $l_{nn}$ ), the effective convex hull diameter ( $l_{ch}$ ), and the orientation of each fish ( $\mathbf{o}$ ). (e) The connected correlation function of the orientation ( $\mathbf{o}$ ) and speed ( $v$ ), as a function of pairwise distances.

### 5.6.2 The Dynamics

The dynamics of the 50 zebrafish in a 3D observation experiment is shown in Fig. 5.11. Figure 5.11 (a)-(c) shows the distribution of the speed ( $v$ ) and the polarisation ( $\Phi$ ), as well as the joint distribution of the two. Interestingly, the speed exhibits a bimodal distribution (Fig. 5.11), indicating the fish were changing between a slow state to a fast state during the observation. The joint PDF of  $v$  and  $\Phi$  exhibits a positive correlation, as shown in Fig. 5.11(b).

The ACF of different structural quantities and dynamical quantities for 50 fish were plotted in Fig. 5.11(d). Like the 2D results, these ACFs exhibit two decays, featuring the relaxation of the orientation ( $\tau_0 \sim 1s$ ) and the local density ( $\tau_\rho \sim 120s$ ). The latter timescale is used to separate the observation into separate segments, to study the time evolution of the fish states in section 5.6.3.

The connected correlation function of the speed and orientation of the fish,  $C_v(r)$  and  $C_o(r)$ , was presented in Fig. 5.11(e). Being very similar to the 2D results, the orientation of the fish exhibits a longer correlation length compared with the speed. The two correlation length values,  $\xi_o$  and  $\xi_v$ , are listed in Table 5.1.

Comparing with the 2D results in Fig. 5.8, the fish were swimming at a similar speed in a 3D environment, with  $v_{2D} = 0.11m/s$  and  $v_{3D} = 0.098m/s$ . However, the fish were swimming in a more ordered way in a 3D

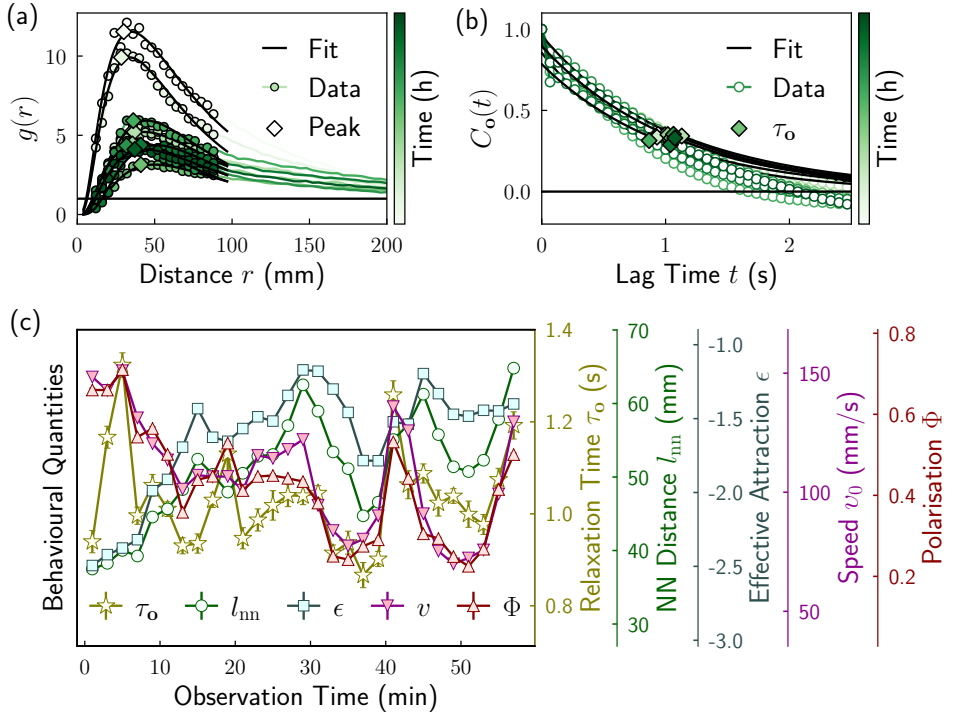


**Figure 5.12:** (a) Sequence of radial distribution functions, the  $g(r)$ , at different time points. In early times (top curves) the fish are clustered together so that the peak is large; at later times (bottom curves) the local density decreases and so does the peak height. (b) Sequence of the auto-correlation function of the orientations  $C_o(t)$  of the fish, at different time points. (c) The time evolution of the averaged behavioural quantities for 50 young fish. Each point corresponds to the average value in 2 minutes. The error bars illustrate the standard error values.

observation, indicated by the high  $\Phi$  values at the tail of the distribution  $f_\Phi$ . It is notable that the ACFs of the structural quantities ( $l_{nn}$  and  $l_{ch}$ ) and dynamical quantities ( $\Phi$  and  $v$ ) sharing the same shape for the fish in the 3D observation. This similarity of the ACFs was not observed in the 2D experiments.

### 5.6.3 The Changing States

To study the changing states of the fish group, we separated the observation into short segments of 120s, and analyse the behaviour of the fish in these short periods separately. The results are shown in Fig. 5.12. For each segment, we calculated the ACF of the orientation, as shown in Fig. 5.12 (b), as well as the  $g(r)$ , plotted in Fig. 5.12(a). From these two correlation functions, we extracted the changing  $\tau_o$  and the changing effective attraction ( $\epsilon$ ) values. Like the behaviour of fish during our 2D observation, the cohesion among the fish gradually decreases, indicated by the decreasing height of the peak in the  $g(r)$ . However, no systematic change of the  $C_o(t)$  were observed.

The time evolution of different structural and dynamical quantities were plotted in Fig. 5.12(c). All these quantities change with time, indicating the fish were constantly changing their states. The speed is correlated with the polarisation, and the nearest neighbour distance is correlated with the effective attraction.

These correlations were also observed from our 2D experiments in Fig. 5.9. The non-linear nature of the time-evolution of fish states revealed the complexity of the behaviour of the fish, and more controlled experiments is necessary to differentiate the possible origins, that are responsible for the changing states of the fish. For instance, a sudden noise in the environment

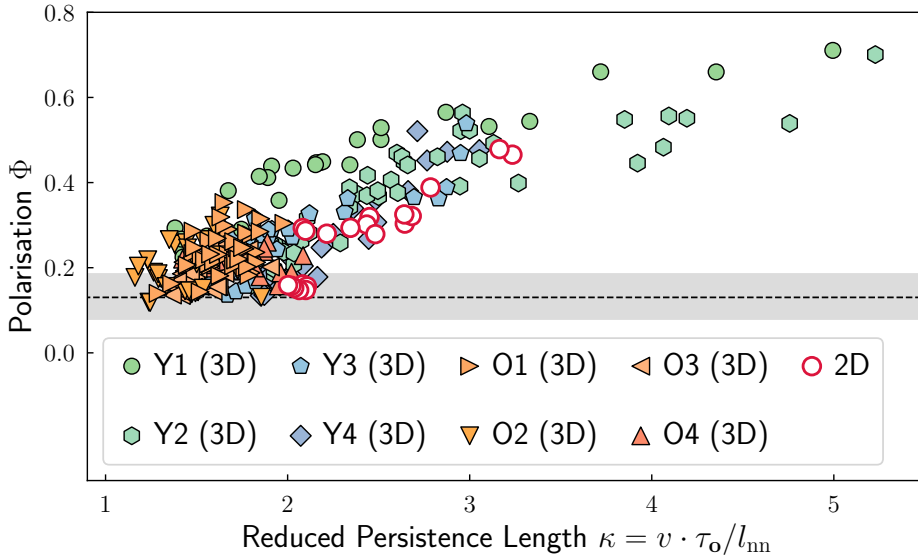


**Figure 5.13:** The relationship between the polarisation, the order of the movement, and the reduced persistence length of the fish. For the 3D observation, multiple repeated measurement with different fish groups at different dates were collected (Y1-Y4: different young fish groups; O1-O4: different old fish groups). All of the observed fish behaviour results were collapsed onto a master curve. The result of one 2D observation was also included, as open circles. The 2D results does not collapse onto the same master curve from the 3D data, because of the difference in the dimensions.

might trigger the jump in speed in Fig. 5.12. But such change, termed as the spontaneous startle cascades in [216], might also emerge naturally without any triggering factor. Unfortunately, the exact cause of these sudden changes is unknown<sup>50</sup>.

## 5.7 The Universal Behaviour of Zebrafish

The complicated changing states of the fish shown in Figs. 5.9 and 5.12, can be captured by one number, regardless of the dimension of the swimming environment. This number is termed as the *reduced persistence length* ( $\kappa$ ), whose definition is,

$$\kappa = \frac{v\tau_o}{l_{nn}} = \frac{l_p}{l_{nn}}. \quad (5.16)$$

The value of  $\kappa$  correlates robustly with the value of polarisation  $\Phi$ , as shown in Fig. 5.13. This correlation is remarkable because it describes all the experimental observations on different adult zebrafish groups, with different ages. A very simple argument for the correlation is that each fish could share its current moving direction with the group, in the lengthscale of  $l_p$ . Such information could be transmitted to more members in a cohesive group, with smaller  $l_{nn}$  value. When more members were exchanging their information about the moving direction, the entire group is more likely to form a consensus, and exhibit ordered movement with a high  $\Phi$  value.

This explanation is helpful because it relates the property of the individual fish (the persistence length, and the local density) to the macroscopic behaviour (the polarisation). Such connection is vital to understand the behaviour of mutant zebrafish, which had significantly larger  $l_p$  values comparing with the wildtype zebrafish. The relevant results will be presented in chapter 7. In addition, it is easy to compare the observed experimental result in Fig. 5.13 with the computer simulations of agent-based models, since both  $\kappa$  and  $\Phi$  are dimensionless numbers. Such comparison will be discussed in chapter 6.

<sup>50</sup> Ideally, I should monitor the noise level and the vibrations of the water in the tank, to study if they affect the fish behaviour or not. However, the relevant data was not recorded. Practically, the experimental setup was located in a relatively quiet room. Closing the door of a nearby room would make a noticeable noise, whose effect on the fish behaviour is unknown.

## Summary of Chapter 5

- We discussed the methods to analyse the experimental coordinates of the zebrafish, in order to study their collective behaviour. There are four steps.

### 1. Refining Coordinates

Some coordinates are very close to each other, which are physically impossible. These overlapping particles can be removed with an optimisation algorithm.

### 2. Linking Coordinates into Trajectories

The refined coordinates can be linked into trajectories, and the short trajectories can be extended using methods in section 5.3.

### 3. Analysing the Structure of the Fish Group

We use the nearest neighbour distance ( $l_{nn}$ ), the size of the convex hull ( $l_{ch}$ ), and the radial distribution function  $g(r)$  to characterise the structure of the fish group.

### 4. Analysing the Dynamics of the Fish Group

We use the average speed ( $v$ ), the polarisation ( $\Phi$ ), the relaxation time scales ( $\tau$ ) to characterise the dynamics of the fish group. In addition, we use the correlation functions of the orientation and the speed,  $C_o(r)$  and  $C_v(r)$ , to measure the dynamical lengthscales.

- We get the following results from the 2D movement of 50 zebrafish.
  - The fish groups segmented into sub-clusters.
  - The fish groups were in the disorder phase, with low polarisation values.
  - The collective motion of the fish groups exhibited a short time scale related to the reorientation of the fish individual (1 s), and a large time scale related to the relaxation of the local density (15 minutes).
  - The correlation length of orientation is longer than the correlation length of the speed.
  - The macroscopic state of the fish group changes over time, indicated by the changing quantities in Fig. 5.9.
- We get the following results from the 3D movement of 50 zebrafish.
  - The fish group remained a cohesive cluster without fragmentation.
  - The fish group switched between the ordered phase and the disorder phase, with varying polarisation values.
  - The collective motion of the fish group exhibit a short time scale related to the reorientation of the fish individual (1 s), and a large time scale related to the relaxation of the local density (2 minutes).
  - The correlation length of orientation is larger than the correlation length of the speed.
  - The macroscopic state of the fish group changes over time, indicated by the changing quantities in Fig. 5.12.
- The change of the macroscopic states of the zebrafish groups is not totally random. The ratio between the persistence length and the nearest neighbour distance, for both 2D and 3D data, presents a robust correlation with the polarisation. The fact, that similar conclusions were reached from 2D and 3D experiments, is in accordance with previous studies [217, 218].

# Chapter 6

## Modelling Zebrafish

人相忘乎道术

---

庄子

### 6.1 Introduction

In this chapter we will study the behaviour of the zebrafish with the help of computer simulation. The goal of the simulation is to reproduce the experimental results from chapter 3 to chapter 5. We will use the Monte-Carlo simulation to study a system in equilibrium, in order to reproduce the spatial distribution of the fish under the influence of the boundary, the gravity, as well as the pairwise interaction. In addition, we will use a dynamical simulation to study an agent-based<sup>51</sup> active matter model, in order to recreate the dynamical feature of the fish group in the experiments.

The density distribution of the fish was strongly affected by the presence of the boundary, as the fish were physically constrained in the tank. For the 3D experiment, the distribution of the fish was also affected by an “effective gravity”, as well as the holes drilled on the tank. These environmental factors can be treated as external fields affecting the fish. In addition to these external factors, the fish-fish interaction will also change their distribution. With the Monte-Carlo (MC) simulation techniques, we can study these effects individually. Using such simulation method, we assumes the fish group were in equilibrium. Such assumption is not valid since a group of fish is an active matter system. By applying this invalid assumption, we implicitly tested the idea of mapping active matter system to an equilibrium counterpart, where the non-equilibrium feature of the system, the activity, was summarised by an effective temperature<sup>52</sup> [64, 219]. The MC approach ignores the dynamics of the system, but will give us insights regarding the structure (density distribution) of the fish group.

For a group of fish, the order of their dynamics, captured by the polarisation value (Eq. 5.10), correlates robustly with a non-dimensional value  $\kappa$ , the ratio between the persistence length ( $l_p$ ) and the nearest neighbour distance ( $l_{nn}$ ). Such a correlation suggests the local density and the persistence motion of the fish dominated the polarisation of the system. Since the persistence motion is a proxy to the *activity* of the fish, the entire group of

<sup>51</sup> The dynamical simulation is similar to the Brownian dynamics simulation for the liquid, where all the particles were updated according the force exerted on them. It's different from the Monte-Carlo simulation where the particles are moved randomly. The moving individuals in the model can take different names, like the “particles”, “animals”, and “agents”. The term “agents” will be used in this chapter for consistency.

<sup>52</sup> This “effective equilibrium” picture is supported by the exponential decay of the excess distribution function shown in section 4.3.1, as the decay suggests the Boltzmann-like distribution commonly seen in equilibrated systems.

50 zebrafish is behaving like an alignment dominated active matter system (section 2.1.2). To confirm the similarity of a group of zebrafish, and a model active matter system, we will use the dynamical simulation method to simulate the famous active matter model, the Vicsek model [35]. Such simulation ignores the structure of the fish group, where all the structural features are absorbed into the number density parameter in the model (section 6.4.1). To get a good fit between the model and the experiments, we will have to modify the Vicsek mode and consider the orientational inertia of the fish. The fitting of the model and the experimental result suggests the existence of the effective alignment interaction among the fish. And the changing states of the fish could be understood as a change of the noise level for the model.

## 6.2 Simulation Methods

### 6.2.1 General Idea

If we think of fish as a collection of agents following pre-defined movement rules, we could reproduce the movement of the fish with the computer simulation. Formally, we call a collection of agents a *system*. And the system can change its (microscopic) states over time. By observing the system for a long time, we could obtain the trajectory of the system, and then calculate the quantities that we are interested in (see chapter 5 for examples). Such process is summarised in the following algorithm (Algorithm 6). During the simulation, the system change its states under some constraints. For example, the constraints could be a controlled noise level ( $\beta$ ), a constant number density ( $\rho$ ), and a fixed total number ( $N$ ) of agents.

---

#### Algorithm 6: The Simulation Procedure

---

```

Data: Constraints  $\{\beta, \rho, N, \dots\}$ 
Result: Trajectory
System  $\leftarrow$  initial microscopic state with  $\{\beta, \rho, N, \dots\}$ ;
repeat
    change the microscopic state of the system with  $\{\beta, \rho, N, \dots\}$ 
until System is stable, and forgets the initial microscopic state;
Trajectory  $\leftarrow \emptyset$ ;
repeat
    change the microscopic state of the system with  $\{\beta, \rho, N, \dots\}$ ;
    Put current state in Trajectory;
until The statistics are good enough;

```

---

### 6.2.2 Monte-Carlo Simulation

There are multiple ways to change the state of the system in algorithm 6. In a seemly arbitrary fashion, we could change the state of the system randomly, and reject some states that is unlikely to happen. This method is termed “Monte-Carlo” (MC) simulation, and the acceptance ratio were often determined by the Metropolis algorithm. Typically, the acceptance ratio from state  $\zeta$  to  $\nu$ ,  $A(\zeta \rightarrow \nu)$ , is written as

$$A(\zeta \rightarrow \nu) = \begin{cases} \exp(-\beta(E_\nu - E_\zeta)) & \text{if } E_\nu - E_\zeta > 0 \\ 1 & \text{otherwise.} \end{cases}$$

And the values of  $E_\nu$  and  $E_\zeta$  represent the energy values of state  $\nu$  and  $\zeta$ , respectively. The value  $\beta$  is the inverse temperature. The smaller  $\beta$  value is, the higher the temperature, and the larger randomness the system exhibits. Sampling the states with this acceptance ratio, we are effective sampling an equilibrium system, whose states follow the Boltzmann distribution. For a microscopic state  $\nu$ , its probability to be sampled is  $\exp(-\beta E_\nu)/Z$ , were  $Z$  is a normalisation factor (the partition function).

With MC simulation, it is easy to constrain the agents in the fish tank, by setting  $E = \infty$  once an agent is outside the tank.<sup>53</sup> In addition, the effect of external fields, like gravity, can be added easily to the simulation. However, due to the lack of “true” dynamics in the MC simulation, we will not have access to the velocities of the system. Hence, this simulation method is only used to model the spatial distribution of the zebrafish.

### 6.2.3 Dynamical Simulation

Another way to change the state of the system is to integrate the *equation of motion* of all the agents. For animals, the equations to be integrated represent the behavioural rules of the agents. Being different from the conventional molecular dynamics simulation or mesoscale simulations [69], the simulation of animal behaviour often incorporates more eccentric rules, such as a fixed vision zone[80, 220], and an attraction to the group centre [79]. Generally, the updating rules for the agents could be described by the following equation,

$$\begin{aligned} \mathbf{v}_i^{t+1} &= \mathcal{B}[\mathbf{v}_i^t] \\ \mathbf{x}_i^{t+1} &= \mathbf{x}_i^t + \mathbf{v}_i^{t+1}, \end{aligned}$$

where the operator  $\mathcal{B}$  encodes all the behavioural rules of the animals. By changing the coordinates and velocities of all the agents simultaneously, we change the state of the system (Algorithm 6).

## 6.3 The Distribution of the Density

In this section we will model the spatial distribution of the fish in the 3D experiment. The simulation will illuminate the effects of the environmental factors, such as the fish tank and the gravity. By comparing with the experimental density distribution, we can get phenomenological parameters such as the effective temperature, to describe the behaviour of the fish.

### 6.3.1 The Effect of the Tank

The 3D geometry of the tank confining the zebrafish was determined in section 4.2.1, and the shape of the tank can be expressed as,

$$z = cr^2,$$

<sup>53</sup> Operationally, we reject the states if any agent is outside the fish tank.

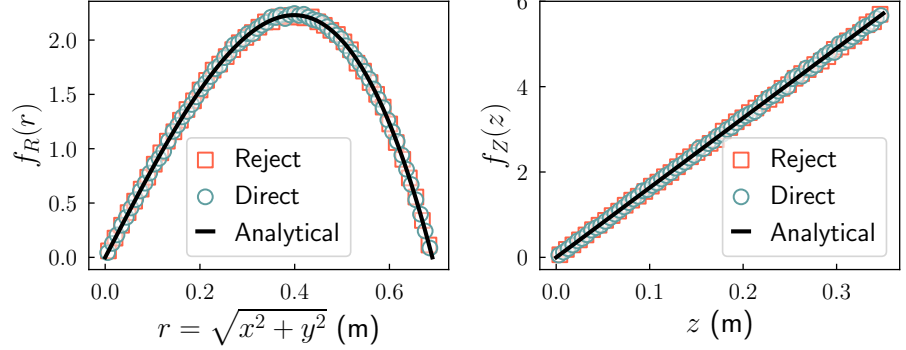


**Figure 6.1:** The marginal probability density distribution of points sampled uniformly inside the experimental fish tank. Left: the distribution the planar radius  $r$ . Right: the distribution of the  $z$  component of the points.

where  $c = 0.74m^{-1}$  when both  $r$  and  $z$  were expressed in the unit of meters. The volume ( $V$ ) of the tank can be calculated as

$$V = \int_0^h \pi \frac{z}{c} dz = \frac{\pi h^2}{2c},$$

where  $h$  is the height of the tank, the vertical distance between the water surface and the base of the tank. The joint probability density function (PDF) of random points, being uniformly distributed inside the tank, is written as,

$$f(x, y, z) = V^{-1} = \frac{2c}{\pi h^2}.$$

The joint PDF of the uniform distribution can be expressed in the spherical coordinates as,

$$f(\theta, r, z) = \frac{2c}{\pi h^2} r, \quad (6.1)$$

where  $\theta$  is the azimuthal angle,  $r = \sqrt{x^2 + y^2}$  is the radius in  $XY$  plane. From the expressions above, we can calculate the marginal distribution of  $r$  and  $z$  coordinates:

$$f_R(r) = \int_0^{2\pi} d\theta \int_{cr^2}^h dz f(\theta, r, z) = \frac{4c}{h} r - \frac{4c^2}{h^2} r^3, \quad (6.2)$$

$$f_Z(z) = \int_0^{2\pi} d\theta \int_0^{\sqrt{z/c}} dr f(\theta, r, z) = \frac{2}{h^2} z.$$

The analytical result (Eq. 6.2) is checked against the numerical sampling of random points inside the tank, as shown in Fig. 6.1. These PDFs can be used as comparison for the distribution of real fish data, as presented in section 4.3. The experimental distribution of the fish is very different from the ideal gas distribution.

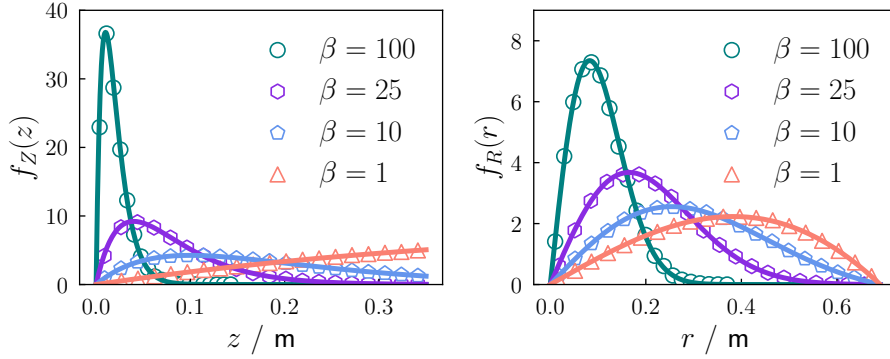


**Figure 6.2:** The marginal probability density distribution of ideal gas particles sampled uniformly inside the experimental fish tank, where the particles were subjected to the gravity field. Left: the distribution the  $z$  component. Right: the distribution of the  $r = \sqrt{x^2 + y^2}$ . The scatters were result of Monte-Carlo simulations, and the solid lines were from Eq. 6.4.

### 6.3.2 The Effect of the “Gravity”

From the results presented in section 4.3, it is evident that the zebrafish will be affected by an “effective gravity”, because of their depth preference behaviour. This effective gravity is similar to As a first attempt, we could calculate the density distribution of ideal gas particles in equilibrium, with an Boltzmann weight  $\exp(-\beta z)$  to capture the effect of the gravity. The *partition function* ( $Z$ ) of the system is written as,

$$Z = \int_0^h \pi \frac{z}{c} \exp(-\beta z) dz = \frac{\pi(1 - \exp(-\beta h)(1 + \beta h))}{c\beta^2}.$$

With the partition function, we could then calculate the joint probability density function of the ideal gas, in the spherical coordinate system (similar to Eq. 6.1).

$$f(\theta, r, z) = \frac{r \exp(-\beta z)}{Z} = \frac{c \exp(-\beta z) r \beta^2}{\pi(1 - \exp(-\beta h)(1 + \beta h))} \quad (6.3)$$

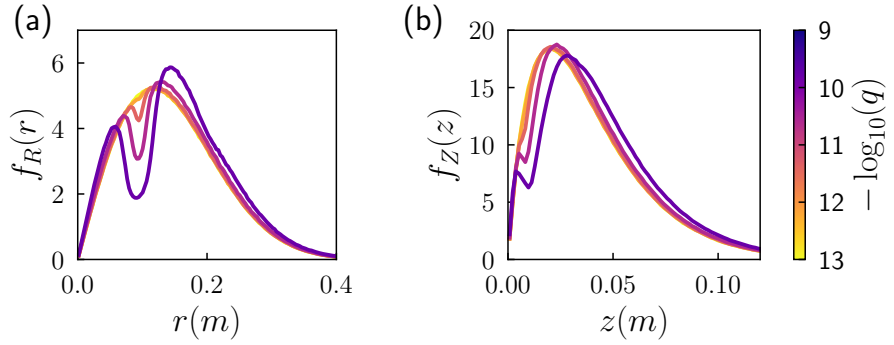
where  $\beta = 1/(k_B T)$  is the inverse temperature. For a physical systems in equilibrium, the vale of  $\beta$  relates to the real temperature measured by a thermometer. However, the value of  $\beta$  for the fish only controls the level of randomness of the system, without a concrete physical meaning. From the function  $f(\theta, r, z)$ , we can calculate the distribution functions  $f_R(r)$  and  $f_Z(z)$ :

$$f_R(r) = \int_0^{2\pi} d\theta \int_{cr^2}^h dz f(\theta, r, z) = \frac{2c (\exp(\beta(h - cr^2)) - 1) r \beta}{\exp(\beta h) - \beta h - 1}, \quad (6.4)$$

$$f_Z(z) = \int_0^{2\pi} d\theta \int_0^{\sqrt{z/c}} dr f(\theta, r, z) = \frac{\exp(-z\beta) z \beta^2}{1 - \exp(-\beta h)(1 + \beta h)}.$$

The results from Eq. 6.4 were checked against the Monte-Carlo simulation results, as shown in Fig. 6.2. With the increase of  $\beta$ , hence the decrease of temperature, the agents were pushed towards smaller  $z$  values and  $r$  values. By “fitting” the experimental results with the analytical results from Eq. 6.4, and setting  $\beta$  as a free parameter, we could obtain the effective temperature for the fish.

**Figure 6.3:** The effect of the holes on the density distribution of ideal gas in the fish tank subjected to gravity field. (a): the distribution the  $z$ . (b): the distribution of the  $r$ . The colour of the lines indicates the strength of the repulsive interaction of the holes on the tank. The simulation was carried out with parameter  $\beta = 50$ , where  $7.5 \times 10^6$  coordinates were sampled.



### 6.3.3 The Effect of the Holes

In our 3D fish observation experiments, the holes on the tank disrupted the density distribution of the fish. This disruption makes the result in Eq. 6.4 very different from the distribution of the fish, as shown in section 4.3.5. To mimic such effect, we could model holes as an extra field, with the following form,

$$H(r, z) = q \sum_i \frac{[(r - r_i)^2 + (z - cr_i^2)^2]^{-2}}{r_i}, \quad (6.5)$$

where  $r_i$  represents the location of the holes on the tank. Specifically, there are three sets of holes (Fig. 4.11), located at  $r_1 = 96$  mm,  $r_2 = 213$ , and  $r_3 = 327$  mm. The denominator ( $r_i$ ) in Eq. 6.5 represents the fact that equal amount of holes were drilled on the circles. So that the larger circles will have less holes per unit length. The factor  $q$  controls the strength of the repelling interaction between the fish and the holes.

Calculating the corresponding density distributions,  $f_R(r)$  and  $f_Z(z)$ , analytically is difficult, but we can estimate the density distribution with the Monte-Carlo simulation. Figure 6.3 shows the result of the simulation. As expected, the distribution  $f_R(r)$  appears bimodal with a locally minimum  $q$  value at the location  $r = r_1$ .

### 6.3.4 The Effect of Pairwise Interaction

The simulations in section 6.3.1 to 6.3.3 treat the agents as ideal gas particles, without any interaction between the agents. This is not realistic, since the  $g(r)$  of the zebrafish exhibits characteristic features (Fig. 5.10 (c) in section 5.6.1). In order to enable the agents to behave more like the zebrafish in the simulation, we added an effective interaction among the agents. We assume the interaction is pairwise, and spherically symmetrical, therefore ignored the possible many-body interactions [133].

To implement the pairwise interaction in the Monte-Carlo simulation, we assign the effective potential energy<sup>54</sup>,  $u(r)$ , for all the pairs of agents. The potential energy is written as,

$$u(r) = -p \log [g(r)]$$

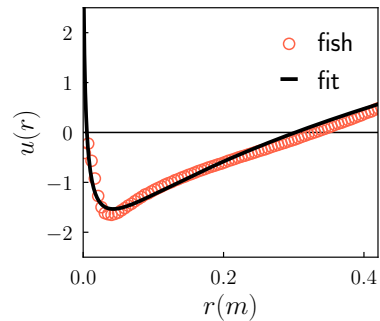
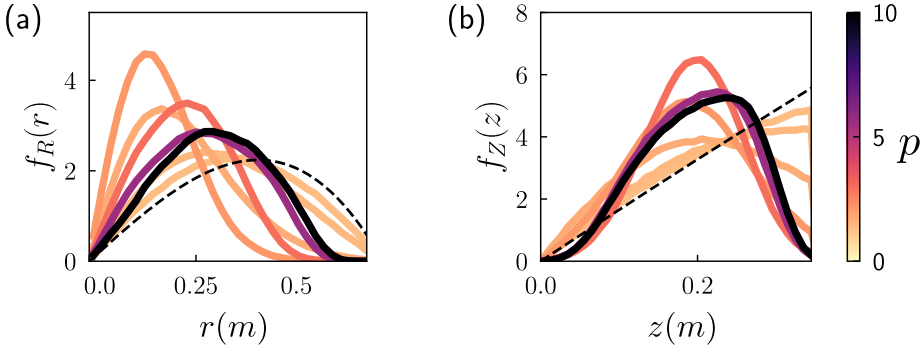


Figure 6.4: Fitting the  $u(r)$  of fish with Eq. 6.6.

<sup>54</sup> Notice the logarithm of  $g(r)$  is  $-\beta u(r)$  for equilibrium systems. Here we ignored the  $\beta$ , and we controlled the strength of the pairwise interaction with parameter  $q$ . The reason for our choice is that we are only interested in the approximated shape of  $u(r)$ , which makes the fish forming a coherent group.



**Figure 6.5:** The effect of the pairwise interaction among the agents, on their density distribution. (a): the distribution the planner radius  $r = \sqrt{x^2 + y^2}$  of the agents' coordinates. (b): the distribution of the  $z$  component of the agents' coordinates. The colour of the solid lines indicates the strength of the pairwise interaction of the fish. The dashed lines corresponds to the result where  $p = 0$ . The simulation was carried out with parameter  $\beta = 0.1$ , where  $5 \times 10^5$  coordinates were sampled.

where  $p$  is a free parameter that determines the contribution of the interaction between the agents. To parameterise the experimental  $u(r)$ , we fitted it with function

$$u(r) = \log(a_1) - \log(2) \left[ \frac{\log(1 + 2a_2(r - a_3)/a_4)}{a_2} \right]^2, \quad (6.6)$$

where  $a_1 - a_4$  are fitting parameters. Figure 6.4 shows the fitting result, where the potential energy took a minimum at the location of nearest neighbour distance. We can incorporate this pairwise interaction into the energy form during the Monte-Carlo simulation, to study its effects. Formally, the energy of the system could be written as,

$$E = \begin{cases} \sum_i \left[ z_i + H(r_i, z_i) + \sum_{j \neq i} u(d_{ij}) \right] & \text{if } cr_i \leq z_i < h \\ \infty & \text{otherwise} \end{cases} \quad (6.7)$$

where the coordinate of agent  $i$  is  $(x_i, y_i, z_i)^\top$ , with  $r_i = \sqrt{x_i^2 + y_i^2}$ . The condition ( $cr_i \leq z_i < h$ ) ensures the agents staying in the boundary. This “energy” is a mixture of the effective gravity<sup>55</sup>, the repulsive holes, and the pairwise interaction, and it is controlled by parameter  $p$  and  $q$ . When both  $p$  and  $q$  are equal to zero, the agents behave like ideal gas in the tank subjected to the effective gravity. But tuning the value of  $p$  and  $q$ , we increase the effect of the pairwise interaction and the holes.

The effect of the pairwise interaction of the fish on the density distribution is shown in Fig. 6.5, where we fixed the value of  $q$  (which controls the strength of the fish-hole interaction) to be 0, and set  $\beta = 0.1$ . These parameters correspond to the condition where the effects of both the gravity and the holes could be ignored. When the value of  $p$  is small, so that the interaction among the agents are weak, the system behaves like ideal gas particles under gravity, described by Eq. 6.5. When the value of  $p$  was gradually increased from  $10^{-2}$  to 1, the fish tend to aggregate near the bottom of the tank in the centre.

Notably, the further increase of  $p$  would change the density distribution of the fish in a different fashion. As the value of  $p$  increased from 1 to 10, the fish are more frequently appear at higher  $r$  and  $z$  values. Such non-monotonic behaviour could be understood by carefully examining the

<sup>55</sup> Notice we implicitly transformed the height of the fish ( $z_i$ ) to the potential energy in an effective gravitational field in Eq. 6.7.

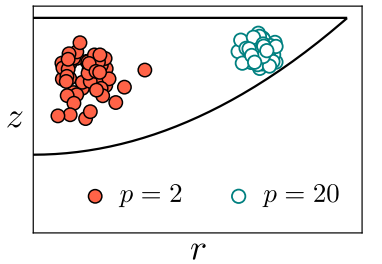
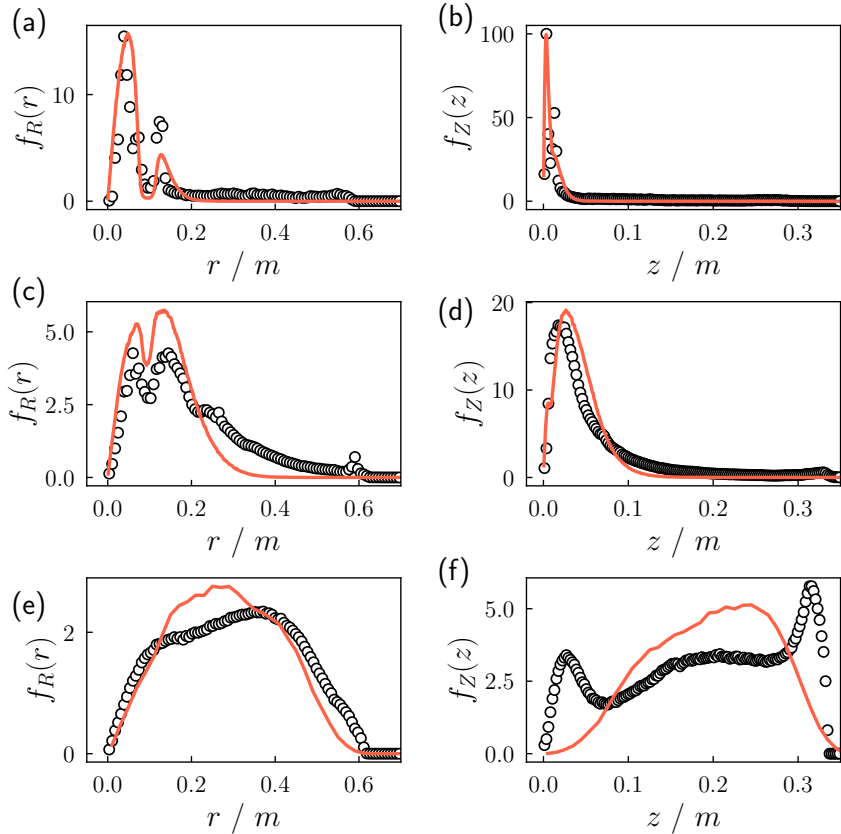


Figure 6.6: The parameter  $p$  controls the size of the group.



**Figure 6.7:** The comparison of the density distribution of fish with the model described by Eq. 6.7. The data points represent the experiment measurements, and the solid lines were calculated from the Monte-Carlo simulation. (a): the distribution the  $z$  from 1 fish. (b): the distribution of the  $r$  from 1 fish. (c): the distribution the  $z$  from 2 fish. (d): the distribution of the  $r$  from 2 fish. (e): the distribution the  $z$  from 50 fish. (f): the distribution of the  $r$  from 50 fish.

effective interaction potential  $u(r)$  of the agents. Typically, the interaction potential would constrain the agents to form a coherent cluster, to mimic the observed structure of the fish group (section 5.6.1). And the size of the cluster would decrease, with the increase of  $p$ , as shown in Fig. 6.6. For smaller clusters, they would be able to explore the “corner” of the fish tank, where both  $r$  value and  $z$  value are high. On the other hand, the large clusters would have to deform its shape, paying extra energy cost, so that they could enter the corner region. Therefore, the agents with stronger pairwise interaction would explore more space in the tank, presenting higher chance to appear in regions where  $r$  and  $z$  values are high.

### 6.3.5 Comparison to Experimental Data

We used the energy term in Eq. 6.7 to simulate the equilibrium density profile of the agents, and compare the results with our experimental data obtained in chapter 4. By tuning the parameters, typically the values of  $\beta$ ,  $q$ , and  $p$  manually, we can generated simulation result that is similar to the experimental results. The fitting result is shown in Fig. 6.7.

For the distribution of one fish in the tank, the fitting results suggests an effective inverse temperature of  $\beta = 200$ , and the strength of the fish-hole interaction of  $a = 2 \times 10^{-10}$ , as presented in Fig. 6.7 (a) and (b). By decreasing the value of  $\beta$  to 45, and incorporating the fish-fish interaction with  $p = 10$ , we could model the density profile of 2 fish, as shown in Fig. 6.7 (c) and (d). There is a slight mismatch between the experiment and the model, which might related to the non-equilibrium nature of the fish, which

is absent in our Monte-Carlo simulation.

To match the density profile of 50 fish, the value of  $\beta$  needs to be further decreased to 0.1, while keeping the  $q$  and  $p$  values unchanged. However, the match between the experimental data and the model is poor. In fact, the bimodal distribution of  $f_Z(z)$  of 50 fish, shown in Fig. 6.7 (f), indicates the presence of multiple states, as reported in section 5.6.3. To take multiple states into consideration, we will need to overlay simulation results from multiple systems with different parameters. Such a complex simulation is beyond the scope of this chapter.

Even though the fitting between the experimental density distribution and that from the Monte-Carlo simulation is not very good, the result is in accordance with our previous discussion in chapter 3 and 4. Namely, when the number of fish is small, the interaction between the fish and the environment (gravity and holes) is significant. Such importance could be translated to a high  $\beta$  value in our model. For a group of 50 fish, the fish-fish interaction dominates their behaviour, corresponding to a low  $\beta$  value.

### 6.3.6 Limitation of the Model

It is important to stress the limitation of our model to describe the behaviour of the fish. Importantly, our Monte-Carlo simulation essentially assumed the fish were in equilibrium states, in which detailed balance is satisfied [209]. This is not true for the zebrafish, as a group of fish constantly dissipate their biological energy to swim. Visually, the movement of fish is very different from the movement of atoms in the gaseous or fluidic phases. For example, if we play the movie of swimming fish backwards, it looks very unnatural. In addition, the interaction between the fish and the environment is speculative. Here we assumed the tank is a hard boundary, and the depth preference of the fish were described by an effective gravity, and the holes have an effective parabolic repelling interaction. And these assumptions may not be accurate, which requires scrutiny.

## 6.4 The Order of the Dynamic

The movement of a group of fish can exhibit two visually different states. The fish may exhibit *ordered* movement, swimming in the same moving direction, with a high polarisation ( $\Phi$ ) value. Alternatively, the fish may exhibit random movement, where they swim in different directions. The switch between random movement and ordered movement is observed for a group of fish in Chapter 5.

Intuitively, the ordered movement is a special state comparing with its random counterpart. And animals have to somehow make something happen, to effectively align with each other and share the same moving direction. In this section, we will try to model this process.

### 6.4.1 The Vicsek Model

The Vicsek model is a very simple active matter model for the dynamics of the animals [35]. Essentially, the agents align with nearby neighbours in the

**Figure 6.8:** The phase behaviour of the Vicsek model. The simulation was performed at different state points, with different density and noise values. The total number of states was  $50 \times 50 = 2500$ . For each state point, 200 agents were simulated, whose speed was fixed at 0.1. The system was updated  $2 \times 10^4$  steps to reach steady state. The polarisation of the system was recorded in the subsequent  $2 \times 10^4$  steps. (a) The time-average polarisation at different states. (b) The standard deviation of the polarisation at different states. This value represents the susceptibility of the system. The dashed line in both subplots indicates a linear relationship between the transitional density and noise. The end of the dashed line *does not* imply the presence of a critical point.

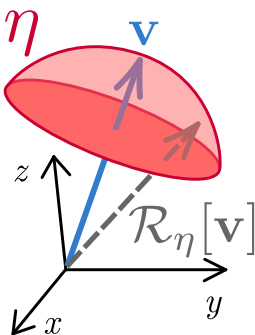
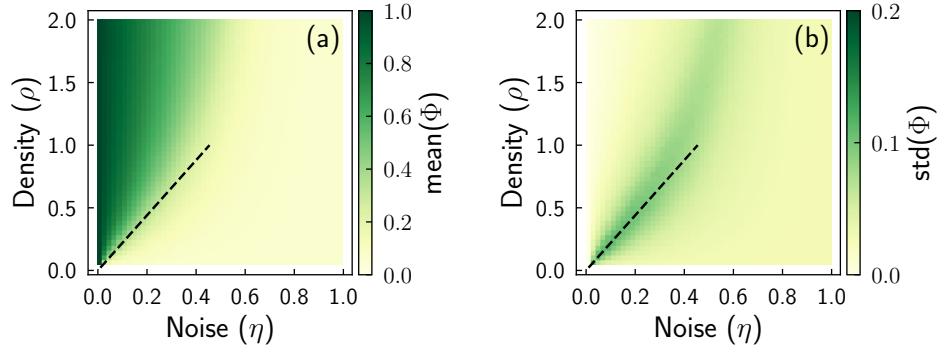


Figure 6.9: The scalar noise in the Vicsek model.

model, leading to the ordered movement. The Vicsek model and its derivatives enjoyed considerable success in describing the collective behaviour of animals. Typically, the equation of motion for the Vicsek model is written as [35],

$$\begin{aligned} \mathbf{v}_i^{t+1} &= v_0 \mathcal{R}_\eta \left[ \Theta \left( \sum_{j \in S_i} \mathbf{v}_j^t \right) \right] = \mathcal{V}(\mathbf{v}_i^t) \\ \mathbf{x}_i^{t+1} &= \mathbf{x}_i^t + \mathbf{v}_i^{t+1}, \end{aligned} \quad (6.8)$$

where  $\mathbf{v}_i^t$  represents the velocity of the  $i$ th agent at time point  $t$ . The symbol  $S_i$  represents the set containing the neighbours of agent  $i$  within the unit distance. The operator  $\Theta$  is responsible for normalising a vector to unit norm. The operator  $\mathcal{R}_\eta$  will rotate a vector randomly around its orientation, adding orientational noise into the system. Such random rotation effectively draws a spherical cap around the vector to be rotated, and the value of  $\eta$  determines the area of this spherical cap. Formally, the noise is referred to as *scalar noise* in the Vicsek model, as opposed to vectorial noise [37]. We use the symbol  $\mathcal{V}$  to represent the velocity updating rule of the Vicsek model.

The important parameters for the Vicsek model are the noise ( $\eta$ ) and the number density ( $\rho$ ), when we set the interaction range to one. The noise controls the randomness of the system, and the density controls the neighbour set  $S_i$  for particle  $i$ . In addition to  $\rho$  and  $\eta$ , another contributing parameter is the speed of the agents ( $v_0$  in Eq. 6.8), but its effect is less significant than  $\eta$  and  $\rho$ . Therefore, we will only focus on  $\eta$  and  $\rho$ .

The behaviour of the Vicsek model is presented in Fig. 6.8 (a), characterised by the polarisation ( $\Phi$ ) as the order parameter. In the low noise and high density region, the system exhibits ordered behaviour. For the

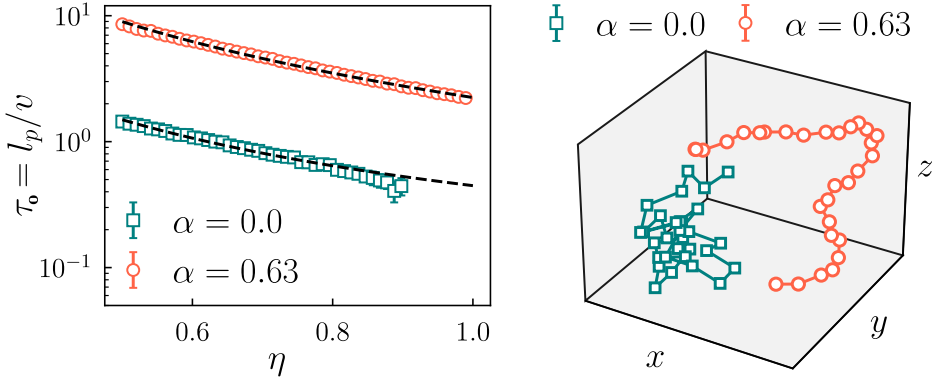


**Figure 6.10:** The effect of inertia, noted as  $\alpha$  in Eq. 6.9, for a single agent in the Vicsek model. (a) The relaxation time of the orientation as a function of the orientation noise ( $\eta$ ). The dashed line shows a polynomial fit, where we assume  $\tau_o \sim \eta^{-2}$  [170]. For the Vicsek model in the noisy region ( $\eta > 0.9$ ), the relaxation time is hard to measure because of its small numerical value. (b) The trajectories of agents with different  $\alpha$  values.

low density and high noise simulations, the agents move randomly with a small  $\Phi$  value. Figure 6.8 (b) shows the standard deviation of the polarisation from the simulation, whose maximum value indicates the transition between the ordered phase and the disordered phase. In the dilute region, where  $\rho < 1$ , the transitional density  $\rho_c$  and noise  $\eta_c$  have a linear relationship, as indicated by the dashed line in Fig. 6.8. Such linear relationship is in accordance with previous 3D numerical simulation results [221].

If we try to compare the Vicsek model with the experimental result, the model would fail, as shown in Fig. 6.12 (a). This is because the real zebrafish reached the most random state ( $\Phi \sim 0.13$ ), with a minimum  $\kappa$  value of 1.5. That is to say, the fish would have some excess persistence length even in their most random states. The excess persistence length is expected, as the real fish do not change their orientation at arbitrarily high frequencies. However, this “minimum persistence length” does not exist in the Vicsek model, as the Vicsek agents do indeed, change their orientation at a frequency  $\sim \infty$ , in their most random state, where  $\eta = 1$ , and  $\Phi \sim 0.13$ .

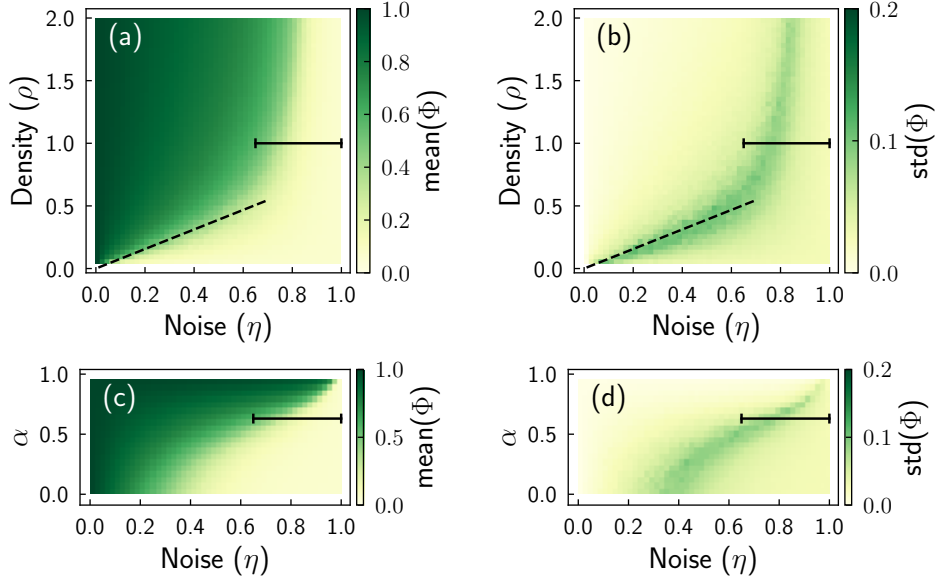
#### 6.4.2 The Effect of Inertia

One heuristic approach to modify the Vicsek model, so that the model could fit the experimental result, is to remedy the extreme zigzag movement of the agents in the high noise region. For a real zebrafish, we expect its swimming pattern to be inertial, since the Reynold number for an adult zebrafish is around 20000 [222]. To incorporate an effective inertia, we could simply let the agents to remember their previous orientations, by rewriting the equation of motion as the following,

$$\begin{aligned} \mathbf{v}_i^{t+1} &= v_0 \Theta [(1 - \alpha) \mathcal{V}(\mathbf{v}_i^t) + \alpha \mathbf{v}_i^t] \\ \mathbf{x}_i^{t+1} &= \mathbf{x}_i^t + \mathbf{v}_i^{t+1}, \end{aligned} \quad (6.9)$$

which is effectively a linear mixture of the Vicsek interaction, noted as  $\mathcal{V}(\mathbf{v}_i^t)$ , and the original velocity ( $\mathbf{v}_i^t$ ). The parameter  $\alpha$  controls the ratio between the moving direction from Vicsek interaction to the existing moving direction, and we call it the *inertia*. When  $\alpha$  is zero, the model is reduced to the Vicsek model. When  $\alpha$  is one, all the agents will travel ballistically without any interaction. The trajectories of a single agent with different  $\alpha$  values are presented in Fig. 6.10(b). The agent with moderate  $\alpha$  value

**Figure 6.11:** The phase behaviour of the Vicsek model with inertia. The simulation detail is the same to those described in Fig. 6.8. The horizontal bars represents the region that matched our experimental results. (a) The time-averaged polarisation at different states with different  $\rho$  and  $\eta$  values, with  $\alpha = 0.63$ . (b) The standard deviation of the polarisation at different states with different  $\rho$  and  $\eta$  values, with  $\alpha = 0.63$ . This value represents the susceptibility of the system. (c) The time-averaged polarisation at different states with different  $\alpha$  and  $\eta$  values, with  $\rho = 1$ . (d) The standard deviation of the polarisation at different states with different  $\alpha$  and  $\eta$  values, with  $\rho = 1$ . This value represents the susceptibility of the system.



presents a smooth trajectory, as expected. Figure 6.10 (a) shows the scaling relationship between the orientational relaxation time and the noise, where  $\tau_0 \sim \eta^{-2}$ . Such relationship is in accordance with previous proposals [170, 221]. The incorporation of the “inertia” ( $\alpha$ ) does not change such the scaling relationship, and it only slows down the relaxation of the orientation of the agents.

The behaviour of the Vicsek model with the inertia is shown in Fig. 6.11. The structure of the phase diagram<sup>56</sup> is similar to that without inertial, where the agents exhibits ordered behaviour in the high density and low noise region, and they perform random movement in the dilute and noisy states. However, the incorporation of the inertia ( $\alpha = 0.63$ ), visually, increases the area of the ordered region in Fig. 6.11. Here we give a hand-waving argument for such an observation. The increase of the  $\alpha$  value would increase the persistence length of the agents (Fig. 6.10). Therefore, these agents would interact with more neighbours, before they forget their original orientations. The increased interaction promotes the propagation of the information within the group, leading to ordered movement.

At a moderate density level ( $\rho = 1$ ), the phase diagram spanned by the noise  $\eta$  and the inertia  $\alpha$  is presented in Fig. 6.11 (c), with the corresponding susceptibility shown in Fig. 6.11 (d). Generally, the increasing  $\alpha$  value expands the ordered region in the parameter space (Fig. 6.11), which is in accordance with the argument that  $\alpha$  increase the order of the system by inducing more interactions among the agents.

#### 6.4.3 Comparing with the Experiment

The parameters in the Vicsek model with inertia, namely the noise  $\eta$ , the density  $\rho$ , and the inertia  $\alpha$ , were manually adjusted to fit the 3D experimental observations in section 5.7. The comparison was shown in Fig 6.12 (a), where the simulation results were plotted as a solid line, and it matches the experimental results. This line was obtained by simulating the Vicsek

<sup>56</sup> Figures 6.11 (a) and (c), as well as Fig. 6.8 (a), revealed two phases of the Vicsek model: the ordered phase with high  $\Phi$  values, and the disordered phase with  $\Phi \sim 0$ .

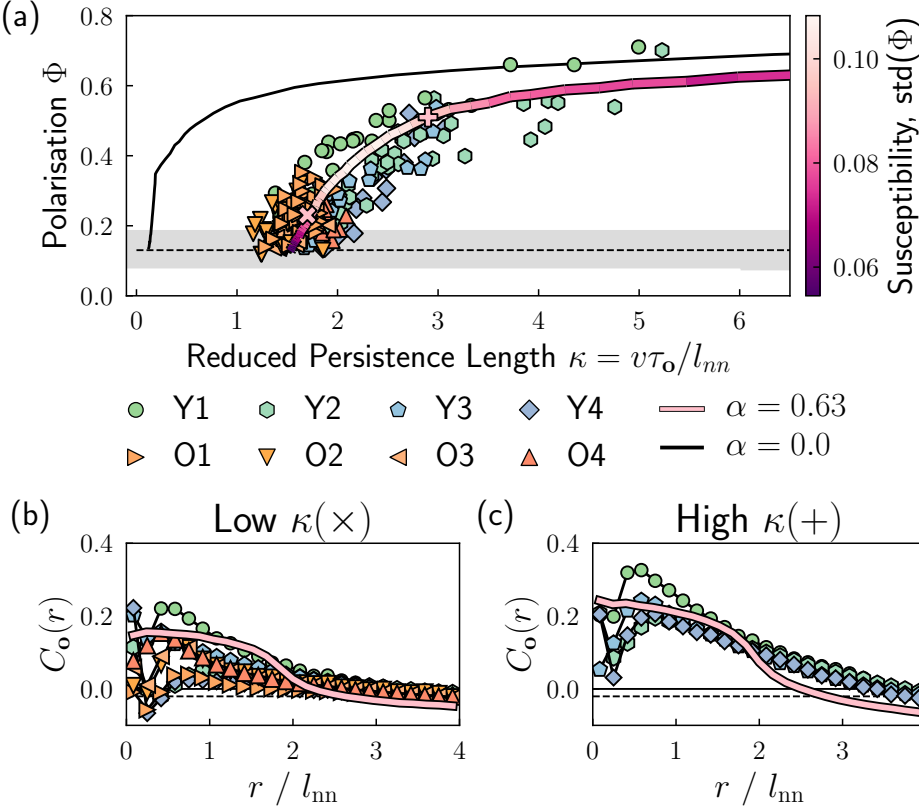


**Figure 6.12:** Comparing the dynamics of the zebrafish with the Vicsek model simulation. (a) The relationship between the rescaled persistence length  $\kappa$  and the polarisation  $\Phi$ . The scatters represent different experimental observations. The solid line represent the simulation result with Vicsek model ( $v = 0.1, \alpha = 0, \rho = 1, 0.18 \leq \eta \leq 0.9$ ). The thick solid line with colour represent the simulation result of the Vicsek model with inertia ( $v = 0.1, \alpha = 0.63, \rho = 1, 0.65 \leq \eta \leq 1$ ). The brightness of the colour represent the standard deviation of the polarisation in different states. (b) The connected correlation function  $C_o(r)$ , calculated from the experimental data (scatters) and the simulation (solid line) in the low  $\kappa$  region. (c) The connected correlation function  $C_o(r)$ , calculated from the experimental data (scatters) and the simulation (solid line) in the high  $\kappa$  region.

model with a fixed speed ( $v = 0.1$ ) and fixed inertia ( $\alpha = 0.63$ ), while varying the value of the noise term ( $0.65 \leq \eta \leq 1$ ). The parameters being simulated were also plotted as horizontal bars in Fig. 6.11.

The matching between the simulation and the experimental results indicates the existence of effective alignment between the fish. And the increasing persistence length at fixed nearest neighbour distance promotes the transformation of information in the group, therefore increase the order.

We also calculated the connected correlation function ( $C_o(r)$ , Eq. 5.14) of the orientation for the simulation results, and compared the results with the one in the simulation. The comparisons were plotted in Fig. 6.12 (b) and (c). In Fig. 6.12 (b), the correlation function from the states with a low  $\kappa$  value were compared, and the results in Fig. 6.12 (c) shows the correlation function in the states with high  $\kappa$  values. In both cases, the simulated agents exhibits different  $C_o(r)$ , compared with the zebrafish. Such deviation is expected, as the information about the spatial correlations, like the  $g(r)$ , was ignored in our model.

Our model for the dynamics of the fish revealed the importance of the inertia. As mentioned in section 6.4.1 and shown in Fig. 6.12 (a), the Vicsek model without inertia, whose  $\alpha$  value equals zero, could not fit the experimental result. The mismatch between the model is especially significant in the low  $\kappa$  region where the noise term is high, which is related to the unrealistic zig-zag movement of the Vicsek agents (Fig. 6.10). The increasing of the  $\alpha$  value shifted the simulation result to the high  $\kappa$  region, that matches the experimental result.

The simplicity of our model is important. The good fit between the

simulation results and the experimental results indicates that the order of the dynamics (the polarisation) for the zebrafish group can be described by the four parameters (the density, the inertia, the speed, and the noise) in the model. This is because the dynamics of the fish group is dominated by their effective alignment interaction. For a group of 50 fish, their changing states can be captured by the noise parameter ( $\eta$  in Eq. 6.8), as shown in Fig. 6.12 (a), suggesting the observed zebrafish behaviour is universal.

It is also important to point out that our model suggests that the fish were effectively crossing the boundary between the ordered phase and the disordered phase (see the horizontal bars in Fig. 6.11). The location of the boundary, for 50 agents, is located at  $\kappa \sim 2$ , where the susceptibility of the polarisation took its maximum, as shown in Fig. 6.12 (a). This result is expected for the collective behaviour from a group of animals. Sometimes it is referred to as a dogma that “all biological systems were poised near a critical state” [223]. For the observed fish, they were clearly not just staying at a critical state, because the state of the group was constantly changing (section 5.5.3 and 5.6.3). However, the simulation indicates that the fish were, at least, close to the phase boundary between the ordered movement and disordered. In other words, the animals tend to stay on the fence, between the ordered state and the disordered state. Such choice is understandably beneficial, because staying in the disordered state essentially means the group could not move collectively. On the other hand, forcing the group in the ordered state means the informed individual could not change the overall moving direction of the entire group.

#### 6.4.4 Limitations of the Model

Finally, it is important to address the several limitations of our simulation, even though the fitting is visually good. First of all, the agents in the Vicsek model have a constant speed ( $v$  in Eq. 6.8), and this is different from the zebrafish. In addition, the only interaction between the agents is the alignment, while we could see evidence for the repulsive interaction and attractive interaction amongst the fish in section 5.5.1 and 5.6.1. Finally, the inhomogeneity of the density inside the tank is ignored in the Vicsek model, and the agents were enclosed in a periodic boundary, rather than a fish tank.

## Summary of Chapter 6

- We modelled the density distribution of the fish as an equilibrium system, featuring the following elements.
  - The observation tank as a hard boundary.
  - The depth preference of the fish as an effective gravity.
  - The holes on the tank which repel the fish.
  - The fish-fish interaction inferred from the  $g(r)$  of the fish.
- By fitting the experimental density distribution and the results from the model, we get the following conclusions.
  - For the 1/2/3 fish experiments, the interaction between the fish and the environment dominates the density distribution.
  - For a group of 50 zebrafish, the fish-fish interaction is important to their density distribution.
- We modelled the ordering process of the dynamics of the fish group with an active matter model (the Vicsek model). We get the following results.
  - The original Vicsek model can not fit the experimental data.
  - If an inertia term was added to the Vicsek model, the simulation results fit the experimental data.
  - The universal relationship between the reduced persistence length ( $\kappa$ ) and the polarisation ( $\Phi$ ) reported in section 5.7 can be understood, as the decreasing noise ( $\eta$ ) values in our model, which lead to higher polarisation.
- There are several limitations for our model.
  - The simulations carried out in section 6.3, to model the density distribution of the fish, ignored the dynamics of the system, by assuming the density profile was from an equilibrium system.
  - The simulations in section 6.4, to model the dynamics of the fish, ignored the inhomogeneous density distribution, as well as the two point density correlation observed from the experimental  $g(r)$  profile.

# Chapter 7

## Collective Behaviour of Mutant Zebrafish

### 7.1 Introduction

In this chapter, the methods developed in previous chapters will be applied to study the behavioural change of zebrafish when they carry mutations in genes relevant to human disease. The idea is to use the behavioural feature as a probe, so that we could test the functions of different genes. Such idea was implemented by the pioneering work from Tang et al., who tested the behaviours of different fish groups with different genetic modifications [179]. Even though the massive screening process could pick up different features of different genetic mutations, there is little explanation for the observations.

Instead of screening many different genes, we will take a different approach, and only focus on one particular gene in this chapter, the *col11a2* gene. This gene is responsible for the production of an alpha chain of type XI collagen [24]. Mutations to Col11a2 (as well as to Type II and Type IX collagen) are associated with Stickler syndrome. Stickler syndrome is characterised by hearing loss, problems with vision, and progressive changes to the skeleton which result in severe early onset osteoarthritis [224, 225]. For zebrafish, such mutation is also found to cause premature osteoarthritis [24]. Here we hypothesise that changes to the skeleton, or to visual and auditory perception would lead to changes to swimming behaviour, either through increased joint stiffness or a failure to correctly perceive their position in the water. This expectation is supported by the reported correlation between swimming performance and the development of bones [83] and cartilage [226].

Observing, analysing, and modelling the 3D swimming behaviour from both the mutant fish, and the wildtype (*wt*) fish, we studied the behavioural differences caused by the *col11a2* mutation. Notably, the mutant fish have a significantly longer orientational relaxation time ( $\tau_o$  in Eq. 5.12). And the slow reorientation of the mutant fish leads to a longer persistence length, since the speed of both kinds (the mutant and the wildtype) are similar. Collectively, the mutant fish exhibit higher polarisation value, which can be explained by the dynamical model in chapter 6. Our analysis provided the behavioural feature of the mutant fish, and provide a direct link between the

microscopic feature of the fish to their corresponding collective behaviour. The linkage is remarkable, because it bridges the gap between the biological feature of the fish and the collective behaviour of the group, under the framework of active matter physics.

## 7.2 Method

### 7.2.1 Mutant Fish

The *col11a2* mutant zebrafish have a nonsense mutation, i.e. in the mutants the Coll1a2 protein is no longer produced. The mutant fish were obtained from European Zebrafish Resource Centre and bred in the fish facility in the university of Bristol [24]. Two generations of mutant fish were crossed by Elizabeth A. Lawrence and Erika Kague respectively from the university of Bristol. The wildtype zebrafish were also crossed and bred in the same time, so that the two groups sharing the same growth condition can be compared. For each generation, the number of wt fish is  $\sim 50$ , and the number of mutant fish is  $\sim 30$ .

The two different generations of “mutant + wildtype” combinations, crossed at different time points, exhibits consistent behavioural features. The fish were observed when they were 40 days post fertilisation (dpf), by which point they are relatively skeletally mature. We carried out the observation repeatedly, until the fish were about 120 dpf.

### 7.2.2 Experiments and Analysis

Both the mutant fish and the wildtype fish were kept in aquarium tanks in a separate room, without the observation equipment. The husbandry of the fish is introduced in section 3.2.1.

For the one-fish experiment, we randomly took 10 fish from their living tank, to the observation room, and recorded the movement of each fish individually for 10 minutes at a frequency of 15 frames per second. We then circulate the water in the observation tank for 5 minutes to remove possible olfactory responses [200], then started recording for another fish. We carried out the experiment for the two generations of the mutant and wildtype fish, therefore tested 40 fish in total.

For the many-fish experiments, we randomly selected 25 fish, and transferred them to the observation tank. We waited 10 minutes for the group to get familiar with the new environment, and then started recording their movement. We carried out the experiment for the two different generations, and we tested 4 groups, 100 fish in total.

The 3D fish tracking apparatus, introduced in chapter 4, was used to record the 3D coordinates of the fish. These coordinates were then linked into trajectories following the methods discussed in chapter 5. The trajectories were analysed following the methods in chapter 5, yielding the results that could be fitted with the modified Vicsek model with inertia (chapter 6).

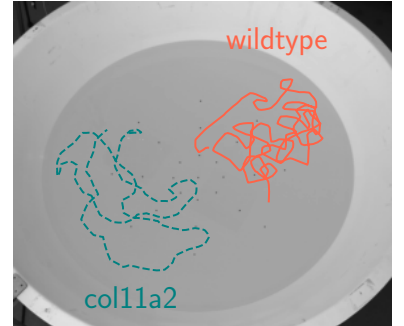
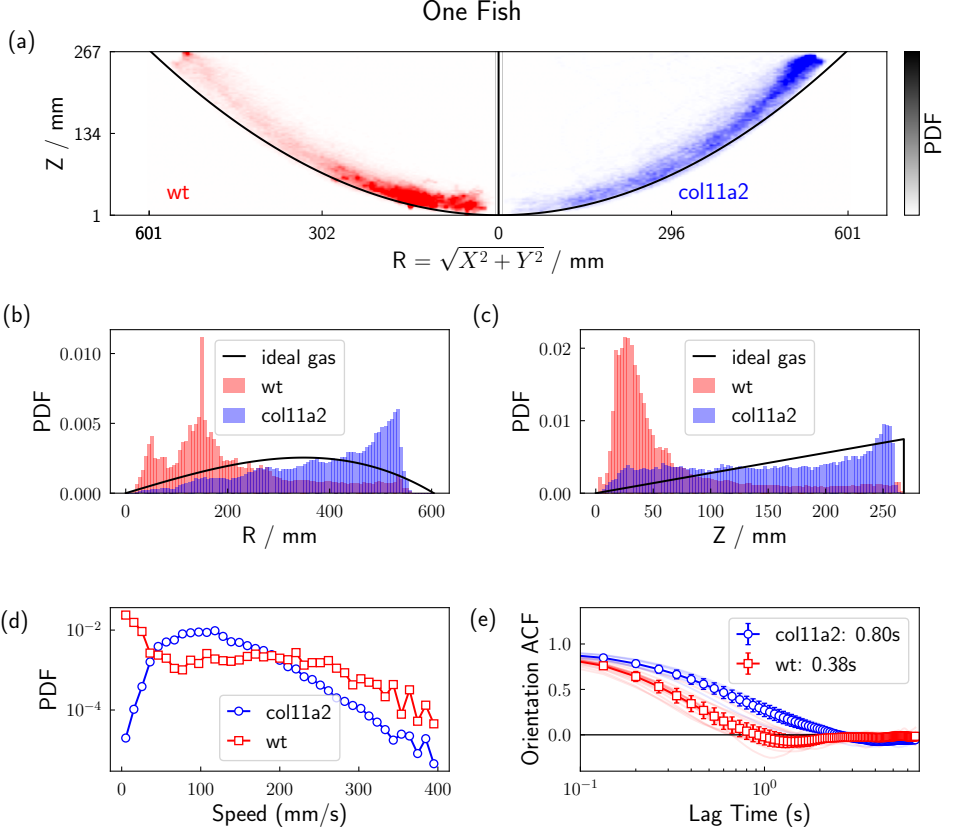


Figure 7.1: Typical trajectories of the *col11a2* mutant zebrafish and the wildtype zebrafish



### 7.3 The Behaviour of A Single Mutant Fish

The movement of one single fish differs significantly between the wt fish and the *col11a2* mutant zebrafish, as shown in Fig. 7.2. For all the different fish individuals, they tend to move near the surface of the tank, as seen in Fig. 7.2 (a). Comparing with the *col11a2* mutant zebrafish, the wt fish prefer the bottom of the tank, as shown in Fig. 7.2 (c). Besides the spatial distribution, the wt fish frequent stops swimming in the tank, indicated by the peak around 0 mm/s in the speed distribution (Fig. 7.2 (d)). However, the wildtype fish also have a longer tail in the speed distribution, meaning they are more likely to enter the high speed state (speed  $> 300$  mm/s).

A notable difference between the wt fish and mutant fish is the dynamics of the orientation. The *col11a2* mutant zebrafish took a significantly longer time to change their directions, indicated by the auto correlation function of the moving direction ( $C_o(t)$ , Eq. 5.11) of the fish. The results are shown in Fig. 7.2 (e). By fitting the ACFs with an exponential function (Eq. 5.12), we obtained the characteristic reorientation timescale of the wt fish (0.38s) and *col11a2* mutant zebrafish (0.8s). Visually, the slow re-orientation of the *col11a2* mutant zebrafish leads to a smoother trajectory, while the trajectory of the wt fish appeared to be more zigzag. These characteristic trajectory shapes were shown in Fig. 7.1. The slower re-orientation of the mutant fish might be attributed to their altered skeletal phenotype in which joints are abnormal [24]. But more work is needed to prove this causality.

It is important to point out, that we took extra care for the calculation

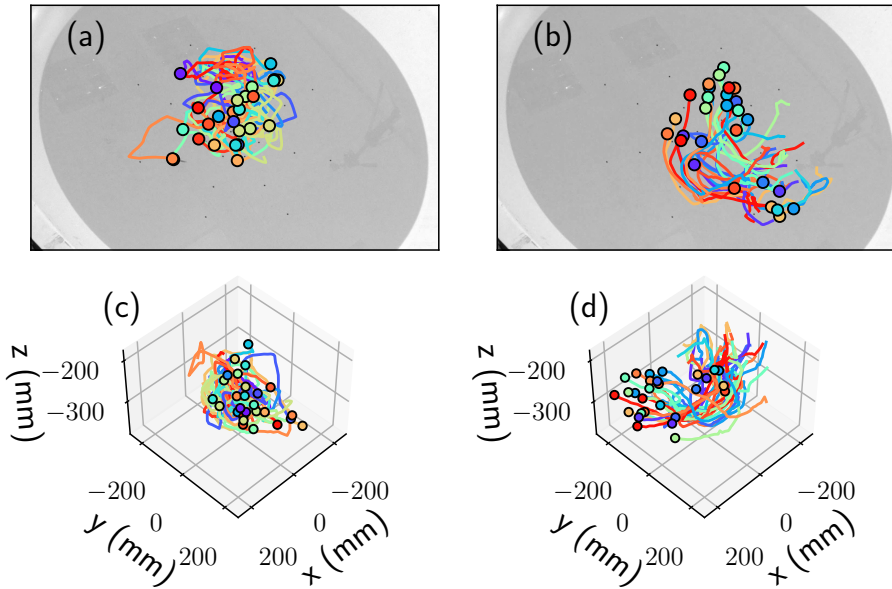


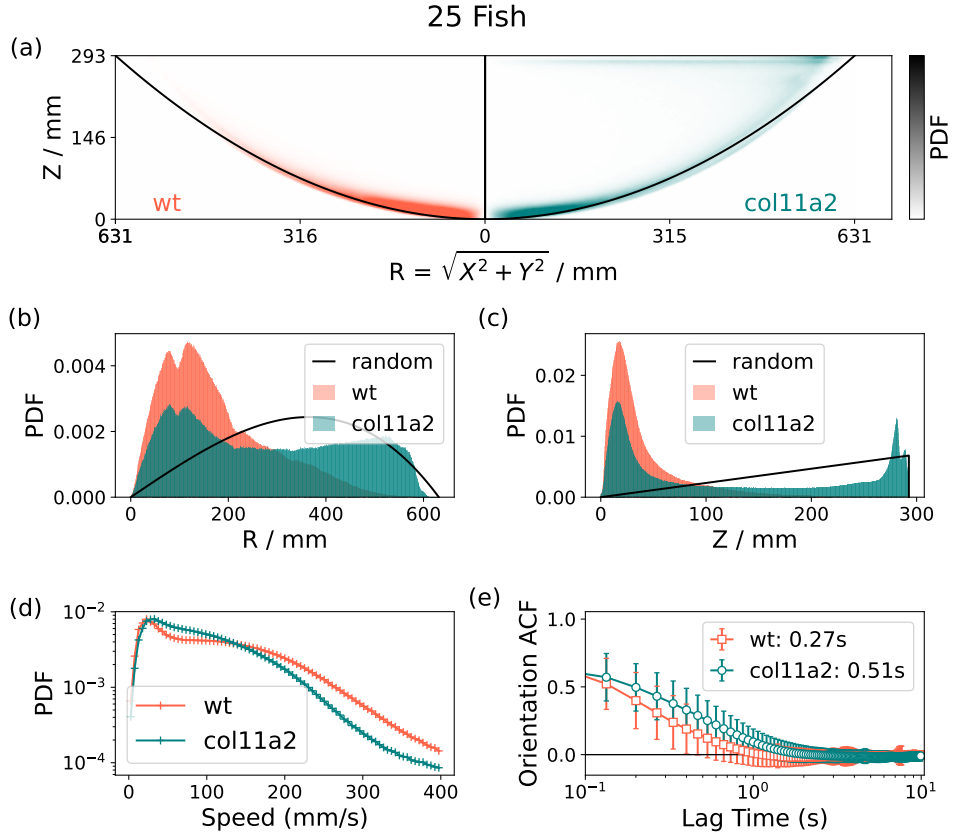
**Figure 7.3:** The trajectories of 25 wildtype zebrafish and *col11a2* mutant zebrafish. (a) The trajectories of wildtype zebrafish projected onto a camera in 5s. (b) The trajectories of *col11a2* zebrafish projected onto a camera in 5s. (c) The 3D trajectories of wildtype zebrafish in 5s. (d) The 3D trajectories of *col11a2* zebrafish in 5s.

of the relaxation time, since the re-orientation process of the fish can be affected by extrinsic factors. For instance, the directional change of the non-moving fish will be dominated by the tracking error, and the fish in the bottom of the tank will be forced to change direction more frequently, because the otherwise ballistic motion will be interrupted by the tank. To exclude these extrinsic effects, we excluded the non-moving time points in the trajectories (speed  $< 50$  mm/s), and focused only on a specific height region ( $50\text{mm} < z < 150\text{mm}$ ) during the calculation of the ACF. The choice of the speed threshold or the height region will not affect the conclusion, but will change the numerical value of these time scales.

In summary, we find three significant differences between the wt fish and the *col11a2* mutant zebrafish. The wt fish prefer the bottom of the tank, and the wt fish tend to stop swimming during the observation. The *col11a2* mutant zebrafish however takes much longer time to change their moving directions, presenting a smoother trajectories over time (Fig. 7.1). These features were robust, as we repeated the experiment by crossing two new groups of wt fish and the *col11a2* mutant zebrafish, and obtained results leading to the exact same conclusions.

## 7.4 The Behaviour of Many Mutant Fish

In addition to the one fish experiment, we also observed a group ( $n = 25$ ) of wt fish and *col11a2* mutant zebrafish, and analysed their behaviours. Visually, the *col11a2* mutant zebrafish are more likely to swim together, while the movement of the wildtype fish seemed more random. The typical trajectories of 25 wt fish and 25 *col11a2* mutant zebrafish are shown in Fig. 7.3. Where the trajectories captured by the cameras were presented in Fig. 7.3 (a) and (b), whose corresponding 3D trajectories were shown in Fig. 7.3 (c) and (d), respectively.



#### 7.4.1 The Behavioural Features of *col11a2* mutant zebrafish

All of the behavioural features of the mutant fish, summarised in section 7.3, were also observed in the 25 fish experiment, as shown in Fig. 7.4. Namely, the wt fish tend to distribute at the bottom of the tank (Fig. 7.4 (a) and (c)), and these fish also tend to stop swimming, leading to a peak around 0 mm/s in the distribution of the speed values (Fig. 7.4 (d)). In contrast, the *col11a2* mutant zebrafish present different spatial distribution and speed distribution, as the *col11a2* mutant zebrafish were more likely to stay on the top of the water, and tend to maintain a moderate swimming speed.

The different orientational relaxation time ( $\tau_o$ ) values, as illustrated in Fig. 7.4 (e), were also observed in the many-fish experiment. The *col11a2* mutant zebrafish have a typical value of  $\tau_o = 0.5s$ , while the wildtype fish have a typical relaxation time of  $\tau_o = 0.27s$ . The standard deviation of the ACFs from the 25-fish experiments are larger, comparing with the single fish experiment. This is because we repeated the observation multiple times. And the fish gradually grew during this period. In addition, the repeated exposure to the experimental environments might also change the behaviour of the fish [227]. Nevertheless, the different orientational relaxation time values for the *col11a2* mutant zebrafish and wt fish were repeatedly observed, being a robust behavioural feature.

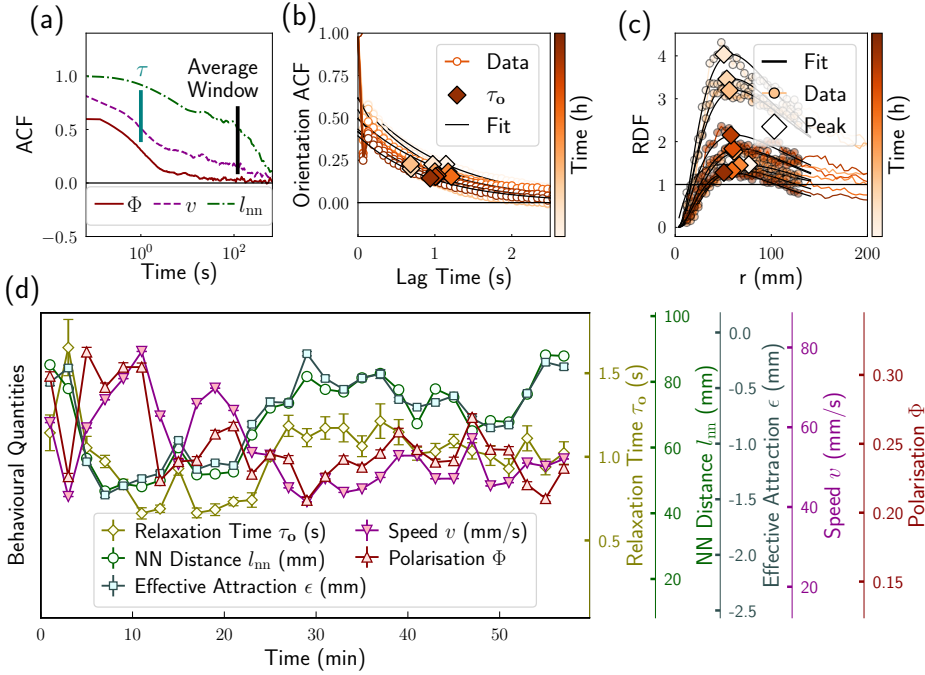


**Figure 7.5:** The Collective Behaviour of 25 wt zebrafish. (a) The ACFs of the polarisation ( $\Phi$ ), the speed ( $v$ ), and the nearest neighbour distance ( $l_{nn}$ ). The first decay corresponds to the relaxation of the orientation, and the second decay is taken as the average window where the long trajectories were segmented into. (b) The ACFs of the orientations ( $C_0(t)$ ) of the fish at different time points. (c) The radial distribution function (RDF, the  $g(r)$ ) of the fish group at different time points. The heights of the peaks are linked to the effective attraction ( $\epsilon$ ) of the fish. (d) The changing states of the fish captured by the orientational relaxation time ( $\tau_o$ ), the speed ( $v$ ), the polarisation ( $\Phi$ ), the nearest neighbour distance ( $l_{nn}$ ), and the effective attraction ( $\epsilon$ ).

#### 7.4.2 The Changing States of *col11a2* mutant zebrafish

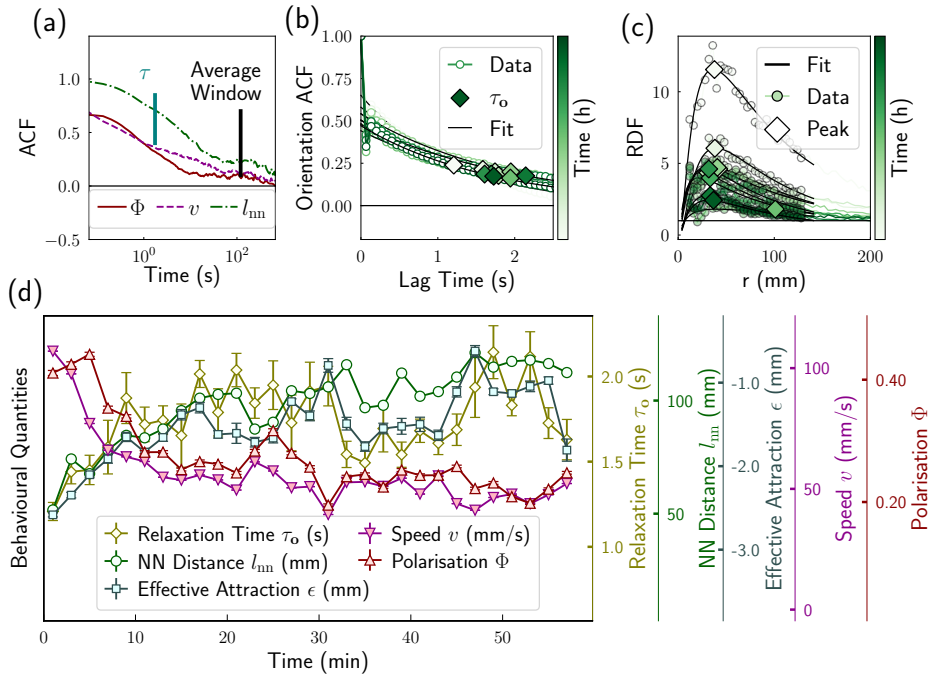
The macroscopic states of 25 zebrafish change over time, like the scenario presented in section 5.6.3 and 5.5.3. These changing states of wildtype fish were plotted in Fig. 7.5. Figure 7.5 (a) shows the ACFs of the polarisation ( $\Phi$ ), the speed ( $v$ ), as well as the nearest neighbour distance ( $l_{nn}$ ). Again, we observed the separated timescales, where the relaxation of orientation caused the initial decay of the ACFs, followed by a second decay that indicates the relaxation of the density.

We segmented the observed trajectories into short segments, whose duration values were 120 seconds, indicated by the vertical bar “Average Window” in Fig. 7.5 (a). The statistical analysis on these segments revealed the fluctuating behaviour of 25 wildtype fish. Figure 7.5 (b) shows the changing  $C_0(t)$  functions of the wt fish, which lead to the fluctuating  $\tau_o$  values in Fig. 7.5 (d). Similarly, the fish group also presents varying degree of cohesion, captured by the effective attraction  $\epsilon$  in Fig. 7.5 (d). The changing cohesion levels are also obvious in the radial distribution function of the fish shown in Fig. 7.5 (c).

These changing states are visually correlated, like the results from section 5.6.3 and 5.5.3. Importantly, the correlations are consistent. The dynamical quantities ( $\Phi$  and  $v$ ) are correlated, while the structural quantities ( $l_{nn}$  and  $\epsilon$ ) are correlated. The orientational relaxation time ( $\tau_o$ ) correlates with the structural quantities, where the fish exhibited slower reorientation when they were less cohesive. The changing relaxation time values could be explained by the short range repulsive interaction of the fish (section 5.6.3).

For 25 *col11a2* mutant zebrafish, we also observed their changing states in a very similar fashion, as shown in Fig. 7.6. One notable difference between the wt fish and the *col11a2* mutant zebrafish is the ACF of the nearest neighbour distance. Specifically, the first decay reached to a value close to 0.3, meaning the system will forget about its current  $l_{nn}$  quicker than

**Figure 7.6:** The Collective Behaviour of 25 *col11a2* zebrafish. (a) The ACFs of the polarisation ( $\Phi$ ), the speed ( $v$ ), and the nearest neighbour distance ( $l_{nn}$ ). The first decay corresponds to the relaxation of the orientation, and the second decay is taken as the average window where the long trajectories were segmented into. (b) The ACFs of the orientations ( $C_0(t)$ ) of the fish at different time points. (c) The radial distribution function (RDF, the  $g(r)$ ) of the fish group at different time points. The heights of the peaks are linked to the effective attraction ( $\epsilon$ ) of the fish. (d) The changing states of the fish captured by the orientational relaxation time ( $\tau_o$ ), the speed ( $v$ ), the polarisation ( $\Phi$ ), the nearest neighbour distance ( $l_{nn}$ ), and the effective attraction ( $\epsilon$ ).



the wt fish. For consistency, we still applied the duration of 120 seconds to segment the trajectories of the *col11a2* mutant zebrafish temporally, and analyse the evolving states.

The orientational relaxation time of the *col11a2* mutant zebrafish is significantly longer than that of the wt fish. The wildtype fish have a  $\tau_o$  value around 1s, while the *col11a2* mutant zebrafish have a  $\tau_o$  value around 2s. These two values here are larger than that from section 7.4.1, because the data presented in Fig. 7.5 and 7.6 were obtained when the fish were 40 dpf. In contrast, the results presented in section 7.4.1 are the average of different experiments during which the fish were aging.

In addition, the *col11a2* mutant zebrafish appear more cohesive than the wt fish, characterised by the high peaks in the RDF of the *col11a2* mutant zebrafish. This feature can not be captured by conventional methods such as the nearest neighbour distance. In fact, the *col11a2* mutant zebrafish have a larger  $l_{nn}$  values compared with the wildtype counterpart. However, the *col11a2* mutant zebrafish are more cohesive because they are more likely to have a pairwise distance around 10 cm. It is this probability that captured the cohesive feature, rather than the physical length scale. Even though these two are normally correlated.

### 7.4.3 Modelling the dynamics of *col11a2* mutant zebrafish

We projected the changing states of the fish onto a “phase diagram”, spanned by the persistence length ( $l_p$ , Eq. 5.13) and the nearest neighbour distance ( $l_{nn}$ , Eq. 5.4). The result was shown in Fig. 7.7 (a). Compared to the wt fish, the *col11a2* mutant zebrafish have both larger  $l_{nn}$  and  $l_p$ . The larger  $l_{nn}$  values of the *col11a2* mutant zebrafish might be related from the fact that these mutant fish distribute in the upper location of the tank, where they naturally get larger volume because of the geometry of the tank. Even though the  $l_{nn}$  value of the *col11a2* mutant zebrafish is larger than the wt

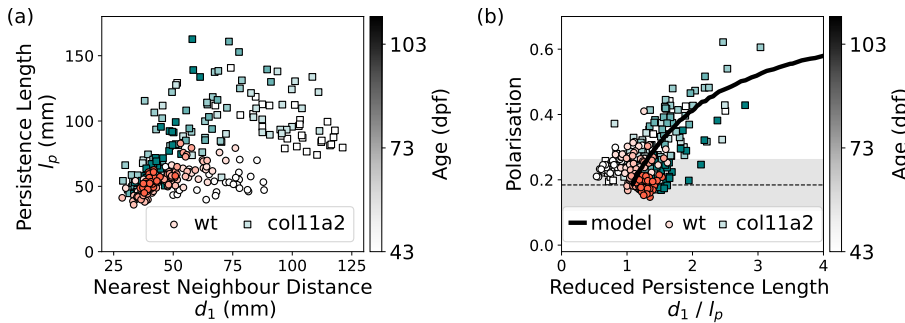


**Figure 7.7:** The behaviour of 25 zebrafish described by  $l_{nn}$  and  $l_p$ . (a) The changing macroscopic states of the fish projected on a 2D state diagram spanned by  $l_{nn}$  and  $l_p$ . The colour of the scatters represents the age of the fish. (b) The changing states of the fish described by the reduced persistence length  $\kappa = l_{nn}/l_p$ , which correlates with the polarisation ( $\Phi$ ) of the group. The correlation is reproduced with a Vicsek model with inertia (section 6.4.2). The brightness of the scatters indicates the age of the fish, illustrated by the colour bars.

fish, these mutant fish appear to be more cohesive, as discussed in section 7.4.2. The larger  $l_p$  of the *col11a2* mutant zebrafish is related to the slow re-orientation of the mutant fish, as the persistence length is defined as the product of the speed and the orientational relaxation time.

We observed the behaviour of 25 fish repeatedly, while the fish were growing. As a result, we could also follow the change of the behaviour of these fish over time. The age of the fish was coloured in Fig. 7.7. With the growth of the fish, the value of  $l_{nn}$  decreased for both the wt group and the mutant group. This indicates that the fish group became more closely packed as they grew from 40 dpf to over 100 dpf. The decreasing  $l_{nn}$  amongst the zebrafish was also observed by Buske and Gerlai [228].

For the observed zebrafish, being whether wt or mutant, their reduced persistence length, defined as  $\kappa = l_p/l_{nn}$ , correlates with the polarisation, as shown in Fig. 7.7 (b). Such correlation is similar to the results shown in section 5.7, from 50 adult zebrafish. Among the two groups, the *col11a2* mutant zebrafish have relatively larger  $\kappa$  values comparing with the wt fish, hence presenting higher  $\Phi$  values.

The relationship between the  $\Phi$  and  $\kappa$  can be explained by the variation of the Vicsek model with an inertia term ( $\alpha$ , Eq. 6.9). To fit the experimental data, we changed the value of  $\eta$  from 0.5 to 1.0, while fixing the values of other variables ( $v_0 = 0.1, \rho = 0.5, \alpha = 0.63$ ). These fixed parameters also fits the behaviour of 50 adult zebrafish, except for the value of the density (we set  $\rho = 1$  for 50 adult fish). The consistent fit suggests our proposed model, regardless of its simplicity, does capture the essence of the collective behaviour of zebrafish.

Biologically, the reason for the behavioural difference might relate to the compromised development of the cartilage, the bones, or the fine mineral stone in the ear of the fish. A careful examination of these intrinsic factors affecting the mutant fish would be the next step, for a more comprehensive understanding of the behaviour, as well as the genetic functions of the *col11a2* mutant fish.

## Summary of Chapter 7

- We applied the methods developed in previous chapters (3 - 6), and studied the behaviour of the *col11a2* mutant zebrafish.
- A single mutant fish exhibited a slow reorientation during its movement, compared to the wildtype zebrafish.
- A group ( $N = 25$ ) of *col11a2* mutant zebrafish exhibited larger persistence length, and higher polarisation value, compared to the wildtype zebrafish.
- A single mutant fish behave like an agent in the inertial Vicsek model with lower noise values, compared to the wildtype fish. Collectively, a group of *col11a2* mutant zebrafish exhibit more ordered movement because of the effective alignment interaction among the fish.

# Chapter 8

## Conclusions

A group of animals is an active matter system, whose collective behaviour could be interpreted in the framework of statistical physics. In this thesis, we studied the behaviour of zebrafish with the existing concepts and tools from the active matter community. For this purpose, we developed the experimental system, the tracking software, and the analytical methods to observe the 3D movement of fish in a quantitatively way. Using these tools, we studied the effect of genetic mutation on the zebrafish, focusing on a particular gene *col11a2* that is associated with human diseases.

In chapter 3, we developed the image processing pipeline to record the 2D collective motion for a group of fish. The proposed pipeline is capable of locating the fish in an image without the biological details. The ideas and algorithms to recover 3D coordinates from 2D images are introduced in chapter 4. It is expected that motivated readers can follow the path and build their own 3D animal tracking systems. As a result, we could obtain the locations of individual fish from our system at different time points, yielding the structural information of the fish group.

The coordinates of the fish need further process, so that we can study their collective behaviour. In chapter 5, we introduced the method to refine the coordinates, and the way to recover dynamical information from the coordinates, by linking the locations into trajectories. We then introduced the different quantities that captured the behavioural features of the zebrafish, and the different correlation functions for the dynamics and the structure of the fish group. The ideas and algorithms introduced in chapter 5 are expected to be helpful for other researchers. For instance, the coordinate refinement method and linking algorithms can be applied to the study of cellular behaviour or the movement of colloids. The correlation functions are helpful for characterising the structure and dynamics of different complex systems.

Using our developed method, we analysed the structure and dynamics of 50 zebrafish. We learned that the fish exhibited two well separated time scales, with the fast reorientation of individuals, and a slow relaxation of the local density. In addition, a group of fish change their macroscopic states constantly, whose collective motion could switch between ordered and disordered. These changing states, nevertheless, can be described by a single quantity that encodes the activity and density of the system.

To get further insight, we modelled the behaviour of the fish in chap-

ter 6. To understand the density distribution of the fish, we numerically simulated an equilibrium model to match the experimental results. The model revealed the effects of the environment, the pairwise interaction, and the group size. To understand the dynamics of the fish, we numerically studied an active matter model where particles align with nearby neighbours. The fit between simulation results and experimental data suggests the importance of the inertia and alignment interaction.

Finally, we observed the collective motion of 25 wildtype zebrafish and 25 *col11a2* mutant zebrafish, whose expression of type XI collagen was interrupted. Analysing the movement of individuals, we discovered the mutant fish have a significantly longer orientational relaxation time, presumably due to their compromised collagen development. The increased relaxation time leads to a higher activity for the *col11a2* mutant zebrafish, yielding more ordered collective behaviour. Such linkage could be explained by the dynamical model developed in chapter 6.

Many technical improvements could be made, for studies that are taking a similar route. For instance, the 2D image processing is still slow, which is incapable of real-time tracking. The speed could be improved with the machine learning methods, and maybe other optimised algorithms. For the 3D tracking, the urgent issue is to make the method more accessible, requiring the implementation of good software engineering principles, such as writing detailed documentation and helpful examples. Ideally, a graphical user interface should be provided for non-specialists without background in coding and computer vision.

For the study of zebrafish behaviour, a potential unexplored topic is the large scale milling phase in 3D<sup>57</sup>, presented in chapter 2. We did not observe such novel phenomenon in this project. To study this new pattern, and other potentially interesting collective behaviour, it may be necessary carry out field observations in the sea. In addition, it would be helpful to perform more experiments under controlled conditions, to study the response of the fish group to external stimuli.

For the understanding of zebrafish behaviour, we tried to model the density distribution and the dynamics of the fish separately. We did not craft a model that is capable of capturing both the structural features and the dynamical features at the same time. It is worthwhile to seek a simple model that recreates more experimental behavioural features.

Is active matter a useful concept, for the sake of biology? The statistical tools helped us extracting important time-scales and length-scales of the zebrafish. We understood their collective order-disorder transition with an active matter model, and studied the effect of genetic mutation under the same framework. At the end of the thesis, we provide positive answer to this question.

<sup>57</sup> The 2D milling phase was carefully studied by Tunstrøm et al. [126].

# Appendices

## Appendix A

# Alternative 2D Image Analysis Methods

### A.1 Introduction

It is possible to get information about the collective behaviour of zebrafish in a quasi-2D environment, without locating each fish individual or linking coordinates into trajectories. We will briefly describe a “tracking-free” analysis and relevant results in this chapter. The experimental setup used to observe the fish is identical to the one discussed in chapter 3.

This tracking-free method is helpful when the fish are very densely packed, since the tracking would fail because of the constant visual occlusion. The densely packed situation happens, as a group of fish exhibit the coexistence between dense regions and dilute regions in certain conditions. Such a “phase-separation” scenario is shown in Fig. A.1, where the dense regions are outlined. This coexistence is reminiscent of the *mobility induced phase separation (MIPS)* phenomenon, commonly seen in a repulsion-dominated active matter system (chapter 2) [45].

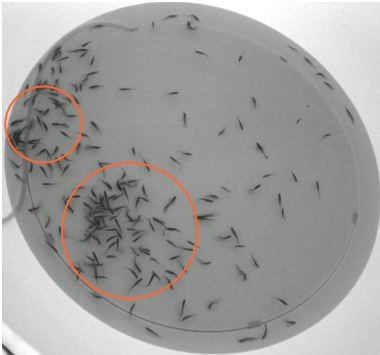


Figure A.1: The dense and dilute regions in a group of fish. The group size is 200, and the fish were confined in a quasi-2D environment.

<sup>58</sup> The areas of the grids seems different because of the projective transformation during the formation of the image. The areas are the same in the rectified image.

### A.2 Estimating Density Heterogeneity

We can quantify the coexistence of the high-density “liquid” and low-density “gas” with the heterogeneity of the density distribution. To do so, we subdivide the image into different grids with the same area, and measure the brightness variation among the grids. One example of these grids<sup>58</sup> is shown in Fig. A.2. For a uniformly distributed fish group, the variation would be close to zero. For phase-separated fish group, the variation would have a large value. Operationally, We take the sum of bright pixels in the foreground movie  $F_{ij}(t)$  in each grid, as a measure of the *density*, noted as  $\tilde{\rho}$ . We take the standard deviation of  $\tilde{\rho}$  values from all grids, as a measure of the density heterogeneity, noted as  $\mathcal{D} = \text{std}(\tilde{\rho})$ .

Figure A.2 shows the measured  $\mathcal{D}$  for 100 zebrafish. The grids were shown in Fig. A.2 (c), and clearly different grids have different  $\tilde{\rho}$  values. The temporal evolution of  $\mathcal{D}$  is shown in Fig. A.2 (a). We carefully kept the illumination condition in the observation room constant, to avoid sudden changes in  $\mathcal{D}$ . Figure A.2 shows the probability density function of  $\mathcal{D}$ , exhibiting a single peak around 1.1.

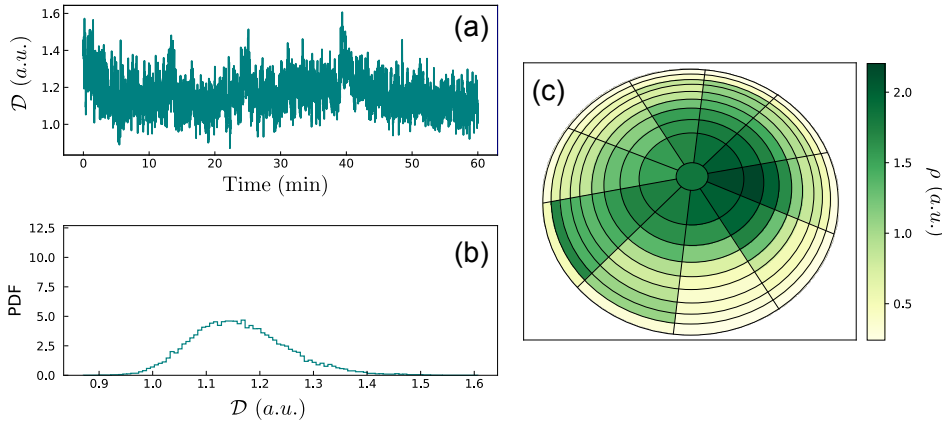


**Figure A.2:** Density Heterogeneity analysis of 100 zebrafish swimming in a quasi-2D environment. The units for  $\tilde{\rho}$  and  $\mathcal{D}$  are arbitrary, which are related to the pixel intensity in the image. (a) The density heterogeneity  $\mathcal{D}$  of the fish group as a function of time. (b) The probability density function of the density heterogeneity  $\mathcal{D}$ . (c) A snapshot of the density distribution of the fish. The tank was partitioned into different grids with the same area. The colour indicates the pixel brightness in each grid. Darker colour = more fish.

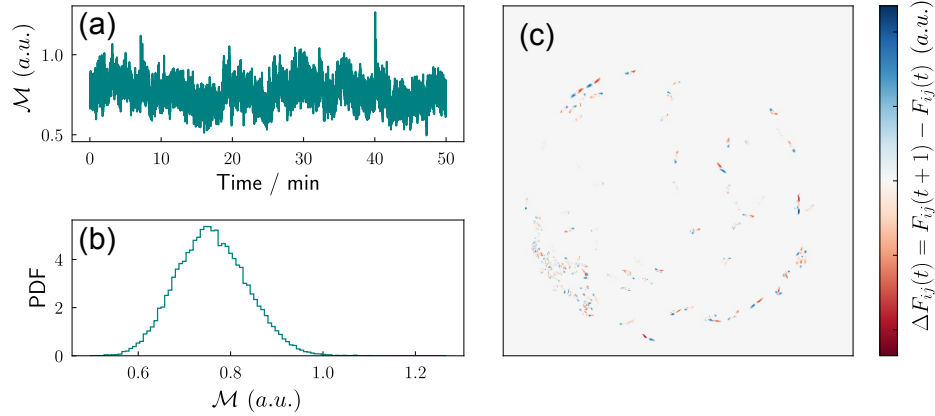


**Figure A.3:** The mobility analysis of 100 zebrafish swimming in a quasi-2D environment. The unit for  $M$  is arbitrary, which is related to the pixel intensity in the image. (a) The mobility  $M$  of the fish group as a function of time. (b) The probability density function of the mobility  $M$ . (c) The difference between two success frames. The dark pixels contains the moving fish.

### A.3 Estimating the Mobility

If we think of a group of zebrafish as active matter, we would want to measure its *activity*, which controls the phase behaviour of the system. The direct measurement of the activity requires the trajectory of individual fish from tracking result. A simpler measurement is the *mobility* of the fish group, which is defined as

$$\mathcal{M} = \sum_{ij} |F_{ij}(t+1) - F_{ij}(t)|, \quad (\text{A.1})$$

where  $F_{ij}(t)$  represents the pixel value of the foreground video at time  $t$  (see section 3.2.3 for details).

Figure A.3 shows the measured  $\mathcal{M}$  for 100 zebrafish. The difference between two success frames in the foreground video,  $\Delta F_{ij}(t)$ , is shown in Fig. A.3 (c), whose absolute sum is the mobility. The values of  $\mathcal{M}$  as a function of time is plotted in Fig. A.3 (a). The probability density function of  $\mathcal{M}$  is shown in Fig. A.3 (b), featuring a single peak.

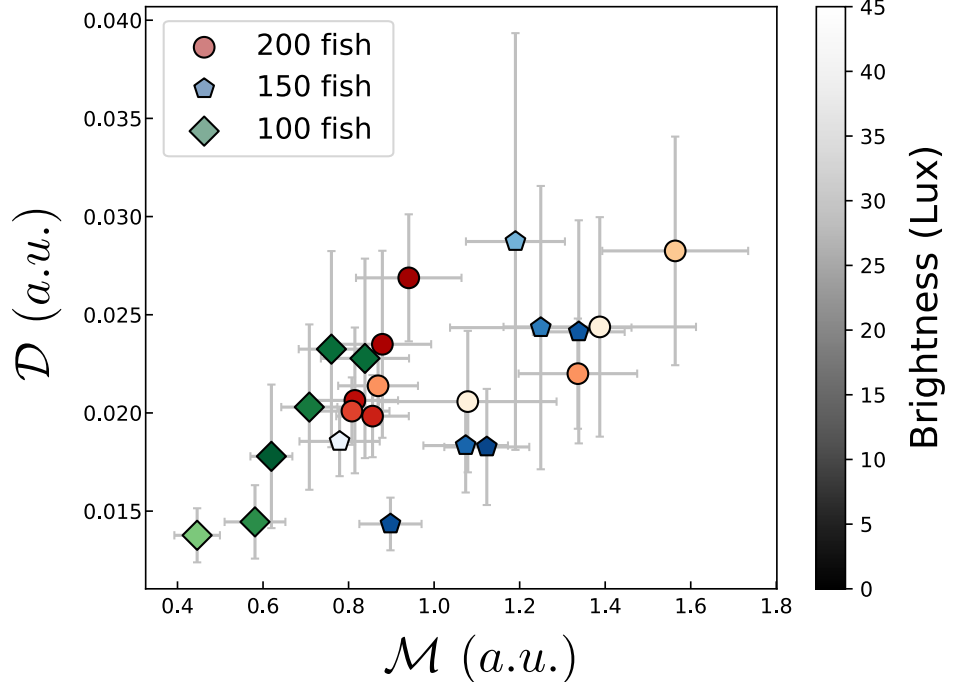


**Figure A.4:** The changing macroscopic states of zebrafish under different illumination conditions. The macroscopic state is indicated by the density heterogeneity ( $\mathcal{D}$ ) and the mobility ( $\mathcal{M}$ ) of the fish group. The error bars represent the standard error of the measurement.

## A.4 Changing States of the Fish Group

We changed the macroscopic state of the fish, by applying different illumination conditions with a smart bulb. It was expected that the fish would perceive more danger in a brighter environment, which leads to a higher  $\mathcal{D}$  value for the group. However, we found that the fish group have non-monotonic response to the brightness of the environment.

The changing macroscopic states of different fish groups, with different group sizes, is shown in Fig. A.4. It is not clear how increasing the brightness level would change the  $\mathcal{D}$  and  $\mathcal{M}$  values of the fish group. The absence of a monotonic relationship could be the result of the other biological or environmental factors, which requires more studies in the future.

However, it is clear that the fish groups exhibited very different macroscopic states, under different illumination conditions. These changing states is consistent with our analysis in chapter 5.

## A.5 MIPS as a Possible Explanation

The different density heterogeneity  $\mathcal{D}$  and mobility  $\mathcal{M}$  values of the fish group could be understood as a MIPS-like behaviour (chapter 2). The result is organised in Fig. A.5, where we use the value of  $\mathcal{D}/N$  as the order parameter. A large  $\mathcal{D}/N$  value indicates the coexistence of a dense phase and a dilute phase, therefore the MIPS.

For the observed fish groups, the MIPS-like behaviour happened if the mobility per fish ( $\mathcal{M}/N$ , as a proxy to the *activity*) is large, and the fish number (as a proxy to the *density*) is moderate. This is in-accordance of the phase behaviour of repulsion dominated active matter systems (for instance the active Brownian particles) [34].

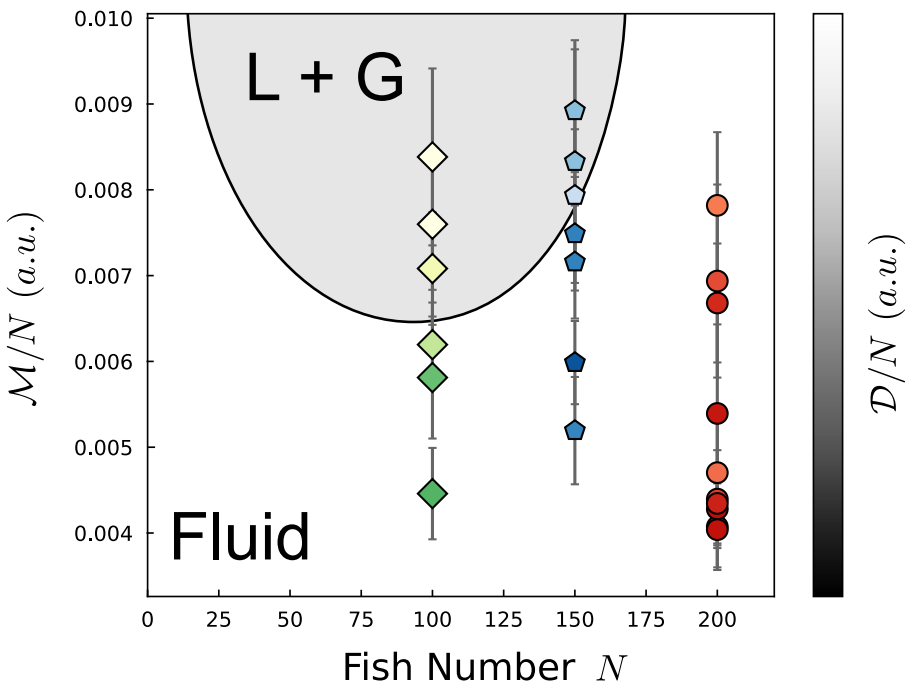


**Figure A.5:** The changing macroscopic states of zebrafish exhibiting a MIPS like phase behaviour. The fish number ( $N$ ) is related to the density, and the mobility divided by the fish number ( $M/N$ ) is a proxy to the activity. In a high activity and moderate density region, we observe a high density heterogeneity per fish ( $D/N$ ) value, corresponding to the coexistence of a dense phase (liquid) and a dilute phase (gas). The coexistence region is drawn manually for illustration.

However, the emergence of MIPS-like behaviour for a group of fish is a surprising result, which needs more careful studies. For instance, more state points should be sampled in the phase diagram. In addition, more detailed analysis is needed. For instance, one should check if the dense regions are also slow, as a result of the feedback loop in MIPS. Finally, the “tracking-free” analysis in this chapter is novel, which needs validation. For instance, we should compare the results of this tracking-free analysis, with the results from widely accepted analysis based on tracking individuals.

## Summary of Appendix A

- We proposed a new method to analyse the video for a group of fish in a quasi-2D environment, without tracking the movement of the individuals.
- The density heterogeneity of the fish group can be estimated by subdividing the image into grids, and calculating the intensity variation in different grids.
- The mobility of the fish group can be estimated by the difference between two successive frames.
- The changing illumination condition changed the macroscopic states of the fish group. But the fish respond to the changing brightness level in a non-monotonic way.
- The different macroscopic states of the fish group is similar to the MIPS behaviour of repulsion-dominated active particles.

# Bibliography

- [1] Y. Yang, F. Turci, E. Kague, C. L. Hammond, J. Russo, and C. P. Royall, “Dominating lengthscales of zebrafish collective behaviour”, *PLOS Computational Biology* **18**, 1 (2022).
- [2] E. Kague, F. Turci, E. Newman, Y. Yang, K. R. Brown, M. S. Aglan, G. A. Otaify, S. A. Temtamy, V. L. Ruiz-Perez, S. Cross, C. P. Royall, P. E. Witten, and C. L. Hammond, “3D assessment of intervertebral disc degeneration in zebrafish identifies changes in bone density that prime disc disease”, *Bone Research*, 1 (2021).
- [3] P. López-Cuevas, L. Deane, Y. Yang, C. L. Hammond, and E. Kague, “Transformed notochordal cells trigger chronic wounds in zebrafish, destabilizing the vertebral column and bone homeostasis”, *Disease Models & Mechanisms* **14**, dmm047001 (2021).
- [4] R. Salazar-Silva, V. L. G. Dantas, L. U. Alves, A. C. Batissoco, J. Oiticica, E. A. Lawrence, A. Kawafi, Y. Yang, F. S. Nicastro, B. C. Novaes, C. Hammond, E. Kague, and R. C. Mingroni-Netto, “NCOA3 identified as a new candidate to explain autosomal dominant progressive hearing loss”, *Human Molecular Genetics* **29**, 3691 (2021).
- [5] P. W. Anderson, “More Is Different: Broken symmetry and the nature of the hierarchical structure of science.”, *Science* **177**, 393 (1972).
- [6] A. Zacccone, “Explicit Analytical Solution for Random Close Packing in  $d = 2$  and  $d = 3$ ”, *Physical Review Letters* **128**, 028002 (2022).
- [7] R. Blumenfeld, “Comment on ”Explicit Analytical Solution for Random Close Packing in  $d=2$  and  $d=3$ ”, *Physical Review Letters* {\bf 128}, 028002 (2022)”, arXiv:2201.10550 [cond-mat, physics:math-ph] (2022).
- [8] P. Charbonneau and P. K. Morse, “Comment on ”Explicit Analytical Solution for Random Close Packing in  $d = 2$  and  $d = 3$ ”, arXiv:2201.07629 [cond-mat] (2022).
- [9] D. Chen and R. Ni, “Comment on ”Explicit Analytical Solution for Random Close Packing in  $d=2$  and  $d=3$ ”, arXiv:2201.06129 [cond-mat] (2022).
- [10] R. D. Kamien and A. J. Liu, “Why is Random Close Packing Reproducible?”, *Physical Review Letters* **99**, 155501 (2007).
- [11] A. Malins, S. R. Williams, J. Eggers, and C. P. Royall, “Identification of structure in condensed matter with the topological cluster classification”, *The Journal of Chemical Physics* **139**, 234506 (2013).

- [12] J. F. Robinson, F. Turci, R. Roth, and C. P. Royall, “Morphometric approach to many-body correlations in hard spheres”, *Physical Review Letters* **122**, 068004 (2019).
- [13] T. Walker, D. Sesko, and C. Wieman, “Collective behavior of optically trapped neutral atoms”, *Physical Review Letters* **64**, 408 (1990).
- [14] H. N. W. Lekkerkerker, W. C. -. Poon, P. N. Pusey, A. Stroobants, and P. B. Warren, “Phase behaviour of colloid + polymer mixtures”, *Europhysics Letters (EPL)* **20**, 559 (1992).
- [15] C. Becco, N. Vandewalle, J. Delcourt, and P. Poncin, “Experimental evidences of a structural and dynamical transition in fish school”, *Physica A: Statistical Mechanics and its Applications* **367**, 487 (2006).
- [16] L. F. Henderson, “The statistics of crowd fluids”, *Nature* **229**, 381 (1971).
- [17] J. L. Silverberg, M. Bierbaum, J. P. Sethna, and I. Cohen, “Collective motion of humans in mosh and circle pits at heavy metal concerts”, *Physical Review Letters* **110**, 617 (2013).
- [18] J. Sethna, *Statistical mechanics: Entropy, order parameters and complexity*, Oxford Master Series in Physics (OUP Oxford, 2006).
- [19] E. P. Neff, “Where the wild zebrafish are”, *Lab Animal* **49**, 305 (2020).
- [20] P. S. Suriyampola, D. S. Shelton, R. Shukla, T. Roy, A. Bhat, and E. P. Martins, “Zebrafish Social Behavior in the Wild”, *Zebrafish* **13**, 1 (2016).
- [21] D. S. Shelton, S. G. Shelton, D. K. Daniel, M. Raja, A. Bhat, R. L. Tanguay, D. M. Higgs, and E. P. Martins, “Collective behavior in wild zebrafish”, *Zebrafish* **17**, 243 (2020).
- [22] K. Howe, M. D. Clark, C. F. Torroja, J. Torrance, C. Berthelot, M. Muffato, J. E. Collins, S. Humphray, K. McLaren, L. Matthews, S. McLaren, I. Sealy, M. Caccamo, C. Churcher, C. Scott, J. C. Barrett, R. Koch, G.-J. Rauch, S. White, W. Chow, B. Kilian, L. T. Quintais, J. A. Guerra-Assunção, Y. Zhou, Y. Gu, J. Yen, J.-H. Vogel, T. Eyre, S. Redmond, R. Banerjee, J. Chi, B. Fu, E. Langley, S. F. Maguire, G. K. Laird, D. Lloyd, E. Kenyon, S. Donaldson, H. Sehra, J. Almeida-King, J. Loveland, S. Trevanion, M. Jones, M. Quail, D. Willey, A. Hunt, J. Burton, S. Sims, K. McLay, B. Plumb, J. Davis, C. Clee, K. Oliver, R. Clark, C. Riddle, D. Elliott, G. Threadgold, G. Harden, D. Ware, S. Begum, B. Mortimore, G. Kerry, P. Heath, B. Phillimore, A. Tracey, N. Corby, M. Dunn, C. Johnson, J. Wood, S. Clark, S. Pelan, G. Griffiths, M. Smith, R. Glithero, P. Howden, N. Barker, C. Lloyd, C. Stevens, J. Harley, K. Holt, G. Panagiotidis, J. Lovell, H. Beasley, C. Henderson, D. Gordon, K. Auger, D. Wright, J. Collins, C. Raisen, L. Dyer, K. Leung, L. Robertson, K. Ambridge, D. Leongamornlert, S. McGuire, R. Gilderthorp, C. Griffiths, D. Manthravadi, S. Nichol, G. Barker, S. Whitehead, M. Kay, J. Brown, C. Murnane, E. Gray, M. Humphries, N. Sycamore, D. Barker, D. Saunders, J. Wallis, A. Babbage, S. Hammond, M.

- Mashreghi-Mohammadi, L. Barr, S. Martin, P. Wray, A. Ellington, N. Matthews, M. Ellwood, R. Woodmansey, G. Clark, J. D. Cooper, A. Tromans, D. Grafham, C. Skuce, R. Pandian, R. Andrews, E. Harrison, A. Kimberley, J. Garnett, N. Fosker, R. Hall, P. Garner, D. Kelly, C. Bird, S. Palmer, I. Gehring, A. Berger, C. M. Dooley, Z. Ersan-Ürün, C. Eser, H. Geiger, M. Geisler, L. Karotki, A. Kirn, J. Konantz, M. Konantz, M. Oberländer, S. Rudolph-Geiger, M. Teucke, C. Lanz, G. Raddatz, K. Osoegawa, B. Zhu, A. Rapp, S. Widaa, C. Langford, F. Yang, S. C. Schuster, N. P. Carter, J. Harrow, Z. Ning, J. Herrero, S. M. J. Searle, A. Enright, R. Geisler, R. H. A. Plasterk, C. Lee, M. Westerfield, P. J. de Jong, L. I. Zon, J. H. Postlethwait, C. Nüsslein-Volhard, T. J. P. Hubbard, H. R. Crolli, J. Rogers, and D. L. Stemple, “The zebrafish reference genome sequence and its relationship to the human genome”, *Nature* **496**, 498 (2013).
- [23] C. B. Kimmel, W. W. Ballard, S. R. Kimmel, B. Ullmann, and T. F. Schilling, “Stages of embryonic development of the zebrafish”, *Developmental Dynamics* **203**, 253 (1995).
  - [24] E. A. Lawrence, E. Kague, J. A. Aggleton, R. L. Harniman, K. A. Roddy, and C. L. Hammond, “The mechanical impact of col11a2 loss on joints; col11a2 mutant zebrafish show changes to joint development and function, which leads to early-onset osteoarthritis”, *Philosophical Transactions of the Royal Society B: Biological Sciences* **373**, 20170335 (2018).
  - [25] O.-H. Kim, H.-J. Cho, E. Han, T. I. Hong, K. Ariyasiri, J.-H. Choi, K.-S. Hwang, Y.-M. Jeong, S.-Y. Yang, K. Yu, D.-S. Park, H.-W. Oh, E. E. Davis, C. E. Schwartz, J.-S. Lee, H.-G. Kim, and C.-H. Kim, “Zebrafish knockout of Down syndrome gene, DYRK1A, shows social impairments relevant to autism”, *Molecular Autism* **8**, 50 (2017).
  - [26] R. Spence, G. Gerlach, C. Lawrence, and C. Smith, “The behaviour and ecology of the zebrafish, *Danio rerio*”, *Biological Reviews* **83**, 13 (2007).
  - [27] M. Westerfield, *The zebrafish book: A guide for the laboratory use of zebrafish (danio rerio)*, University of Oregon Press (University of Oregon Press, 2000).
  - [28] S. Ramaswamy, “Active matter”, *Journal of Statistical Mechanics: Theory and Experiment* **2017**, 054002 (2017).
  - [29] P. Romanczuk, M. Bär, W. Ebeling, B. Lindner, and L. Schimansky-Geier, “Active Brownian particles: From individual to collective stochastic dynamics”, *The European Physical Journal Special Topics* **202**, 1 (2012).
  - [30] J. O’Byrne, Y. Kafri, J. Tailleur, and F. van Wijland, “Time irreversibility in active matter, from micro to macro”, *Nature Reviews Physics* **4**, 167 (2022).
  - [31] C. Bechinger, R. D. Leonardo, H. Löwen, C. Reichhardt, G. Volpe, and G. Volpe, “Active particles in complex and crowded environments”, *Reviews of Modern Physics* **88**, 045006 (2016).

- [32] J. RUDNICK and G. GASPARI, “The shapes of random-walks”, *Science* **237**, 384 (1987).
- [33] A. Mauleon-Amieva, M. Mosayebi, J. E. Hallett, F. Turci, T. B. Liverpool, J. S. van Duijneveldt, and C. P. Royall, “Competing active and passive interactions drive amoebalike crystallites and ordered bands in active colloids”, *Physical Review E* **102**, 032609 (2020).
- [34] F. Turci and N. B. Wilding, “Phase Separation and Multibody Effects in Three-Dimensional Active Brownian Particles”, *Phys. Rev. Lett.* **126**, 038002 (2021).
- [35] T. Vicsek, A. Czirók, E. Ben-Jacob, I. Cohen, and O. Shochet, “Novel type of phase transition in a system of self-driven particles”, *Physical Review Letters* **75**, 1226 (1995).
- [36] G. Grégoire and H. Chaté, “Onset of collective and cohesive motion”, *Physical Review Letters* **92**, 025702 (2004).
- [37] J. A. Pimentel, M. Aldana, C. Huepe, and H. Larralde, “Intrinsic and extrinsic noise effects on phase transitions of network models with applications to swarming systems”, *Physical Review E* **77**, 061138 (2008).
- [38] J. Toner, Y. Tu, and S. Ramaswamy, “Hydrodynamics and phases of flocks”, *Annals of Physics* **318**, 170 (2005).
- [39] J. Stenhammar, D. Marenduzzo, R. J. Allen, and M. E. Cates, “Phase behaviour of active Brownian particles: the role of dimensionality”, *Soft Matter* **10**, 1489 (2014).
- [40] A. P. Solon, H. Chaté, and J. Tailleur, “From Phase to Microphase Separation in Flocking Models: The Essential Role of Nonequilibrium Fluctuations”, *Physical Review Letters* **114**, 068101 (2015).
- [41] H. Chaté, “Dry aligning dilute active matter”, *Annual Review of Condensed Matter Physics* **11**, 1 (2020).
- [42] W. Krauth, *Statistical mechanics: Algorithms and computations*, Oxford University Press, UK (Oxford University Press, UK, 2006).
- [43] J. U. Klamser, S. C. Kapfer, and W. Krauth, “Thermodynamic phases in two-dimensional active matter”, *Nature Communications*, 1 (2018).
- [44] Y. Fily and M. C. Marchetti, “Athermal phase separation of self-propelled particles with no alignment”, *Physical Review Letters* **108**, 235702 (2012).
- [45] M. E. Cates and J. Tailleur, “Motility-induced phase separation”, *Annual Review of Condensed Matter Physics* **6**, 1 (2015).
- [46] P. Digregorio, D. Levis, A. Suma, L. F. Cugliandolo, G. Gonnella, and I. Pagonabarraga, “Full Phase Diagram of Active Brownian Disks: From Melting to Motility-Induced Phase Separation”, *Physical Review Letters* **121**, 098003 (2018).
- [47] J.-P. Hansen and L. Verlet, “Phase transitions of the lennard-jones system”, *Physical Review* **184**, 151 (1969).

- [48] T. Speck, “Collective behavior of active Brownian particles: From microscopic clustering to macroscopic phase separation”, *The European Physical Journal Special Topics* **225**, 2287 (2016).
- [49] V. J. Anderson and H. N. W. Lekkerkerker, “Insights into phase transition kinetics from colloid science”, *Nature* **416**, 811 (2017).
- [50] A. Cavagna, P. M. Chaikin, D. Levine, S. Martiniani, A. Puglisi, and M. Viale, “Vicsek model by time-interlaced compression: A dynamical computable information density”, *Physical Review E* **103**, 062141 (2020).
- [51] R. Kürsten and T. Ihle, “Quantitative kinetic theory of flocking with three-particle closure”, *Physical Review E: Statistical Physics, Plasmas, Fluids, and Related Interdisciplinary Topics* **104**, 034604 (2021).
- [52] J. Toner and Y. Tu, “Long-range order in a two-dimensional dynamical XY model: How birds fly together”, *Physical Review Letters* **75**, 4326 (1995).
- [53] F. Ginelli and H. Chaté, “Relevance of Metric-Free Interactions in Flocking Phenomena”, *Physical Review Letters* **105**, 168103 (2010).
- [54] H. Chaté, F. Ginelli, G. Grégoire, and F. Raynaud, “Collective motion of self-propelled particles interacting without cohesion”, *Physical Review E* **77**, 046113 (2008).
- [55] A. Bricard, J.-B. Caussin, N. Desreumaux, O. Dauchot, and D. Bartolo, “Emergence of macroscopic directed motion in populations of motile colloids”, *Nature* **503**, 95 (2013).
- [56] D. Geyer, A. Morin, and D. Bartolo, “Sounds and hydrodynamics of polar active fluids”, *Nature Materials* **17**, 789 (2018).
- [57] N. Sakaï and C. P. Royall, “Active dipolar colloids in three dimensions: Strings, sheets, labyrinthine textures and crystals”, arXiv **2010**, arXiv:2010.03925 (2020).
- [58] F. A. Lavergne, H. Wendehenne, T. Bäuerle, and C. Bechinger, “Group formation and cohesion of active particles with visual perception-dependent motility”, *Science* **364**, 70 (2019).
- [59] V. Narayan, S. Ramaswamy, and N. Menon, “Long-Lived Giant Number Fluctuations in a Swarming Granular Nematic”, *Science* **317**, 105 (2007).
- [60] M. Bär, R. Großmann, S. Heidenreich, and F. Peruani, “Self-Propelled Rods: Insights and Perspectives for Active Matter”, *Annual Review of Condensed Matter Physics* **11**, 441 (2020).
- [61] F. J. Moore, C. P. Royall, T. B. Liverpool, and J. Russo, “Crystallisation and polymorph selection in active Brownian particles”, *The European Physical Journal E* **44**, 121 (2021).
- [62] A. K. Omar, K. Klymko, T. GrandPre, and P. L. Geissler, “Phase Diagram of Active Brownian Spheres: Crystallization and the Metastability of Motility-Induced Phase Separation”, *Physical Review Letters* **126**, 188002 (2021).

- [63] L. Berthier, E. Flenner, and G. Szamel, “How active forces influence nonequilibrium glass transitions”, *New Journal of Physics* **19**, 125006 (2017).
- [64] N. Klongvessa, F. Ginot, C. Ybert, C. Cottin-Bizonne, and M. Leocmach, “Active Glass: Ergodicity Breaking Dramatically Affects Response to Self-Propulsion”, *Physical Review Letters* **123**, 248004 (2019).
- [65] T. Speck, “Critical behavior of active Brownian particles: Connection to field theories”, arXiv (2022).
- [66] H. L. Devereux, C. R. Twomey, M. S. Turner, and S. Thutupalli, “Whirligig beetles as corralled active Brownian particles”, *Journal of The Royal Society Interface* **18**, rsif.2021.0114, 20210114 (2021).
- [67] A. Cavagna, A. Cimarelli, I. Giardina, G. Parisi, R. Santagati, F. Stefanini, and M. Viale, “Scale-free correlations in starling flocks”, *Proceedings of the National Academy of Sciences of the United States of America* **107**, 11865 (2010).
- [68] A. Attanasi, A. Cavagna, L. Del Castello, I. Giardina, S. Melillo, L. Parisi, O. Pohl, B. Rossaro, E. Shen, E. Silvestri, and M. Viale, “Collective Behaviour without Collective Order in Wild Swarms of Midges”, *PLoS Computational Biology* **10**, e1003697 (2014).
- [69] M. Allen and D. Tildesley, *Computer simulation of liquids* (OUP Oxford, 2017).
- [70] D. J. T. Sumpter, R. P. Mann, and A. Perna, “The modelling cycle for collective animal behaviour”, *Interface Focus* **2**, 764 (2012).
- [71] M. S. Bull and M. Prakash, “Mobile defects born from an energy cascade shape the locomotive behavior of a headless animal”, arXiv (2021).
- [72] M. Prakash, *Can we build "perceptive" machines from mechanical parts?*, July 2021.
- [73] M. S. Bull, L. A. Kroo, and M. Prakash, “Excitable mechanics embodied in a walking cilium”, arXiv (2021).
- [74] M. S. Bull, V. N. Prakash, and M. Prakash, “Ciliary flocking and emergent instabilities enable collective agility in a non-neuromuscular animal”, arXiv (2021).
- [75] T. Vicsek and A. Zafeiris, “Collective motion”, *Physics Reports* **517**, 71 (2012).
- [76] A. Strandburg-Peshkin, C. R. Twomey, N. W. Bode, A. B. Kao, Y. Katz, C. C. Ioannou, S. B. Rosenthal, C. J. Torney, H. S. Wu, S. A. Levin, and I. D. Couzin, “Visual sensory networks and effective information transfer in animal groups”, *Current Biology* **23**, R709 (2013).
- [77] K. Ota, I. Aihara, and T. Aoyagi, “Interaction mechanisms quantified from dynamical features of frog choruses”, *Royal Society Open Science* **7**, 191693 (2020).

- [78] C. H. Miller, M. F. Hillock, J. Yang, B. Carlson-Clarke, K. Haxhillari, A. Y. Lee, M. R. Warden, and M. J. Sheehan, *Dynamic changes to signal allocation rules in response to variable social environments in house mice*, Preprint (Ecology, Jan. 2022).
- [79] C. W. Reynolds, “Flocks, herds and schools: A distributed behavioral model”, *ACM SIGGRAPH Computer Graphics* **21**, 25 (1987).
- [80] I. D. Couzin, J. Krause, R. James, G. D. Ruxton, and N. R. Franks, “Collective memory and spatial sorting in animal groups”, *Journal of Theoretical Biology* **218**, 1 (2002).
- [81] J. Buhl, D. J. T. Sumpter, I. D. Couzin, J. J. Hale, E. Despland, E. R. Miller, and S. J. Simpson, “From disorder to order in marching locusts”, *Science* **312**, 1402 (2006).
- [82] C. A. Yates, R. Erban, C. Escudero, I. D. Couzin, J. Buhl, I. G. Kevrekidis, P. K. Maini, and D. J. T. Sumpter, “Inherent noise can facilitate coherence in collective swarm motion.”, *Proceedings of the National Academy of Sciences of the United States of America* **106**, 5464 (2009).
- [83] E. Fontaine, D. Lentink, S. Kranenbarg, U. K. Müller, J. L. van Leeuwen, A. H. Barr, and J. W. Burdick, “Automated visual tracking for studying the ontogeny of zebrafish swimming”, *Journal of Experimental Biology* **211**, 1305 (2008).
- [84] J. G. Puckett, A. R. Pokhrel, and J. A. Giannini, “Collective gradient sensing in fish schools”, *Scientific Reports*, 1 (2018).
- [85] H. E. A. MacGregor, J. E. Herbert-Read, and C. C. Ioannou, “Information can explain the dynamics of group order in animal collective behaviour”, *Nature Communications*, 1 (2020).
- [86] R. C. Gerum, B. Fabry, C. Metzner, M. Beaulieu, A. Ancel, and D. P. Zitterbart, “The origin of traveling waves in an emperor penguin huddle”, *New Journal of Physics* **15**, 125022 (2013).
- [87] R. Gerum, S. Richter, B. Fabry, C. Le Bohec, F. Bonadonna, A. Nesterova, and D. P. Zitterbart, “Structural organisation and dynamics in king penguin colonies”, *Journal of Physics D: Applied Physics* **51**, 164004 (2018).
- [88] D. P. Mersch, A. Crespi, and L. Keller, “Tracking Individuals Shows Spatial Fidelity Is a Key Regulator of Ant Social Organization”, *Science* **340**, 1090 (2013).
- [89] O. Feinerman, I. Pinkoviezky, A. Gelblum, E. Fonio, and N. S. Gov, “The physics of cooperative transport in groups of ants”, *Nature Physics*, 1 (2018).
- [90] J. F. Méndez-Valderrama, Y. A. Kinkhabwala, J. Silver, I. Cohen, and T. A. Arias, “Density-functional fluctuation theory of crowds”, *Nature Communications* **9**, 228701 (2018).
- [91] F. Ginelli, F. Peruani, M.-H. Pillot, H. Chaté, G. Theraulaz, and R. Bon, “Intermittent collective dynamics emerge from conflicting imperatives in sheep herds”, *Proceedings of the National Academy of Sciences* **112**, 12729 (2015).

- [92] A. Pérez-Escudero, J. Vicente-Page, R. C. Hinz, S. Arganda, and G. G. de Polavieja, “idTracker: tracking individuals in a group by automatic identification of unmarked animals”, *Nature Methods* **11**, 743 (2014).
- [93] A. Rodriguez, H. Zhang, J. Klaminder, T. Brodin, P. L. Andersson, and M. Andersson, “ToxTrac: A fast and robust software for tracking organisms”, *Methods in Ecology and Evolution* **9**, edited by R. Freckleton, 460 (2017).
- [94] F. Romero-Ferrero, M. G. Bergomi, R. C. Hinz, F. J. H. Heras, and G. G. de Polavieja, “Idtracker.ai: tracking all individuals in small or large collectives of unmarked animals”, *Nature Methods* **16**, 179 (2019).
- [95] T. Walter and I. D. Couzin, “TRex, a fast multi-animal tracking system with markerless identification, and 2D estimation of posture and visual fields”, *eLife* **10**, e64000 (2021).
- [96] V. Panadeiro, A. Rodriguez, J. Henry, D. Wlodkowic, and M. Andersson, “A review of 28 free animal-tracking software applications: current features and limitations”, *Lab Animal* **50**, 246 (2021).
- [97] N. C. Makris, P. Ratilal, D. T. Symonds, S. Jagannathan, S. Lee, and R. W. Nero, “Fish population and behavior revealed by instantaneous continental shelf-scale imaging”, *Science* **311**, 660 (2006).
- [98] N. C. Makris, P. Ratilal, S. Jagannathan, Z. Gong, M. Andrews, I. Bertsatos, O. R. Godø, R. W. Nero, and J. M. Jech, “Critical population density triggers rapid formation of vast oceanic fish shoals.”, *Science* **323**, 1734 (2009).
- [99] D. Papageorgiou and D. R. Farine, “Group size and composition influence collective movement in a highly social terrestrial bird”, *eLife* **9**, e59902 (2020).
- [100] J. Cullen, E. Shaw, and H. A. Baldwin, “Methods for measuring the three-dimensional structure of fish schools”, *Animal Behaviour* **13**, 534 (1965).
- [101] T. Pitcher, “The three-dimensional structure of schools in the minnow, *Phoxinus phoxinus* (L.)”, *Animal Behaviour* **21**, 673 (1973).
- [102] R. Hartley and A. Zisserman, *Multiple view geometry in computer vision*, Second (Cambridge University Press, USA, 2003).
- [103] A. Cavagna, I. Giardina, A. Orlandi, G. Parisi, A. Procaccini, M. Viale, and V. Zdravkovic, “The STARFLAG handbook on collective animal behaviour: 1. Empirical methods”, *Animal Behaviour* **76**, 217 (2008).
- [104] M. Pedersen, J. B. Haurum, S. H. Bengtson, and T. B. Moeslund, “3D-ZeF - a 3D zebrafish tracking benchmark dataset.”, *CVPR*, 10.1109/cvpr42600.2020.00250 (2020).
- [105] H. Ling, G. E. McIvor, G. Nagy, S. MohaimenianPour, R. T. Vaughan, A. Thornton, and N. T. Ouellette, “Simultaneous measurements of three-dimensional trajectories and wingbeat frequencies of birds in the field”, *Journal of The Royal Society Interface* **15**, 20180653 (2018).

- [106] A. Cavagna, S. Melillo, L. Parisi, and F. Ricci-Tersenghi, “SpaRTA Tracking Across Occlusions via Partitioning of 3D Clouds of Points”, *IEEE Transactions on Pattern Analysis and Machine Intelligence* **43**, 1394 (2021).
- [107] A. Attanasi, A. Cavagna, L. D. Castello, I. Giardina, A. Jeli, S. Melillo, L. Parisi, F. Pellacini, E. Shen, E. Silvestri, and M. Viale, “GReTA-A novel global and recursive tracking algorithm in three dimensions”, *IEEE Transactions on Pattern Analysis and Machine Intelligence* **37**, 2451 (2015).
- [108] N. T. Ouellette, H. Xu, and E. Bodenschatz, “A quantitative study of three-dimensional Lagrangian particle tracking algorithms”, *Experiments in Fluids* **40**, 301 (2005).
- [109] H. Xu, “Tracking Lagrangian trajectories in position–velocity space”, *Measurement Science and Technology* **19**, 075105 (2008).
- [110] M. Nagy, Z. Ákos, D. Biro, and T. Vicsek, “Hierarchical group dynamics in pigeon flocks”, *Nature Publishing Group* **464**, 890 (2010).
- [111] A. Attanasi, A. Cavagna, L. Del Castello, I. Giardina, T. S. Grigera, A. Jelic, S. Melillo, L. Parisi, O. Pohl, E. Shen, and M. Viale, “Information transfer and behavioural inertia in starling flocks”, *Nature Physics* **10**, 691 (2014).
- [112] H. Ling, G. E. McIvor, K. Vaart, R. T. Vaughan, A. Thornton, and N. T. Ouellette, “Costs and benefits of social relationships in the collective motion of bird flocks”, *Nature Ecology & Evolution*, **1** (2019).
- [113] S. Butail, N. Manoukis, M. Diallo, A. S. Yaro, A. Dao, S. F. Traoré, J. M. Ribeiro, T. Lehmann, and D. A. Paley, “3D tracking of mating events in wild swarms of the malaria mosquito *Anopheles gambiae*”, *2011 Annual International Conference of the IEEE Engineering in Medicine and Biology Society* **2011**, 720 (2011).
- [114] A. D. Straw, K. Branson, T. R. Neumann, and M. H. Dickinson, “Multi-camera real-time three-dimensional tracking of multiple flying animals”, *Journal of The Royal Society Interface* **8**, 395 (2011).
- [115] A. Attanasi, A. Cavagna, L. Del Castello, I. Giardina, S. Melillo, L. Parisi, O. Pohl, B. Rossaro, E. Shen, E. Silvestri, and M. Viale, “Finite-Size Scaling as a Way to Probe Near-Criticality in Natural Swarms”, *Physical Review Letters* **113**, 211 (2014).
- [116] D. H. Kelley and N. T. Ouellette, “Emergent dynamics of laboratory insect swarms”, *Scientific Reports* **3**, 4714 (2013).
- [117] K. van der Vaart, M. Sinhuber, A. M. Reynolds, and N. T. Ouellette, “Mechanical spectroscopy of insect swarms”, *Science Advances* **5**, eaaw9305 (2019).
- [118] J. R. Stowers, M. Hofbauer, R. Bastien, J. Griessner, P. Higgins, S. Farooqui, R. M. Fischer, K. Nowikovsky, W. Haubensak, I. D. Couzin, K. Tessmar-Raible, and A. D. Straw, “Virtual reality for freely moving animals”, *Nature Methods* **14**, 995 (2017).

- [119] L. V. Rosa, F. V. Costa, J. Canzian, J. V. Borba, V. A. Quadros, and D. B. Rosemberg, “Three- and bi-dimensional analyses of the shoaling behavior in zebrafish: Influence of modulators of anxiety-like responses”, *Progress in Neuropsychopharmacology & Biological Psychiatry*, **109957** (2020).
- [120] M. Ballerini, N. Cabibbo, R. Candelier, A. Cavagna, E. Cisbani, I. Giardina, V. Lecomte, A. Orlandi, G. Parisi, A. Procaccini, M. Viale, and V. Zdravkovic, “Interaction ruling animal collective behavior depends on topological rather than metric distance: Evidence from a field study”, *Proceedings of the National Academy of Sciences* **105**, 1232 (2008).
- [121] A. Cavagna, D. Conti, C. Creato, L. Del Castello, I. Giardina, T. S. Grigera, S. Melillo, L. Parisi, and M. Viale, “Dynamic scaling in natural swarms”, *Nature Physics* **13**, 914 (2017).
- [122] A. Cavagna, X. Feng, S. Melillo, L. Parisi, L. Postiglione, and P. Villegas, “CoMo: A Novel Comoving 3D Camera System”, *IEEE Transactions on Instrumentation and Measurement* **70**, 1 (2021).
- [123] F. A. Francisco, P. Nührenberg, and A. Jordan, “High-resolution, non-invasive animal tracking and reconstruction of local environment in aquatic ecosystems”, *Movement Ecology* **8**, 27 (2020).
- [124] A. Engel, Y. Reuben, I. Kolesnikov, D. Churilov, R. Nathan, and A. Genin, “In situ three-dimensional video tracking of tagged individuals within site-attached social groups of coral-reef fish”, *Limnology and Oceanography: Methods* **19**, 579 (2021).
- [125] D. S. Calovi, U. Lopez, S. Ngo, C. Sire, H. Chaté, and G. Theraulaz, “Swarming, schooling, milling: phase diagram of a data-driven fish school model”, *New Journal of Physics* **16**, 015026 (2014).
- [126] K. Tunstrøm, Y. Katz, C. C. Ioannou, C. Huepe, M. J. Lutz, and I. D. Couzin, “Collective states, multistability and transitional behavior in schooling fish”, *PLoS Computational Biology* **9**, edited by E. Ben-Jacob, e1002915 (2013).
- [127] T. S. Grigera, “Everything you wish to know about correlations but are afraid to ask”, arXiv:2002.01750 [cond-mat] (2020).
- [128] J.-P. Hansen and I. R. McDonald, “Chapter 3 - static properties of liquids: Thermodynamics and structure”, in *Theory of simple liquids (fourth edition)*, edited by J.-P. Hansen and I. R. McDonald, Fourth Edition (Academic Press, Oxford, 2013), pp. 61–104.
- [129] R. Pathria and P. Beale, *Statistical mechanics*, Academic Press (Butterworth-Heinemann, 2011).
- [130] A. R. Dulaney, S. A. Mallory, and J. F. Brady, “The “isothermal” compressibility of active matter”, *The Journal of Chemical Physics* **154**, 014902 (2021).
- [131] A. Cavagna, A. Cimarelli, I. Giardina, A. Orlandi, G. Parisi, A. Procaccini, R. Santagati, and F. Stefanini, “New statistical tools for analyzing the structure of animal groups”, *Mathematical Biosciences* **214**, 32 (2008).

- [132] M. Romenskyy, J. E. Herbert-Read, A. J. W. Ward, and D. J. T. Sumpter, “Body size affects the strength of social interactions and spatial organization of a schooling fish (*Pseudomugil signifer*)”, *Royal Society Open Science* **4**, 161056 (2017).
- [133] R. Kürsten, S. Stroteich, M. Z. Hernández, and T. Ihle, “Multiple particle correlation analysis of many-particle systems: Formalism and application to active matter”, *Physical Review Letters* **124**, 088002 (2020).
- [134] K. Zahn, G. Maret, C. Russ, and H. H. von Grünberg, “Three-particle correlations in simple liquids.”, *Physical Review Letters* **91**, 115502 (2003).
- [135] S. R. Williams, “Topological classification of clusters in condensed phases”, arXiv, 1 (2007).
- [136] J. E. Hallett, F. Turci, and C. P. Royall, “The devil is in the details: pentagonal bipyramids and dynamic arrest”, *Journal of Statistical Mechanics: Theory and Experiment* **2020**, 014001 (2020).
- [137] 早川美德, “鳥の群れの動態解析と数理モデル”, *計測と制御* **52**, 207 (2013).
- [138] R. Ni and N. T. Ouellette, “Velocity correlations in laboratory insect swarms”, *The European Physical Journal Special Topics* **224**, 3271 (2015).
- [139] T. Castellani and A. Cavagna, “Spin-glass theory for pedestrians”, *Journal of Statistical Mechanics: Theory and Experiment* **2005**, P05012 (2005).
- [140] I. Herbut, *A modern approach to critical phenomena* (Cambridge University Press, 2007).
- [141] W. Bialek, A. Cavagna, I. Giardina, T. Mora, E. Silvestri, M. Viale, and A. M. Walczak, “Statistical mechanics for natural flocks of birds”, *Proceedings of the National Academy of Sciences* **109**, 4786 (2011).
- [142] K. van der Vaart, M. Sinhuber, A. M. Reynolds, and N. T. Ouellette, “Environmental perturbations induce correlations in midge swarms”, *Journal of The Royal Society Interface* **17**, 20200018 (2020).
- [143] B. (https://stats.stackexchange.com/users/173082/ben), *Autocorrelation definition*, Cross Validated, URL:https://stats.stackexchange.com/q/45512 (version: 2020-07-27).
- [144] B. L. Partridge, “Internal dynamics and the interrelations of fish in schools”, *Journal of comparative physiology* **144**, 313 (1981).
- [145] V. Mwaffo, R. P. Anderson, S. Butail, and M. Porfiri, “A jump persistent turning walker to model zebrafish locomotion”, *Journal of The Royal Society Interface* **12**, 20140884 (2015).
- [146] A. Zienkiewicz, D. A. Barton, M. Porfiri, and M. di Bernardo, “Data-driven stochastic modelling of zebrafish locomotion”, *Journal of Mathematical Biology* **71**, 1081 (2015).
- [147] G. A. Pavliotis, *Stochastic processes and applications: diffusion processes, the fokker-planck and langevin equations*, Vol. 60 (Springer, 2014).

- [148] A. Cavagna and I. Giardina, “Bird Flocks as Condensed Matter”, *Annual Review of Condensed Matter Physics* **5**, 183 (2014).
- [149] H. Ling, G. E. McIvor, J. Westley, K. Vaart, R. T. Vaughan, A. Thornton, and N. T. Ouellette, “Behavioural plasticity and the transition to order in jackdaw flocks”, *Nature Communications*, **1** (2019).
- [150] D. Bumann and J. Krause, “Front individuals lead in shoals of three-spined sticklebacks (*gasterosteus aculeatus*) and juvenile roach (*rutilus rutilus*)”, *Behaviour* **125**, 189 (1993).
- [151] Z. Chen, H.-T. Zhang, X. Chen, D. Chen, and T. Zhou, “Two-level leader-follower organization in pigeon flocks”, *EPL (Europhysics Letters)* **112**, 20008 (2015).
- [152] M. Yomosa, T. Mizuguchi, and Y. Hayakawa, “Spatio-Temporal Structure of Hooded Gull Flocks”, *PLoS ONE* **8**, edited by A. Dornhaus, e81754 (2013).
- [153] S. Martiniani, P. M. Chaikin, and D. Levine, “Quantifying hidden order out of equilibrium”, *Physical Review X* **9**, 011031 (2019).
- [154] S. Martiniani, Y. Lemberg, P. M. Chaikin, and D. Levine, “Correlation lengths in the language of computable information”, *arXiv cond-mat.stat-mech*, 10.1103/physrevlett.125.170601 (2020).
- [155] C. McAnlis and A. Haecky, *Understanding compression: Data compression for modern developers* (“O’Reilly Media, Inc.”, 2016).
- [156] M. Ballerini, N. Cabibbo, R. Candelier, A. Cavagna, E. Cisbani, I. Giardina, A. Orlandi, G. Parisi, A. Procaccini, M. Viale, and V. Zdravkovic, “Empirical investigation of starling flocks: a benchmark study in collective animal behaviour”, *Animal Behaviour* **76**, 201 (2008).
- [157] A. Cavagna, L. D. Castello, I. Giardina, T. Grigera, A. Jelic, S. Melillo, T. Mora, L. Parisi, E. Silvestri, M. Viale, and A. M. Walczak, “Flocking and turning: a new model for self-organized collective motion”, *Journal of Statistical Physics* **158**, 601 (2015).
- [158] Y.-L. Chou, R. Wolfe, and T. Ihle, “Kinetic theory for systems of self-propelled particles with metric-free interactions”, *Physical Review E* **86**, 021120 (2012).
- [159] A. Peshkov, S. Ngo, E. Bertin, H. Chaté, and F. Ginelli, “Continuous Theory of Active Matter Systems with Metric-Free Interactions”, *Physical Review Letters* **109**, 098101 (2012).
- [160] D. Martin, H. Chaté, C. Nardini, A. Solon, J. Tailleur, and F. Van Wijland, “Fluctuation-Induced Phase Separation in Metric and Topological Models of Collective Motion”, *Physical Review Letters* **126**, 148001 (2021).
- [161] P. Rahmani, F. Peruani, and P. Romanczuk, “Topological flocking models in spatially heterogeneous environments”, *Communications Physics* **4**, 206 (2021).

- [162] J. Gautrais, F. Ginelli, R. Fournier, S. Blanco, M. Soria, H. Chaté, and G. Theraulaz, “Deciphering interactions in moving animal groups”, *PLoS Computational Biology* **8**, edited by S. A. Levin, e1002678 (2012).
- [163] D. Strömbom, “Collective motion from local attraction”, *Journal of Theoretical Biology* **283**, 145 (2011).
- [164] J. Toner and Y. Tu, “Flocks, herds, and schools: A quantitative theory of flocking”, *Physical Review E* **58**, 4828 (1998).
- [165] M. R. Shaebani, A. Wysocki, R. G. Winkler, G. Gompper, and H. Rieger, “Computational models for active matter”, *arXiv cond-mat.soft*, [10.1038/s42254-020-0152-1](https://arxiv.org/abs/1010.1038/s42254-020-0152-1) (2019).
- [166] B. Mahault, F. Ginelli, and H. Chaté, “Quantitative assessment of the toner and tu theory of polar flocks”, *Physical Review Letters* **123**, 218001 (2019).
- [167] M. Nagy, I. Daruka, and T. Vicsek, “New aspects of the continuous phase transition in the scalar noise model (SNM) of collective motion”, *arXiv.org nlin.AO*, 445 (2006).
- [168] H. Chaté, F. Ginelli, G. Grégoire, F. Peruani, and F. Raynaud, “Modeling collective motion: variations on the Vicsek model”, *The European Physical Journal B* **64**, 451 (2008).
- [169] N. D. Mermin and H. Wagner, “Absence of Ferromagnetism or Antiferromagnetism in One- or Two-Dimensional Isotropic Heisenberg Models”, *Physical Review Letters* **17**, 1133 (1966).
- [170] F. Ginelli, “The physics of the vicsek model”, *The European Physical Journal Special Topics* **225**, 2099 (2016).
- [171] N. T. Ouellette, “A physics perspective on collective animal behavior”, *Physical Biology* **19**, 021004 (2022).
- [172] J.-P. Hansen and I. R. McDonald, “Statistical Mechanics”, in *Theory of Simple Liquids* (Elsevier, 2013), pp. 13–59.
- [173] D. Gorbonos, R. Ianconescu, J. G. Puckett, R. Ni, N. T. Ouellette, and N. S. Gov, “Long-range acoustic interactions in insect swarms: an adaptive gravity model”, *New Journal of Physics* **18**, 073042 (2016).
- [174] R. Ni, J. G. Puckett, E. R. Dufresne, and N. T. Ouellette, “Intrinsic Fluctuations and Driven Response of Insect Swarms”, *Physical Review Letters* **115**, 118104 (2015).
- [175] M. Sinhuber and N. T. Ouellette, “Phase Coexistence in Insect Swarms”, *Physical Review Letters* **119**, 178003 (2017).
- [176] S. C. Takatori, W. Yan, and J. F. Brady, “Swim Pressure: Stress Generation in Active Matter”, *Physical Review Letters* **113**, 028103 (2014).
- [177] D. A. Egolf, “Equilibrium Regained: From Nonequilibrium Chaos to Statistical Mechanics”, *Science* **287**, 101 (2000).
- [178] M. Sinhuber, K. van der Vaart, Y. Feng, A. M. Reynolds, and N. T. Ouellette, “An equation of state for insect swarms”, *Scientific Reports* **11**, 3773 (2021).

- [179] W. Tang, J. D. Davidson, G. Zhang, K. E. Conen, J. Fang, F. Serluca, J. Li, X. Xiong, M. Coble, T. Tsai, G. Molind, C. H. Fawcett, E. Sanchez, P. Zhu, I. D. Couzin, and M. C. Fishman, “Genetic control of collective behavior in zebrafish”, *iScience* **23**, 100942 (2020).
- [180] L. Chen, J. Toner, and C. F. Lee, “Critical phenomenon of the order-disorder transition in incompressible active fluids”, *New Journal of Physics* **17**, 042002 (2015).
- [181] V. Guttal, P. Romanczuk, S. J. Simpson, G. A. Sword, and I. D. Couzin, “Cannibalism can drive the evolution of behavioural phase polyphenism in locusts”, *Ecology Letters* **15**, edited by A. Liebhold, 1158 (2012).
- [182] N. Miller and R. Gerlai, “Quantification of shoaling behaviour in zebrafish (*Danio rerio*)”, *Behavioural Brain Research* **184**, 157 (2007).
- [183] F. J. H. Heras, F. Romero-Ferrero, R. C. Hinz, and G. G. de Polavieja, “Deep attention networks reveal the rules of collective motion in zebrafish”, *PLOS Computational Biology* **15**, e1007354 (2019).
- [184] V. H. Sridhar, L. Li, D. Gorbonos, M. Nagy, B. R. Schell, T. Sorochkin, N. S. Gov, and I. D. Couzin, “The geometry of decision-making in individuals and collectives”, *Proceedings of the National Academy of Sciences* **118**, e2102157118 (2021).
- [185] Y. Ma, S. Soatto, J. Kosecka, and S. S. Sastry, *An invitation to 3-D vision: From images to geometric models*, Springer New York (Springer New York, 2005).
- [186] J. M. Newby, A. M. Schaefer, P. T. Lee, M. G. Forest, and S. K. Lai, “Convolutional neural networks automate detection for tracking of submicron-scale particles in 2D and 3D”, *Proceedings of the National Academy of Sciences* **115**, 201804420 (2018).
- [187] I. Goodfellow, Y. Bengio, and A. Courville, *Deep learning*, <http://www.deeplearningbook.org> (MIT Press, 2016).
- [188] J. Solem, *Programming computer vision with python*, ”O'Reilly Media, Inc.” (“O'Reilly Media, Inc.”, June 2012).
- [189] A. Géron, *Hands-on machine learning with scikit-learn, keras, and TensorFlow: Concepts, tools, and techniques to build intelligent systems* (O'Reilly Media, 2019).
- [190] Martín Abadi, Ashish Agarwal, Paul Barham, Eugene Brevdo, Zhifeng Chen, Craig Citro, Greg S. Corrado, Andy Davis, Jeffrey Dean, Matthieu Devin, Sanjay Ghemawat, Ian Goodfellow, Andrew Harp, Geoffrey Irving, Michael Isard, Y. Jia, Rafal Jozefowicz, Lukasz Kaiser, Manjunath Kudlur, Josh Levenberg, Dandelion Mané, Rajat Monga, Sherry Moore, Derek Murray, Chris Olah, Mike Schuster, Jonathon Shlens, Benoit Steiner, Ilya Sutskever, Kunal Talwar, Paul Tucker, Vincent Vanhoucke, Vijay Vasudevan, Fernanda Viégas, Oriol Vinyals, Pete Warden, Martin Wattenberg, Martin Wicke, Yuan Yu, and Xiaqiang Zheng, *TensorFlow: large-scale machine learning on heterogeneous systems*, Software available from tensorflow.org, 2015.

- [191] T. Carneiro, R. V. Medeiros Da Nobrega, T. Nepomuceno, G.-B. Bian, V. H. C. De Albuquerque, and P. P. R. Filho, “Performance Analysis of Google Colaboratory as a Tool for Accelerating Deep Learning Applications”, *IEEE Access* **6**, 61677 (2018).
- [192] A. Séguret, B. Collignon, and J. Halloy, “Strain differences in the collective behaviour of zebrafish (*Danio rerio*) in heterogeneous environment”, *Royal Society Open Science* **3**, 160451 (2016).
- [193] C. F. Lee, “Active particles under confinement: aggregation at the wall and gradient formation inside a channel”, *New Journal of Physics* **15**, 055007 (2013).
- [194] C. Maggi, U. M. B. Marconi, N. Gnan, and R. Di Leonardo, “Multi-dimensional stationary probability distribution for interacting active particles”, *Scientific Reports* **5**, 10742 (2015).
- [195] D. B. Rosemberg, E. P. Rico, B. H. M. Mussulini, Á. L. Piatto, M. E. Calcagnotto, C. D. Bonan, R. D. Dias, R. E. Blaser, D. O. Souza, and D. L. de Oliveira, “Differences in spatio-temporal behavior of zebrafish in the open tank paradigm after a short-period confinement into dark and bright environments”, *PLoS ONE* **6**, edited by X. Zhuang, e19397 (2011).
- [196] A. Pérez-Escudero and G. G. de Polavieja, “Adversity magnifies the importance of social information in decision-making”, *Journal of The Royal Society Interface* **14**, 20170748 (2017).
- [197] H. G. Maas, A. Gruen, and D. Papantoniou, “Particle tracking velocimetry in three-dimensional flows”, *Experiments in Fluids* **15**, 14 (1993).
- [198] K.-Y. Chan, D. Stich, and G. A. Voth, “Real-time image compression for high-speed particle tracking”, *Review of Scientific Instruments* **78**, 023704 (2007).
- [199] J. W. Jolles, N. J. Boogert, V. H. Sridhar, I. D. Couzin, and A. Manica, “Consistent individual differences drive collective behavior and group functioning of schooling fish”, *Current Biology* **27**, 2862 (2017).
- [200] A. V. Kalueff, M. Gebhardt, A. M. Stewart, J. M. Cachat, M. Brimmer, J. S. Chawla, C. Craddock, E. J. Kyzar, A. Roth, S. Landsman, S. Gaikwad, K. Robinson, E. Baatrup, K. Tierney, A. Shamchuk, W. Norton, N. Miller, T. Nicolson, O. Braubach, C. P. Gilman, J. Pittman, D. B. Rosemberg, R. Gerlai, D. Echevarria, E. Lamb, S. C. F. Neuhauss, W. Weng, L. Bally-Cuif, H. Schneider, and Z. N. R. Consortium, “Towards a comprehensive catalog of zebrafish behavior 1.0 and beyond”, *Zebrafish* **10**, 70 (2013).
- [201] V. Mwaffo, S. Butail, and M. Porfiri, “In-silico experiments of zebrafish behaviour: modeling swimming in three dimensions”, *Scientific Reports* **7**, 39877 (2016).
- [202] Z. Zhang, “A flexible new technique for camera calibration”, *IEEE Transactions on Pattern Analysis and Machine Intelligence* **22**, 1330 (2000).

- [203] G. B. Dantzig, “Linear programming”, *Operations research* **50**, 42 (2002).
- [204] D. H. Theriault, N. W. Fuller, B. E. Jackson, E. Bluhm, D. Evangelista, Z. Wu, M. Betke, and T. L. Hedrick, “A protocol and calibration method for accurate multi-camera field videography”, *Journal of Experimental Biology* **217**, 1843 (2014).
- [205] J. Cachat, A. Stewart, E. Utterback, P. Hart, S. Gaikwad, K. Wong, E. Kyzar, N. Wu, and A. V. Kalueff, “Three-dimensional neurophenotyping of adult zebrafish behavior”, *PLoS ONE* **6**, edited by A. Bartolomucci, e17597 (2011).
- [206] J. Cachat, A. Stewart, L. Grossman, S. Gaikwad, F. Kadri, K. M. Chung, N. Wu, K. Wong, S. Roy, C. Suciu, J. Goodspeed, M. Ellegante, B. Bartels, S. Elkhayat, D. Tien, J. Tan, A. Denmark, T. Gilder, E. Kyzar, J. DiLeo, K. Frank, K. Chang, E. Utterback, P. Hart, and A. V. Kalueff, “Measuring behavioral and endocrine responses to novelty stress in adult zebrafish”, *Nature Protocols* **5**, 1786 (2019).
- [207] T. Biben, J.-P. Hansen, and J.-L. Barrat, “Density profiles of concentrated colloidal suspensions in sedimentation equilibrium”, *The Journal of Chemical Physics* **98**, 7330 (1993).
- [208] C. P. Royall, J. Dzubiella, M. Schmidt, and A. van Blaaderen, “Nonequilibrium Sedimentation of Colloids on the Particle Scale”, *Physical Review Letters* **98**, 77 (2007).
- [209] M. Newman and G. Barkema, *Monte carlo methods in statistical physics* (Clarendon Press, 1999).
- [210] L. Berthier, “Dynamic Heterogeneity in Amorphous Materials”, *Physics* **4**, 42 (2011).
- [211] P. Klein, *Coding the matrix: Linear algebra through applications to computer science* (Newtonian Press, 2013).
- [212] J. C. Crocker and D. G. Grier, “Methods of digital video microscopy for colloidal studies”, *Journal of Colloid and Interface Science* **179**, 298 (1996).
- [213] D. B. Allan, T. Caswell, N. C. Keim, C. M. van der Wel, and R. W. Verweij, *Soft-matter/trackpy: trackpy v0.5.0*, version v0.5.0, Apr. 2021.
- [214] d. Berg, M. Van Kreveld, M. Overmars, and O. Schwarzkopf, *Computational geometry: Algorithms and applications* (Springer, 2000).
- [215] N. Miller and R. Gerlai, “From schooling to shoaling: Patterns of collective motion in zebrafish (*danio rerio*)”, *PLoS ONE* **7**, edited by G. G. de Polavieja, e48865 (2012).
- [216] S. B. Rosenthal, C. R. Twomey, A. T. Hartnett, H. S. Wu, and I. D. Couzin, “Revealing the hidden networks of interaction in mobile animal groups allows prediction of complex behavioral contagion”, *Proceedings of the National Academy of Sciences* **112**, 4690 (2015).
- [217] I. Watts, M. Nagy, R. I. Holbrook, D. Biro, and T. Burt de Perera, “Validating two-dimensional leadership models on three-dimensionally structured fish schools”, *Royal Society Open Science* **4**, 160804 (2017).

- [218] M. Romenskyy, J. E. Herbert-Read, C. C. Ioannou, A. Szorkovszky, A. J. W. Ward, and D. J. T. Sumpter, “Quantifying the structure and dynamics of fish shoals under predation threat in three dimensions”, *Behavioral Ecology* **31**, edited by N. Dingemanse, 311 (2020).
- [219] J. Palacci, C. Cottin-Bizonne, C. Ybert, and L. Bocquet, “Sedimentation and Effective Temperature of Active Colloidal Suspensions”, *Physical Review Letters* **105**, 088304 (2010).
- [220] B. Yigit, Y. Alapan, and M. Sitti, “Cohesive self-organization of mobile microrobotic swarms”, *Soft Matter* **16**, 1996 (2020).
- [221] M. L. R. Puzzo, A. D. Virgiliis, and T. S. Grigera, “Self-propelled Vicsek particles at low speed and low density”, *Physical Review E* **99**, 052602 (2019).
- [222] N. Danos and G. V. Lauder, “Challenging zebrafish escape responses by increasing water viscosity”, *Journal of Experimental Biology* **215**, 1854 (2012).
- [223] T. Mora and W. Bialek, “Are Biological Systems Poised at Criticality?”, *Journal of Statistical Physics* **144**, 268 (2011).
- [224] M. Viikkula, E. C. Madman, V. C. Lui, N. I. Zhidkova, G. E. Tiller, M. B. Goldring, S. E. van Beersum, M. C. de Waal Malefijt, F. H. van den Hoogen, H.-H. Ropers, R. Mayne, K. S. Cheah, B. R. Olsen, M. L. Warman, and H. G. Brunner, “Autosomal dominant and recessive osteochondrodysplasias associated with the COL11A2 locus”, *Cell* **80**, 431 (1995).
- [225] E. Jakkula, M. Melkoniemi, I. Kiviranta, J. Lohiniva, S. Räinä, M. Perälä, M. Warman, K. Ahonen, H. Kröger, H. Göring, and L. Ala-Kokko, “The role of sequence variations within the genes encoding collagen II, IX and XI in non-syndromic, early-onset osteoarthritis”, *Osteoarthritis and Cartilage* **13**, 497 (2005).
- [226] Y.-J. Tseng, T.-H. Chen, S. C. Tsai, and S. M. Wu, “Effects of bisphenol A or diethyl phthalate on cartilage development and the swimming behavior of zebrafish (*Danio rerio*) through maternal exposure”, *Comparative Biochemistry and Physiology Part C: Toxicology & Pharmacology* **247**, 109057 (2021).
- [227] H. E. A. MacGregor and C. C. Ioannou, “Collective motion diminishes, but variation between groups emerges, through time in fish shoals”, *Royal Society Open Science* **8**, 210655 (2021).
- [228] C. Buske and R. Gerlai, “Shoaling develops with age in Zebrafish (*Danio rerio*)”, *Progress in Neuro-Psychopharmacology and Biological Psychiatry* **35**, 1409 (2011).